DISS.ETH No. 16933

Photonic crystals with metallic inclusions

A dissertation submitted to the

SWISS FEDERAL INSTITUTE OF TECHNOLOGY ZURICH

For the degree of

Doctor of Science

Presented by

Xudong Cui

M.S, Chinese Academy of Engineering Physics
B.S, Beijing Institute of Technology
Born 06, 03, 1973

Citizen of China

Accepted on the recommendation of

Prof. Dr. Ruediger Vahldieck, examiner
Prof. Dr. Christian Hafner, coexaminer
Prof. Dr. Hans-Peter Herzig, coexaminer

2006

Contents

Abstract

Photonic crystals are artificial materials that can be obtained from arranging at least two different materials with high index contrast on a regular lattice, i.e., two different dielectrics with a high index contrast or a dielectric and a metallic material. As electromagnetic waves are modulated periodically, there exist band gaps for such structures, in which propagating waves are not allowed to exist. Through introducing point or line defects in the photonic crystals, the light can be controlled, i.e., confined, guided, or localized. This opens a new door in photonics: technologies for directing light on a microscopic scale will have a major impact on telecommunication and related areas. In this thesis, photonic crystals were studied with numerical simulations and new components for optical communication were proposed.

For a better understanding of the fundamental effects of metallic photonic crystals, the scattering of electromagnetic waves at metallic wires both in the radio frequency and in the optical frequency range are outlined. This preparatory study includes plasmon resonances of a single wire and of a set of 9 wires. It is demonstrated that plasmon resonances cause flat band structures with many modes rather than photonic band gaps. At radio frequencies, the existence of a fundamental band gap for Ez waves is highly attractive for practical applications. It was demonstrated that a fundamental band gap also exists at optical frequencies (under certain conditions) although metals lose their conductivity almost entirely and must be described by a complex permittivity.

Filter characteristics of metallo-dielectric photonic crystal slabs are analyzed using the Multiple Multipole Program (MMP) combined with the Model-Based Parameter Estimation technique. This approach takes losses and material dispersion into account and provides highly accurate results at short computation time. Starting from this analysis, different ultra-compact band pass filters for telecommunication wavelengths are designed. The filters consist of only five silver wires embedded in a waveguide structure. By applying stochastic and deterministic techniques the filter structures are optimized to obtain the desired characteristics.

To realize Photonic Crystal slab based filters in integrated circuits, two methods: a) using conducting walls to replace periodic boundary conditions of the photonic crystal slab and b) embedding a photonic crystal filter in a conventional waveguide structure are presented. In the former case - as conductors at optical frequencies aren't Perfect Electric Conductors at all - a real metal (silver) was partially coated near the photonic crystal holes along the sides of the trench waveguide to realize a photonic crystal slab based filter. Although the coatings completely spoil the filter properties and the loss in the metal reduces the filter quality (transmission, bandwidth, etc.), it is possible to reestablish the desired filter characteristics by using an optimization procedure that also takes the coating into account.

In chapter 5, sharp trench waveguide bends in dual mode operation with small local photonic crystals for suppressing radiation are analyzed. Through optimization, different configurations with low reflection, low radiation, low mode conversion, and therefore high transmission for the dominant mode are obtained. Three different types of bends are analyzed and compared: mirror-based structures, resonator-based structures, and structures with small photonic crystals in the bend area. The local

photonic crystals help not only to suppress radiation but also to provide solutions with fewer fabrication tolerance problems.
In chapter 6, different definitions of the resolution of negative index material (NIM) slabs and classical optical lenses with magnification 1 are presented and evaluated for both cases. Several numerical codes – based on domain and boundary discretizations, working in the time- and frequency-domain – are applied and compared. It is shown that super resolution depends very much on the definition of the resolution and that it may be obtained not only for NIM slabs but also for highly refracting classical lenses when the distances of the image and source points from the surface of the lens or slab are shorter than the wavelength.

Zusammenfassung

Photonenkristalle sind künstliche Materialien, welche entstehen, wenn mindestens zwei unterschiedliche natürliche Materialien auf einem periodischen Gitter angeordnet werden. Dabei können entweder unterschiedliche Dielektrika (mit üblicherweise hohem Brechungsindexunterschied) oder Dielektrika mit Metallen kombiniert werden. Da damit die elektromagnetischen Wellen periodisch moduliert werden, entstehen Bandlücken in welchen keine ausbreitungsfähigen Wellen existieren. Durch gezielte Einführung von Punkt- oder Liniendefekten in Photonenkristallen kann die Lichtausbreitung kontrolliert, d.h. eingegrenzt oder geführt werden. Dadurch wird eine neue Tür der Lichttechnologie aufgestossen. Technologien, welche Licht in einem mikroskopischen Massstab manipulieren, werden einen grossen Einfluss auf die Telekommunikation und verwandte Gebiete haben. In der vorliegenden Dissertation werden Photonenkristalle mit numerischen Simulationen untersucht und neue Komponenten der optischen Kommunikation vorgeschlagen.

Für ein besseres Verständnis der grundlegenden Effekte in metallischen Photonenkristallen wird die Streuung elektromagnetischer Wellen an metallischen Drähten, sowohl für Radiofrequenzen als auch für optische Frequenzen vorgestellt. Diese vorbereitende Studie schliesst Plasmon Resonanzen an einzelnen Drähten und an einer Anordnung von neun Drähten ein. Es wird gezeigt, dass Plasmonresonanzen zu flachen Bandstrukturen mit vielen Moden führen, welche jedoch verschwinden, sobald relistische Verluste in den Metallen berücksichtigt werden. Bei Radiofrequenzen existiert eine fundamentale Bandlücke für Ez Wellen, welche für praktische Anwendungen sehr attraktiv ist. Es wird gezeigt, dass eine solche fundamentale Bandlücke - unter bestimmten Bedingungen - auch bei optischen Frequenzen vorkommt obwohl dann Metalle ihre Leitfähigkeit nahezu vollständig verlieren und durch eine komplexe Dielektrizitätskonstante beschrieben werden müssen.

Filtercharakteristiken von metallo-dielektrischen Photonenkristallstrukturen wurden mit Hilfe des Mehrfach Multipol Programms in Kombination mit modell-basierter Parameterabschätzung analysiert. Bei diesem Ansatz werden Verluste und Materialdispersion einbezogen und trotz relativ kurzer Rechenzeit sehr genaue Resultate erzielt. Ausgehend von diesen Untersuchungen wurden unterschiedliche, ultra-kompakte Bandpassfilter für den Telekommunikationsbereich entwickelt. Derartige Filter bestehen aus lediglich fünf Silberdrähten in einem optischen Wellenleiter. Sowohl stochastische als auch deterministische Optimierungsstrategien wurden eingesetzt um die gewünschten Filtercharakteristiken zu erhalten.

Um auf Photonenkristallen basierende Filter in integrierten optischen Schaltkreisen zu realisieren, wurden zwei Methoden vorgeschlagen: a) leitfähige Wände, welche die periodischen Randbedingungen einer Photonenkristallschicht ersetzen und b) Einbettung eines Photonenkristallfilters in einem konventionellen optischen Wellenleiter. Obwohl die metallischen Wände die Filtercharakteristik zerstören und die Verluste im Metall die Filterqualität reduzieren, ist es möglich, die ursprüngliche Filtercharakteristik wieder herzustellen, indem eine geeignete Optimierung durchgeführt wird, welche auch die Wandeffekte berücksichtigt.

Im Kapitel 5 werden scharfe Biegungen in Trenchwellenleitern (tiefgeätzte Rippen) analysiert, in welchen zwei Wellentypen ausbreitungsfähig sind. Dabei werden kleine,

lokale Photonenkristall eingebracht, um Abstrahlung zu unterdrücken. Mittels Optimierung wurden unterschiedliche Anordnungen mit niedriger Reflexion, geringer Abstrahlung und Modenumformung und demgemäss hoher Transmission gefunden. Drei unterschiedliche Typen von Biegungen wurden untersucht und verglichen: Strukturen basierend auf Spiegeln, Strukturen basierend auf Resonatoren und Strukturen mit kleinen lokalen Photonenkristallen. Letztere unterdrücken die unerwünschte Abstrahlung und reduzieren gleichzeitig die Probleme der Fabrikationstoleranzen.
Im Kapitel 6 werden unterschiedliche Definitionen der Auflösung von Schichten mit Metamaterialien mit negativem Brechungsindex („NIM Schicht", sogenannte „Pendry Linse") und von klassischen optischen Linsen vorgestellt und anschliessend benutzt um die maximale Auflösung derartiger Strukturen zu berechnen. Mehrere numerische Programme – basierend auf Gebiets- und Randdiskretisierungsmethoden, welche im Zeit- und Frequenzbereich arbeiten – werden angewendet und verglichen. Es wird gezeigt, das „Superresolution" sehr stark von der Definition der Auflösung abhängt und dass nicht nur NIM Schichten, sondern auch klassische Linsen (mit hohem Brechungsindex) Superresolution aufweisen können, aber nur wenn die Distanzen von Quell- und Bildpunkten von der Oberfläche der Schicht bzw. Linse kürzer als die Wellenlänge sind.

1 Introduction

1.1 Photonic crystals and their applications

To meet the requirements of high speed communication and to keep up with the internet's exploding need for bandwidth, technologists are looking for some substitutions to replace electronic switches that are the "bottle neck" of high speed communication systems, with faster and much smaller optical devices. A promising candidate for this is the photonic crystals [1].

Photonic crystals are artificial materials consisting of nano-size structures arranged periodically on regular lattices, as first proposed by Yablonovitch who found that the electromagnetic band gap for light would prohibit spontaneous emission [2]. Almost at the same time, S. John found that light could be localized when disorder is present in a periodic medium [3]. These discoveries opened a new door to control light and therefore attracted much attention of scientists from different areas such as solid-state physics, semiconductor physics, quantum optics, mechanics, nanostructures etc.

From careful physical analysis, one can see that the light propagating in photonic crystal structures is periodically modulated when the dielectric constant (and also the refractive index) is periodically changed in space. When the dielectric contrast of two media is big enough and the lattice constant is comparable with the operating wavelength in the lower refractive index medium, photonic band gap(s) are observed in the dispersion curves. Within the band gaps, light can not propagate and therefore it is reflected almost perfectly at the surface of a photonic crystal [5]. The appearance of band gaps can modify the density of states of the optical field due to the periodicity of the crystal. The optical density of states, which is responsible for optical properties of the material, is proportional to the square of the frequency in uniform materials. With the help of photonic crystals, the optical density of states can be controlled and thus, the optical properties can be tailored [6]. When defects are introduced, light can be localized and guided in such structures, which provide the means to create optical circuits and other small, low-power devices that can carry, route, and process data at the speed of light [7].

Up to now, many new structures based on photonic crystals have been proposed showing high performance compared with traditional ones. Some promising structures are the following.

1) High performance mirrors. As the wave within the band gap can not propagate, the structure can reflect the light from any incident direction. The reflectivity almost can reach 100% [8].
2) Photonic crystal waveguides. Conventional waveguides undergo energy loss at sharp bends. Theoretical and experimental studies show that photonic crystal waveguide bends may have almost 100% transmission over a wide band region [9].
3) High quality micro-cavities. When defects are introduced into photonic crystals, it is possible to have defect states in the structure with a large density of states and high quality factor. Cavities with theoretical quality factors above 20000 have been designed and experimental values as high as 4000 have been demonstrated for photonic crystal cavities [10].
4) Photonic crystal fiber. When the cladding of a fiber is made of photonic crystals, light can be confined in the core by the band gap

effect. Therefore, the core can have a lower refractive index than the cladding, and light can be guided even in air. These special characteristics cannot be achieved with standard optical fibers [11].

5) Photonic crystal super-prism. The super-prism effect [12] occurs due to the peculiar dispersion characteristics in the frequency range above the first photonic band gap. It allows wide-angle deflection of a light beam by a slight change of the wavelength and of the incident angle. Basically, these phenomena arise from the high anisotropy of the dispersion surface of a photonic crystal. A prism made up of a photonic crystal would have a dispersion capability 500 times stronger than a prism made of a conventional medium. These phenomena have been proposed to be utilized for wavelength division multiplexing (WDM) and for super-lens applications [13].

Besides the above mentioned applications, photonic crystals could also be used for threshold-less lasers [14], optical switches [15], optical amplifiers [16], optical filters [17] etc. with recently discovered phenomena [18]. With further understanding of these physical phenomena and the improvements of fabrication and experimental technologies, more and more new applications are expected to become known and are to be exploited in the near future.

1.2 Metallic photonic crystals

Photonic crystals consisting of metallic materials exhibit a number of interesting properties at radio and optical frequencies [19]. For example, one-dimensional photonic crystals composed of a stack of alternating layers of metallic and dielectric materials can be designed to be transparent over a tunable range of optical frequencies [20]. Three dimensional photonic crystals have been demonstrated to make inductive and capacitive screens for filtering and imaging applications [21]. High efficient microwave reflectors [22], high quality factor resonators [24] and high directivity antennas [25] have been realized by metallic photonic crystals in the microwave region. In addition, metallic photonic crystals are successfully used in accelerator systems [23]. Compared with dielectric photonic crystals, metallic photonic crystals have more promising characteristics as follows.

1) Structures made by metallic photonic crystal devices may have more compact sizes than their dielectric counterparts. Since metals are more reflective than dielectrics over a wide range of wavelengths, less photonic crystal layers are required to establish band gaps [26].
2) Studies show that when metals are introduced into photonic crystals, they may enlarge the band gaps, which leaves more margins to the applications [27].
3) Metallic photonic crystals with Ez-polarization have a fundamental band gap that covers the frequency range from zero to cut-off frequency, implying that there is no low-frequency limit for metallic photonic crystals [28, 29].
4) Flat bands in metallic photonic crystals characterize modes with very low group velocity, which can be used for low-threshold and high power lasers. Furthermore, these modes can be used for the excitation of surface plasmon polaritons [30], thus would be good candidates for the wiring of future optoelectronic integrated circuits [31].

In general, the applications of metallic photonic crystals can be classified in two areas: long wavelength and optical region. At the long wavelength region, where metals are more reflective and have less absorption, metallic photonic crystals could be used to improve the performance of microwave devices with relatively low costs as stated above. At optical frequencies, metals have stronger nonlinearity than other optical materials, thus metallic photonic crystals can be used to enhance some nonlinear optical phenomena [32]. On the other hand, because of absorption and dispersion at optical frequencies, metallic photonic crystals are not suitable for general optical devices. In addition, some applications with metallic photonic crystals like sensors, filters that need high temperature operation environment may be possible [33] since metals have higher melting points than other materials.

In this thesis, some fundamental issues of metallic photonic crystals are discussed in the chapters 2 and 3.

1.3 *Numerical methods for photonic crystals*

As the lattice constant of photonic crystal structures is comparable with the wavelength in the structure, many devices can be minimized with the help of photonic crystal structures, particularly at optical frequencies. Miniaturization of parts is the basis for small systems. The trend towards miniaturization is mainly motivated by the desire of obtaining higher speed in the processing of the optical signals [34]. Miniaturization necessitates optimum layout of structures which in turn cannot be accomplished without the use of design methodologies that are based numerical calculation of electromagnetic fields. In this section, numerical methods for small systems of photonic crystals are discussed.

Many numerical methods have been developed and applied to study photonic crystals, namely the Plane Wave Method (PWM) [35], the Transfer Matrix Method (TMM) [36], the Finite Difference Time Domain (FDTD) method [37], the Finite Element Method (FEM) [38], the MMP [39] etc. However, depending on the problems to be solved, not all methods are suitable, flexible, and efficient for the numerical modeling of photonic crystals.

The PWM is based on the discrete Fourier series that lead to a plane wave expansion basis to solve Maxwell's equations [40]. PWM was the first method that was used to calculate band diagrams of photonic crystals with a frequency independent dielectric function. The accuracy of the solution is determined by the number of plane waves used in the calculations. When the dielectric contrast is big (i.e. >3), PWM has very slow convergence because of large fluctuations of the truncated series approximating the actual dielectric constant and fields. In this case, many plane waves are needed which lead to large matrix equations; When the calculated structure contains defects, the super-cell method may be applied which leads to huge numbers of plane wave. In particular when this method is applied to problems with frequency-dependent materials, for instance, metallic photonic crystals as in this thesis, the performance is not good although many authors try to exploit special forms of the dielectric function to obtain a standard eigenvalue problem [41]. One can therefore safely state that this method is currently limited to band diagram calculations for materials without loss and dispersion.

To overcome the drawbacks of PWM, Pendry and coworkers introduced the TMM [42]. This method essentially consists of a layer by layer calculation of the field. Therefore, not only band diagrams but also the calculation of transmission and reflection coefficients for incident electromagnetic waves on finite photonic crystal

structures can be handled. For photonic crystal structures with defects one uses a super-cell technique as in PWM [43]. In TMM, structures are assumed to have infinite width and effects of the actual finite width are neglected. Compared with PWM, TMM could be used to calculate metallic photonic crystal structures, i.e., materials with loss and dispersion, without numerical problems [43]. Currently, TMM method was used for the structures with periodicity in one or more direction.

FDTD is widely used for photonic crystal structures [44]. The method is formulated by discretizing Maxwell's curl equations over a finite volume as proposed by Yee in the 1960s [45]. Through centered difference approximations, the space and time derivatives of the electric and magnetic fields are formulated. Since FDTD works in time domain, this would permit one to study the dynamic behavior of photonic crystal structures. As all time-domain methods, FDTD has substantial problems with frequency-dependent material properties, i.e., dispersive and lossy media, like metals [46].

Besides FDTD, FEM is also widely used in both frequency and time domain for the analysis of photonic crystal structures [47]. It is well known that the unstructured mesh used in FEM is advantageous because it provides a better approximation of the material boundaries, but at the same time the mesh generation is crucial and has a strong influence on the results. When the computational domain is large, both FDTD and FEM are time and memory-consuming.

MMP is a well-developed method and has been widely and successfully used for photonic crystals [48, 49]. The method was initially proposed by Hafner in 1980 [50] as a special case of the Generalized Multipole Techniques (GMT) [51]. In MMP the field inside each computational domain is approximated by a series expansion of basis functions that fulfill Maxwell's equations analytically within the corresponding domains. Currently, plane waves, harmonic expansions, Bessel expansions, multipoles, Rayleigh expansions, etc. are used in MMP. When different basis functions (expansions) with different boundary conditions are used, various problems can be solved. For example, when Rayleigh expansions with periodic boundary conditions are used, one can deal with semi-infinite photonic crystal structures like those in the transfer matrix method. The advantage of MMP is that with the expansions mentioned above and superpositions thereof a large number of problems with complex geometry and functionality [52] can be solved. For example, waveguide discontinuities may be handled accurately and efficiently without any absorbing boundaries. Since MMP works in the frequency domain, periodic boundary conditions and dispersive materials can be handled without numerical problems.

Besides the features mentioned above, 2D problems in MMP need only a 1D boundary to be discretized, which reduces the numerical effort and computation time significantly. Additionally, MMP provides high accuracy because of its semi-analytic nature and exponential convergence behavior in the case of Hoelder-continuous boundaries. This is highly advantageous for numerical optimization.

Based on the advantages listed before, MMP is highly suitable for the research on 2D photonic crystal structures. A software platform is available based on MMP (MaX-1 [53]) which can also be linked to numerical optimizers. This software platform will be used in many of the investigations conducted in this thesis.

Optimization of photonic crystal structures

Because of the often counter-intuitive behavior of photonic crystal based devices and their unprecedented properties, the best way for photonic crystal design is to combine accurate field solvers with appropriate numerical optimizers [54]. Generally, two

design approaches are used: direct design based methods and inverse design based methods [55]. Direct design methods are based on trial and error and guided by knowledge and intuition, while inverse design methods are guided by a stochastic or deterministic optimization algorithm with constrains of physical intuition. Since the behavior of photonic crystal devices are sometimes very different from intuition, inverse design based methods are most often used. They were successfully tested for various photonic crystal devices such as low-loss photonic crystal waveguides [56], photonic crystal fibers [57], trench waveguide bends with photonic crystals [58] etc. Two types of optimizers are used with inverse design methods: stochastic optimizers and deterministic optimizers.

Among stochastic optimizers, Genetic Algorithms (GA) and Evolutionary Strategies (ES) are most promising [59]. GA and ES belong to the class of evolutionary algorithms. Since GA was developed by Holland in 1975 [60], GA and its derivatives have been widely applied to many problems in various areas of science and engineering, i.e., numerical optimization [61], machine learning [62], intelligent control [63], artificial life [64], image processing, pattern recognition [65], etc. The main advantage of stochastic optimizers such as GA and ES is that such optimizers are not trapped in local optima and need not to be started with a sufficiently good initial guess of the solution [66]. This really helps to save computation time and therefore design time when the conventional design rules fail or when there is not much prior design knowledge available as is the case in the structures investigated in this thesis.

As stochastic optimization is used to model uncertainty in the data by assuming that the input is specified in terms of a probability distribution, stochastic optimization models are also often computationally quite difficult, both from a practical perspective, as well as from the viewpoint of complexity theory [59]. In some cases, when a more or less reasonable solution was found from stochastic optimization and the relevance of the design variables is known, deterministic optimization is suitable for further optimization and fine-tuning of the initial solution. This can lead to faster convergence with smaller number of simulations than if stochastic optimization is used until the end. One important issue is that deterministic optimization may be misled by local optima and the number of simulations strongly increases with the total number of design variables. Usually, deterministic optimization is efficient when the design variable dimensions are low, i.e. not much higher than 5.

1.4 Outline of this work

The organization of this dissertation is as follows. In chapter 2, metallic photonic crystals at radio frequencies and at optical frequencies are investigated and general design rules for metallic photonic crystals are presented. In chapter 3, ultra-compact metallo-dielectric photonic crystal filters are designed and analyzed using MMP, combined with the Model-Based Parameter Estimation technique. Material losses and dispersion are taken into account. Furthermore, simple stochastic and deterministic optimization techniques are employed to obtain the desired characteristics. In chapter 4 - to realize the structures designed in chapter 3 - two methods a) using conducting walls to replace periodic boundary conditions of the photonic crystal slab and b) embedding a photonic crystal filter in a conventional waveguide structure are presented. Considering photonic crystal applications for future optical communication systems, sharp trench waveguide bends in dual mode operation with small photonic crystals for suppressing radiation are analyzed in chapter 5. In chapter 6, the

resolution of negative index material slabs are discussed because such metamaterials currently attract much interest and because they are fabricated very much like metallic photonic crystals. Finally, conclusions are presented, and a short outlook is given.

References

[1] http://www.technologyreview.com

[2] E. Yablonovitch, *Phys. Rev. Lett.* **58**, 2059 (1987).

[3] S. John, *Phys. Rev. Lett.* **58**, 2486 (1987).

[4] J. D. Joannopoulos, R. D. Meade, and J. N. Winn, *Photonic Crystals – Molding the Flow of Light*, Princeton University Press, Princeton (1995).

[5] http://www.technologyreview.com/read_article.aspx?id=12258&ch=infotech

[6] http://physicsweb.org/articles/world/13/8/9

[7] Gary Taubes, *Science* **278**, 5344, 1709-1710 (1997).

[8] Elliott R. Brown, Oliver B. McMahon, and Christopher D. Parker, *Lincoln Lab. J.* **11**, 2 (1998).

[9] A. Mekis, J. C. Chen, I. Kurland, S. Fan, P. R. Villeneuve, and J. D. Joannopoulous, *Phys. Rev. Lett.* **77**, 3787 (1996).

[10] T. Yoshie, J. Vuckovic, M. Loncar, A. Scherer, H. Chen, D. Deppe, *Lasers and Electro-Optics, 2002, CLEO'02 Technical Digest* **1**, pp. 191 (2002).

[11] J. C. Knight, J. Broeng, T. A. Birks, and P. St. Russell, *Science* **282**, 1476 (1998).

[12] M. Notomi, T. Tamamura, Y. Ohtera, O. Hanaizumi, and S. Kawakami, *Phys. Rev. B* **61**, 7165 (2000).

[13] A. S. Jugessure, A. Bakhtazad, A. G. Kirk, L. Wu, T. F. Krauss, R.M. De La Rue, *Opt. Express* **14**, 1632-1642 (2006).

[14] M. Sigalas, C. T. Chan, K. M. Ho, and C. M. Soukoulis, *Phys. Rev. B* **52**, 11744 (1995).

[15] G. Pan, R. Kesavamoorthy, and S. A. Asher, Phys. Rev. Lett. **78**, 3860 (1997).

[16] Kim, M Hacker et al, *IEEE MTT-S International digest*, pp. 543-546 (1999).

[17] Cui xudong, Christian Hafner, Ruediger Vahldieck, *Opt. Express* **13**, pp. 6175-6180 (2005).

[18] F. J. Garcia-Vidal and J. B. Pendry, Phys. Rev. Lett. **77**, 1163 (1996).

[19] M. Scalora, M. J. Bloemer, A. S. Pethel, J. P. Dowling, C. M. Bowden and A. S. Manka, *J. Appl. Phys.* **83**, 2377 (1998).

[20] M. J. Bloemer and M. Scalora, *Appl. Phys. Lett.* **72**, 1676 (1998).

[21] J. Shah, K. D. Moeller, and H. Grebel, *J. Opt. Soc. Am. A* **22**, 2 (2005).

[22] A. R. McGurn and A. A. Maradudin, *Phys. Rev. B* **48**, 17576 (1993).

[23] D. R. Smith, S. Shultz, N. Kroll, M. Sigalas, K. M. Ho, and C. M. Soukoulis, *Appl. Phys. Lett.* **65**, 645 (1994).

[24] C. J. Maggiore, A. M. Clogston, G. Spalek, W. C. Sailor, and F. M. Mueller, *Appl. Phys. Lett.* **64**, 1451 (1994).

[25] E. R. Brown and O. B. McMahon, *Appl. Phys. Lett.* **68**, 1300 (1996).

[26] E.Oezbay and B. Temelkuran et al., *Appl. Phys. Lett.* **69**, 25 (1996).

[27] E. R. Brown and O. B. McMahon, *Appl. Phys. Lett.* **67**, 2138 (1995).

[28] Ovidiu Toader and Sajeev John, *Phys. Rev. E* **70**, 046605 (2004).

[29] Mehmet Bayindir, E. Cubukcu, I. Bulu, T. Tut, and E. Ozbay, *Phys. Rev. B* **64**, 195113 (2001).

[30] Sergey I. Bozhevolnyi, John erland, Kristjan Leosson, Peter M. W. Skovgaard and Jorn M. Hvam, *Phys. Rev. Lett.* **86**, 3008 (2001).

[31] Sergey I. Bozhevolnyi and Valentyn S. Volkov, Kristjan Leosson and Alexandra Boltasseva, *Appl. Phys. Lett.* **79**, 8 (2001).

[32] F. J. Garcia-Vidal and J. B. Pendry, *Phys. Rev. Lett.* **77**, 1163 (1996).

[33] Chul-Sik Kee and H. Lim, Young-Ki Ha, Jae-Eun Kim, and Hae Yong Park, *Phys. Rev. B* **64**, 085114 (2001).

[34] T. F. Krauss and R. M. De La Rue, *Progress Quantum Electron.* **23**, No.2, 51-96 (1999).

[35] K. M. Ho, C. T. Chan, and C. M. Soukoulis, *Phys. Rev. Lett.* **65**, 3152 (1990).

[36] M. Sigalas, C. M. Soukoulis, E. N. Economou, C. T. Chan, and K. M. Ho, *Phys. Rev. B* **48**, 14121 (1993).

[37] A. Taflove, *Computational electrodynamics, the Finite-Difference Time-Domain Method*, Artech House, Boston, London (1995).

[38] Pelosi G., Cocchi A. Monorchio A, *IEEE Trans. On Antenna and Propagation* **48**, pp. 973-980 (2000).

[39] E Moreno, D Erni, C Hafner, *Phys. Rev. B* **65**, 155120 (2002).

[40] A. R. McGurn and A. A. Maradudin, *Phys. Rev. B* **48**, 17576 (1993).

[41] V. Kuzmiak, A. A. Maradudin, and F. Pincemin, *Phys. Rev. B* **50**, 16835 (1994).

[42] J. B. Pendry and A. MacKinnon, *Phys. Rev. Lett.* **69**, 2772 (1992).

[43] I. El-Kady, M. M. Sigalas, R. Biswas, K. M. Ho, and C. M. Soukoulis, *Phys. Rev. B* **62**, 15299 (2000).

[44] Guida, G., T. Brillat, A. Ammouce, F. Gadot, A. de Lustrac, and A. Priou, J. *Appl. Phys.* **88**, 4491 (2000).

[45] K. S. Yee, *IEEE Trans. Antennas Propagat.* **14**, 302 (1966).

[46] Qiu M.; He S., *Physics Letters A* **282**, pp. 85-91(2001).

[47] Coccioli, R. Itoh, T. Pelosi, G. In *Microwave Symposium Digest, IEEE MTT-S International* (1997).

[48] Esteban Moreno, F. J. García-Vidal and L. Martín-Moreno, *Phys. Rev. B* **69**, 121402 (2004).

[49] Esteban Moreno, *Diss.ETH Nr.* **14553**, ETH Zurich (2002).

[50] Christian Hafner, *Diss.ETH Nr.* **6683**, ETH Zurich (1980).

[51] T. Wriedt, editor, *Generalized Multipole Techniques for Electromagnetic and Light Scattering*, Elsevier, Amsterdam (1999).

[52] D. Karkashadze, R. Zaridze, A. Bijamov, Ch. Hafner, J. Smajic, D. Erni, *ACES Journal* **19**, pp. 10-21 (2004).

[53] http://max-1.ethz.ch.

[54] J. Smajic, Ch. Hafner, D. Erni, *J. Opt. Soc. Am. A* **21**, 2223-2232 (2004).

[55] J. M. Geremia, Jon Williams, and Hideo Mabuchi, *Phys. Rev. E* **66**, 066606 (2002).

[56] P. Borel, A. Harpøth, L. Frandsen, M. Kristensen, P. Shi, J. Jensen, and O. Sigmund, *Opt. Express* **12**, 1996-2001 (2004).

[57] E. Kerrinckx, L. Bigot, M. Douay, and Y. Quiquempois, "Photonic crystal fiber design by means of a genetic algorithm," *Opt. Express* **12**, 1990-1995 (2004).

[58] Cui Xudong, Christian Hafner, Ruediger Vahldieck, Franck Robin, *Opt. Express* **14**, No. 10, pp. 4351-4356 (2006).

[59] J. Froehlich, *Diss. ETH Nr.* **9225**, ETH Zurich (1997).

[60] J. H. Holland, *Adaption in Natural and Artificial Systems*, MIT Press, New York (1968).

[61] Yan Yu and M. C. Schell, *Medical Physics* **23**, pp. 2085-2091 (1996).

[62] C.-Y. LEE, S. Piramuthu and Y.-K. Tsai, *Job shop scheduling with a genetic algorithm and machine learning*, Taylor & Francis Group (1997).

[63] Passino, K.M., *IEEE Spectrum* **32**, pp. 55-62 (1995).

[64] M Kawata, Y Toquenaga, *Trends in Ecology & Evolution* (1994).

[65] Sang Kyoon Kim, Dac Wook Kim, Hang Joon Kim, *Proceedings in international conference on image processing* **2**, pp. 661-664 (1996).

[66] Christian Hafner, Cui Xudong, Ruediger Vahldieck, *International J. Microwave and Opt. Technol.* **1** (2006).

2 Metallic photonic crystals at radio frequency and optical frequency

Radio frequency (RF) models are frequently used for testing concepts that should finally work at optical frequencies. Since metals loose their conductivity at optical frequencies (OF), such models are of questionable value. In this chapter, the simulations of two-dimensional photonic crystals (PhCs) consisting of arrays of metallic wires at RF and at OF are presented to show the limitations of RF models. The most important features of photonic crystals consisting of parallel metallic wires at optical frequencies are analyzed using a reliable and accurate numerical method. For a better understanding of the fundamental effects, the scattering of electromagnetic waves at metallic wires both in the radio frequency and in the optical frequency range are outlined first. This preparatory study includes plasmon resonances of a single wire and of a set of 9 wires. It is demonstrated that plasmon resonances cause flat band structures with many modes rather than photonic band gaps. At radio frequencies, the existence of a fundamental band gap for Ez waves is highly attractive for practical applications. We demonstrate that a fundamental band gap also exists at optical frequencies (under certain conditions) although metals lose their conductivity almost entirely and must be described by a complex permittivity.

2.1 Introduction

There are numerous attractive applications in engineering for a "perfectly reflecting wall", i.e., a perfect mirror, such as in a waveguide or resonator. At RF, metals are used when a "perfect wall" is desired. Here, the (almost) total reflection of an electromagnetic wave at a metallic object is due to the high conductivity σ, i.e., due to the high imaginary part ε'' of the permittivity ε:

$$\varepsilon = \varepsilon' + i\varepsilon'' = \varepsilon_0 \varepsilon_r + i\sigma / \omega \tag{1}$$

where ω is the angular frequency and ε_0 is the free-space permittivity. As a consequence, strong electric currents are observed near the surface of the conductor and the electromagnetic field decays essentially exponentially with the distance from the surface. This decay is referred to as skin-effect and is characterized by the skin depth. When the metallic object is big compared with the skin depth, one usually describes it as a Perfect Electric Conductor (PEC), i.e., it is assumed that the conductivity is infinite. Then, no losses are present in the conductor and the skin depth is zero as well as the entire electromagnetic field inside the conductor. Such PEC models are frequently used because they drastically simplify the models and hence the numerical computations.

Unfortunately, metals loose their conductivity at OF due to the mass of electrons. This can be seen from measurements [1, 2] but also from the well-known Drude model:

$$\varepsilon(\omega) = \varepsilon_0 \left(1 - \frac{\omega_p^2}{\omega(\omega + i/\tau)} \right) \tag{2}$$

where ω_p and τ are real parameters that are characteristic for the material. It is evident from (2) that the real part of the permittivity becomes negative for some frequency range. For silver, a negative real part is obtained for wavelengths longer than 327 nm,

i.e. for blue light down to red and infrared. Above 350 nm, the imaginary part is considerably smaller than the absolute value of the real part. The negative real part gives rise to the well-known plasmon effect [3] with attractive applications.

The existence of photonic band gaps in PhCs has been demonstrated by numerous simulations and experiments [5-7]. What makes PhCs most attractive in optics is the fact that no light may penetrate a PhC within the band gap, i.e., a PhC can act similar to a "perfect wall" within some frequency range. By properly selecting the geometry and material properties, one can design a PhC that provides total reflection within the desired frequency range. Dielectric PhCs at OF are composed of materials that may be described by a complex permittivity with a positive real part and a much smaller imaginary part. Since undesired material losses are mainly caused by the imaginary part, one tries to find materials with an imaginary part that is as small as possible. Furthermore, one usually sets the imaginary part equal to zero because this considerably simplifies the mathematical description and the numerical models. Effects caused by material losses are then considered as secondary although they are of high importance for practical applications.

At RF, currently much work is done on metallic PhCs, i.e., on artificial crystals consisting of metallic wires - although a simple metallic plate is an almost perfect mirror for these frequencies. The main motivation for metallic PhC research is the promise of a "perfect lens" that might be obtained from a simple slab of "negative index" or left-handed" metamaterials [8, 9, 10]. This structure will be considered in more detail in chapter 6. Currently, metallic PhCs provide the simplest way toward such metamaterials [11, 12]. For this kind of applications, the PhCs are operated outside the band gap. However, since we know that the PEC approximation of a metal is not valid at all at OF, it is obvious that these investigations do not carry too much value in the optical domain. In other words, an attractive PEC PhC configuration at RF is no guarantee that this configuration will also be attractive at OF. In fact, it is not even clear if any metallic PhC configuration might be of any practical value. Therefore, numerical simulations will be provided in the following to shed some light on this question.

Typically, several PBGs occur for a given PhC – provided that the dielectric contrast, i.e., the ratio of highest refraction index divided by the smallest refraction index is big enough -, but the lowest band gap is of highest value for most of the practical applications. When metals are introduced, the dielectric contrast is no longer real valued. For a loss-free model with metallic rods - described by a negative permittivity and a background material of positive permittivity - the contrast becomes imaginary. Beside this, the procedure of the band diagram computation and that of the PBG evaluation remains the same. It should also be mentioned, that many codes used in the computation of PhCs cannot handle metallic PhCs at OF because they restrict the permittivity to positive real values. In the following computation the focus is on the first PBG because it is the most important one in practice. It will be demonstrated that a fundamental PBG, i.e., a PBG without any lower frequency limit exists not only for PEC PhCs at RF, but also for PhCs made of realistic metallic rods with negative permittivity – provided that the absolute value of the contrast is high enough.

2.2 Metallic wires

In order to better understand metallic photonic crystals made of an infinite set of parallel metallic wires, the scattering of a plane wave at a single metallic wire of circular cross section is considered first, which is one of the simplest problems in the

context of this thesis and one that can be solved with very high accuracy. It is assumed that the wire is parallel to the z axis and that the plane wave propagates perpendicular to this axis. Two different polarizations exist that are often denoted as s or p polarization, as TM or TE waves, or as E or H waves. Unfortunately, these notations are differently defined in different books and papers. This often causes confusion. For this reason, the case where the electric field is parallel to the wire axis is called the "Ez" wave and the case where the magnetic field is parallel to the wire axis the "Hz" wave.

It is well known that the wire scatters a part of the incident wave. Although only the total field outside the wire may be measured, one often uses the Scattering Cross Section (SCS) that essentially is an integral over the scattered field only. The reason for this is that plane wave illumination is not available in measurements. Often one uses some beam-like excitation that illuminates the scatterer from one side and from measurements the radiated field is obtained in some other direction. This is done in such a way that the direct illumination of the sensor by the incident beam may be neglected. Then, the dependence of the measured signal on the frequency is proportional to the frequency dependence of the SCS - as long as the angular distribution of the scattered field remains constant. In this thesis the integral of the total scattered power is calculated instead of the SCS. This integral is proportional to the SCS and to the power density of the incident plane wave. Note that the absolute values of these integrals (and of the SCS) are not important because they are not measured anyway. For this reason, we use arbitrary units in the corresponding plots.

2.2.1 Metallic wires at radio frequency

At RF, the conductivity of metallic wires is usually so big that a strong skin effect is obtained. As a result, reasonable results are obtained under the assumption that the wire is a *perfect electric conductor*, i.e., the electromagnetic field inside is set to zero and therefore, the tangential components of the electric field on the surface must be zero as well, whereas the tangential components of the magnetic field can be non-zero because of surface currents.

It is well known that the SCS of a PEC wire is much higher in the Ez case than in the Hz case when the diameter of the wire is small compared with the wavelength. This is shown in Fig.2.1. Note, for a first comparison it is assumed that very thin PEC wires also exist at OF although it is known to the author that no appropriate materials exist. The main reason for this assumption is that these results are compared with more realistic computations of silver wires in the following to show the differences. Scaling the results shown in Fig.2.1 by multiplying both the diameter of the wire and the wavelength by a sufficiently big factor (of the order of 10^5), the results are shifted into the RF range, where they become more realistic, i.e., a PEC is then a good approximation for copper or silver.

As illustrated in Fig.2.1, the SCS of a thin PEC wire increases very much (factor >10 when the radius is doubled) for the Hz case, whereas it increases not much (factor <2 when the radius is doubled) for the Ez case. Since the SCS for the Ez case is very high even when the radius is much smaller than the wavelength, an array of parallel thin wires acts like a wall when the distance between the wires is small enough. This effect is well known to RF engineers and it is often used in antenna design. Fabricating a metallic PhC at RF, it is therefore expect that a band gap exists for the Ez case when the wavelength is sufficiently long (compared with the period), i.e., for frequencies from zero up to a certain maximum frequency. This will be verified in the following.

2.2.2 *Metallic wires at optical frequencies*

As was already mentioned, the conductivity of metals is lost at OF. Instead of a high conductivity, i.e., a permittivity with a relatively high imaginary part, one observes a complex permittivity that is strongly frequency dependent and may have an imaginary part that is smaller than the absolute value of the real part. Furthermore, for some frequency range the real part even becomes negative as described by the Drude model (2).

When we repeat the computations illustrated in Fig.2.1 using measured data of silver instead of the PEC assumption for the wire, we obtain Fig.2.2. As one can see, the behavior is much different from the PEC case. First of all, a considerable increase of the SCS is observed also for the Ez case. Second, the SCS for the Hz case is now bigger than the SCS for the Ez case for some frequency range. Slightly above 350nm one can see a nice peak for the Hz case that is caused from the well-known plasmon effect. As one can see, the plasmon resonance shifts toward longer wavelengths, when the radius of the wire is increased. Furthermore, the resonance becomes broader.

For a better understanding, we compute the total scattered power for hypothetical wires with arbitrary, complex permittivity and plot the results over the complex permittivity plane (see Fig.2.3). Now, we obtain a very strong peak near $\varepsilon_r = -1$. For the theoretical case of an infinitely thin wire, this peak is a singularity at $\varepsilon_r = -1$. Since a macroscopic model is used for describing the material properties, such computations are not realistic at all. For increasing radii, the macroscopic model becomes more realistic. Then, the peak moves along the real axis toward more negative values. At the same time, one obtains a finite resonance peak that becomes broader. At sufficiently big diameters, one observes additional resonances as one can see in Figs.2.4 and 2.5.

Since all currently known materials exhibit a frequency dependence with a rather big imaginary part, the observed plasmon resonances are much less pronounced. As one can see from Figs.2.2 and 2.5, even for a good conductor such as silver with an imaginary part of the relative permittivity in the order of 0.1, the additional peaks for wires with bigger diameters are not observed in measurements of realistic wires. Furthermore, one can see from Fig.2.2 that the maximum SCS at plasmon resonance is not bigger than the SCS of the Ez case at sufficiently long wavelengths.

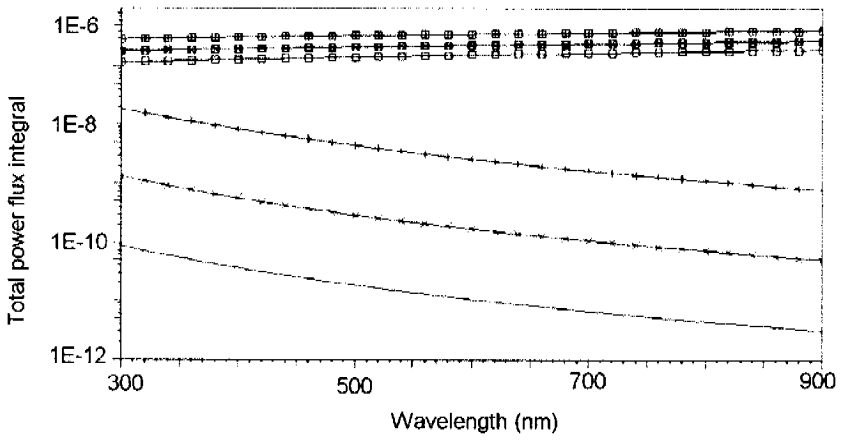

Fig.2.1 Total power flux integral over the scattered field (scattered power) versus wavelength for circular PEC wires of radius 5nm (line), 10nm (x), 20nm (+) for Ez waves (square) and Hz waves (no marker).

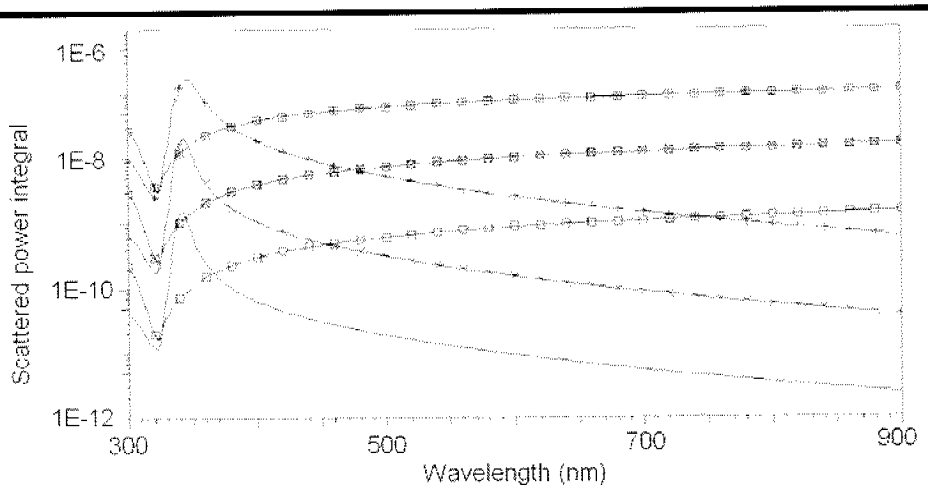

Fig.2.2 Scattered power integral versus wavelength for silver wires of radius 5nm (neither + nor x marker), 10nm (x marker), 20nm (+ marker) for Ez waves (square marker) and Hz waves (no square marker). For the material properties of the wire, measured data of Johnson and Christie[1] were used.

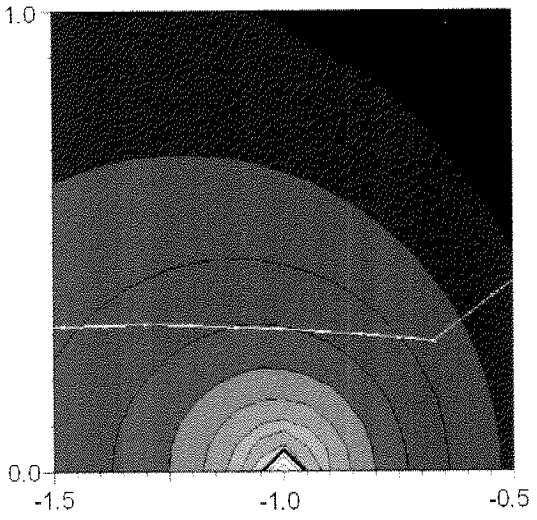

Fig.2.3 Scattered power integral for a thin wire (diameter = wavelength/100) of complex permittivity, illuminated by an Hz wave. Plot drawn over the complex permittivity plane (relative values, ε_r). For the ISO lines, a logarithmic scale is used. Values on neighbor ISO lines differ by the factor 2. Because of the limited resolution of the plot, the extremely strong peak near -1 is only shown roughly. The white line is the trace of the measured frequency dependence of the complex permittivity of silver that was used for the computations of Fig.2.2.

The interactions of neighbor wires shows a much more complicated behavior considering an ensemble of several wires illuminated by an Hz wave (see Fig.2.6). Even for the relatively simple case of 9 wires on a square lattice one obtains rather many sharp resonances when the imaginary part of the permittivity is small enough, as one can see from Fig.2.7. Each resonance peak corresponds to a specific field pattern. Two examples are plotted in Fig.2.6. Figure 2.7 also shows that the sharp peaks disappear almost entirely when losses are present, i.e., when the imaginary part of the relative permittivity is of order 0.1 or even bigger.

For the loss-free case it is obvious that the number of plasmon modes for an infinite PhC tends to infinity. Thus, a very complicated band structure is to be

expected. Of course, we also expect that this cannot be observed when the losses are high. For well-known metals such as silver, copper, and gold the losses are always so high that higher order plasmon resonances are not observed.

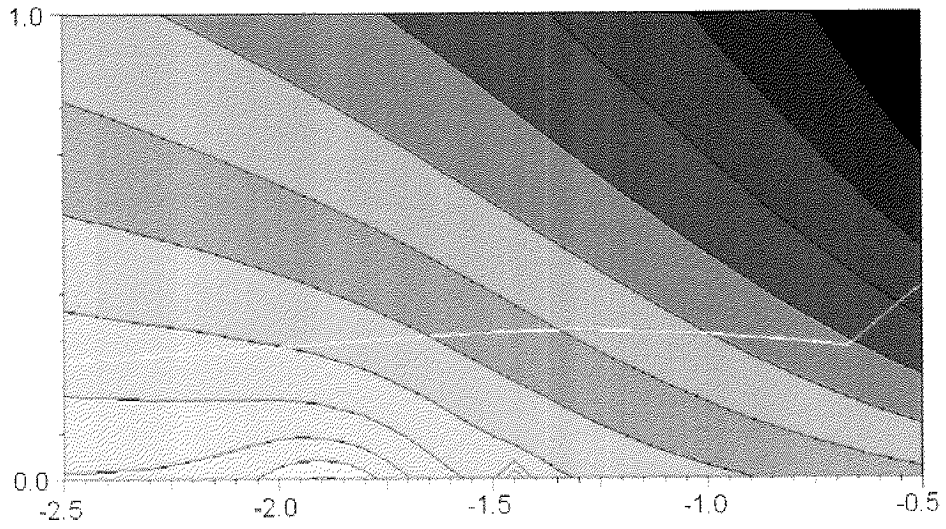

Fig.2.4 Same as in Fig.2.3 for a wire of diameter equal to the wavelength of the incident Hz wave.

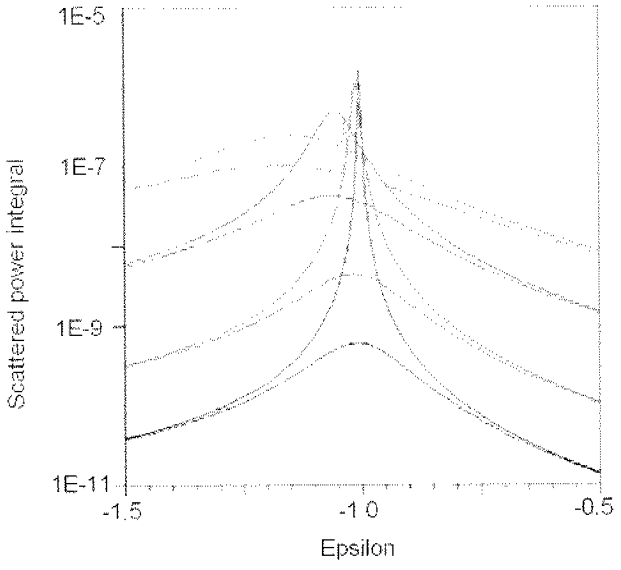

Fig.2.5 Scattered power integral for wires of different diameters D (black: D = wavelength/100, green: D = wavelength/50, blue: D = wavelength/20, red: D = wavelength/10) with complex permittivity, illuminated by an Hz wave. Curves with pronounced peaks: Imaginary part of the permittivity = 0, smooth curves: Imaginary part of the relative permittivity = 0.1.

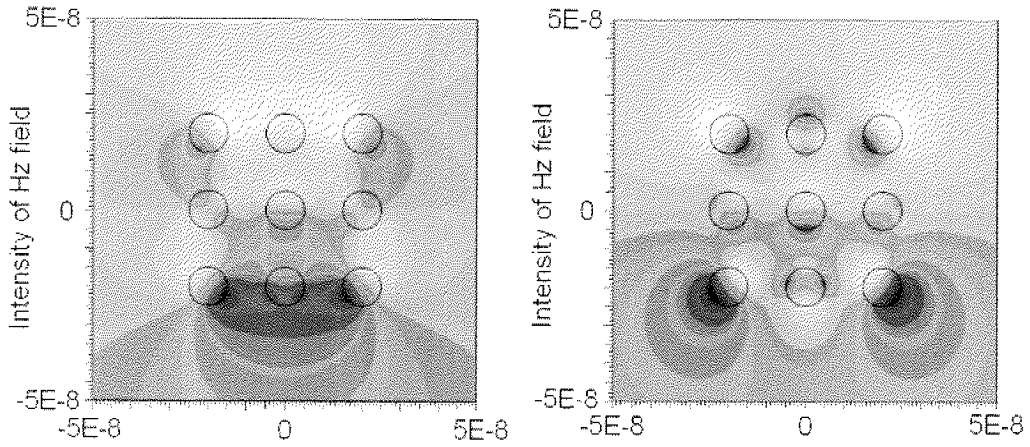

Fig.2.6 Intensity of the H_z field for a set of 9 circular wires (diameter = wavelength/100, lattice constant = wavelength/50) with negative permittivity, illuminated by an Hz wave. Bright/dark colors indicate strong positive/negative values of H_z. Red indicates values of H_z close to 0. Left hand side: Relative permittivity -1.1545, right hand side: Relative permittivity -0.874.

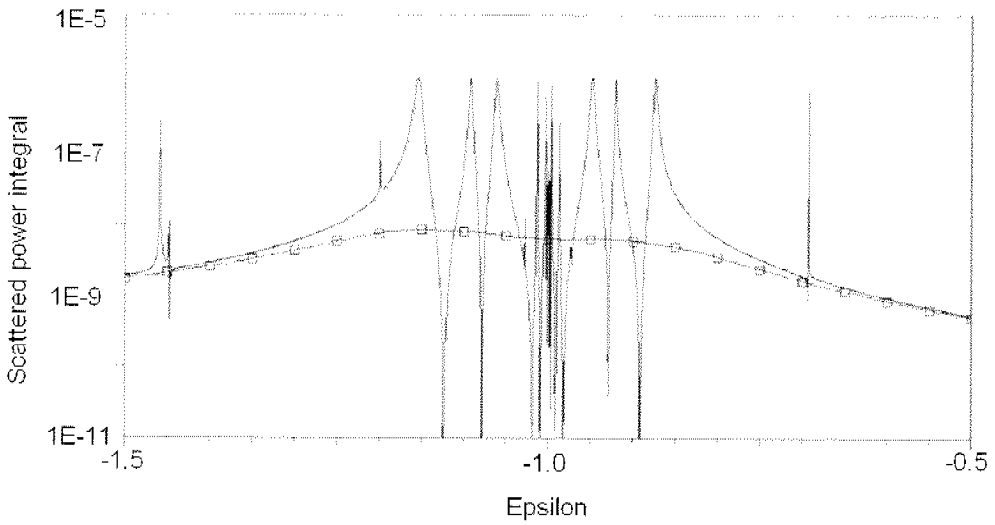

Fig.2.7 Scattered power integral for a set of 9 circular wires (see Fig.2.6) with complex permittivity, illuminated by an Hz wave. Curve without markers: Imaginary part of the permittivity = 0, curve with markers: Imaginary part of the relative permittivity = 0.1.

2.3 Metallic photonic crystals

2.3.1 At radio frequencies

As mentioned before, we can obtain reasonable approximations of the scattered field of good conductors at RF with an idealized PEC model. The simplest cases of the scattering in either plane illuminated by Ez or Hz waves at a thin, circular PEC wire already exhibit the main effects. Additional effects are observed when the geometry is changed, when losses are accounted for, when two or more wires interact with each other, or when the length of the wire is finite. Therefore, it is natural to study an infinite array of identical, circular PEC wires located on a regular lattice as the

simplest prototype of a photonic crystal that only exhibits the most fundamental effects. As for the single wire, such a model is only realistic for RF.

RF models are currently frequently studied for obtaining "negative index" or "left handed" metamaterials that promise the construction of a "perfect lens" [17, 18, 19] and will be considered in chapter 6. Such metamaterials are usually constructed using metallic wires on a periodic lattice, i.e., they can be considered as metallic photonic crystals. For this reason, almost all work done on metallic PhCs considers the wires as PECs, i.e., it is restricted to the RF range. In the previous section we found that PEC models only provide rough hints for the scattering at realistic wires at OF. Therefore, a more detailed analysis of realistic materials is essential. Before we start with this, we outline the most important observations for 2D PhCs consisting of parallel PEC wires.

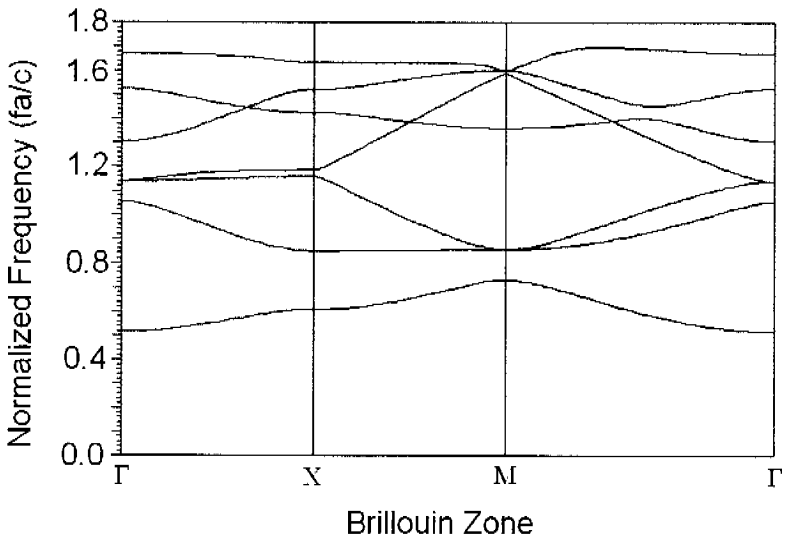

Fig.2.8 Band diagram for Ez waves on a PEC PhC consisting of circular PEC cylinders in air on a square lattice. $r/a = 0.187$, where a is the lattice constant and r is the radius.

It has been shown [20, 21, 22] that a fundamental PBG exists for PhCs consisting of thin PEC wires in the Ez case (see Fig.2.8), whereas no such band gap is observed for the Hz case (see Fig.2.9). Beside the fundamental PBG that extends from zero frequency to some maximum frequency, one also may have PBGs (for both Ez and Hz modes) at higher frequencies that are less attractive because this corresponds to smaller lattice constants are very difficulty to fabricate. Although we have considered only circular PEC wires, we assume that no essential new effects will be observed when the cross section of the wires is modified as long as the wires do not touch each other.

2.3.2 At optical frequencies

At OF, metals are characterized by a strongly frequency dependent, complex permittivity. For reasons of simplicity, we omit the losses for a first approximation although we know that losses play an important role in practice. As a consequence, we may consider the band diagrams using the well-known formalisms and procedures that are also used for dielectric PhCs and for PEC PhCs. The frequency dependence of the permittivity of metals has several consequences for the analysis. When frequency

domain codes like MMP are used, one can easily consider frequency-dependent material properties, i.e., no severe numerical problems are encountered. For the analysis of the band diagram one should keep in mind that the normalization of the diagrams is no longer reasonable. For example, when a square lattice with period a is considered, resonances are no longer observed at the normalized frequency $f_n = fa/c$ (where c is the velocity of light) for all values of a. Thus, one must separately compute the band diagram for each period a. Furthermore, the band diagrams may become very complicated [23] even when the frequency dependence of the material is as simple as in the Drude model. For this reason, we proceed in a way similar to the analysis of plasmon resonances in the complex permittivity plane (Fig.2.3), i.e., we assume that the permittivity of the wire has a constant value and compute the standard (normalized) band diagrams for such a fictitious material. Then, we repeat the computation for various permittivities.

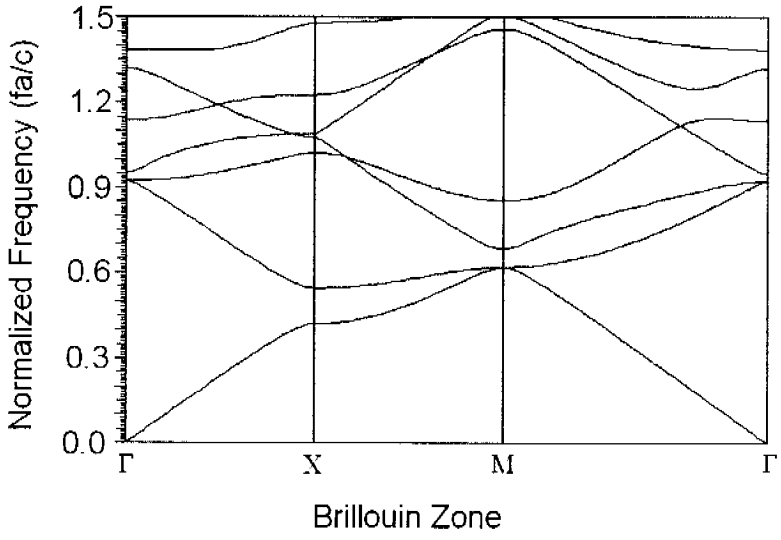

Fig.2.9 Same as in Fig.2.8 for Hz waves.

It is important to note that there are different methods to tackle PhCs with complex permittivities: 1) The imaginary part can be set equal to zero and a real-valued computation with a real eigenvalue search routine can be performed. Although this is possible for a numerical method, it may violate fundamental laws, namely the Kramers-Kronig relation [24]. When we set the imaginary part equal to zero, we obtain very sharp resonance peaks as in Fig.2.7. The numerical detection of such peaks may be computationally very demanding. For this reason, it is better - also from the numerical point of view – to take the imaginary part into account. 2) A complex description of the permittivity can also be used and then it is possible to search for the resulting complex eigenvalue, i.e., complex resonance frequency. Complex codes as MMP offer procedures for such a complex eigenvalue search, but this search is numerically demanding. When the complex eigenvalues are known, one should be able to plot the corresponding complex band diagrams. This is also rather difficult. Furthermore, it should be kept in mind that, measurements are usually performed by illuminating a finite PhC with an electromagnetic or light wave which is characterized by a certain real-valued frequency. As a result the frequency dependence of the scattered field is obtained, i.e., resonance curves rather than complex frequency values. When the losses are small enough, the real part of the complex resonance frequency is

typically close to the maximum of the resonance curve. The width of the resonance curve increases with the imaginary part of the complex frequency. Therefore, the following "hybrid" technique is most natural and mimics the measurement situation. 3) Here a complex permittivity is used in conjunction with a sweep of the frequency of a fictitious illumination. It is then possible to observe, for example, the total energy of the scattered field at some fictitious measurement point. The peaks of the resulting resonance curves are then detected numerically and used for plotting a "loss-free" band diagram. Our numerical tests have shown that all three methods deliver very similar band diagrams as long as the imaginary part of the permittivity is small compared with the absolute value. Therefore, in the following we focus on the methods 1 and 3 - that do not require complex eigenvalue solutions and complex graphic representations.

Sakoda [25] has used essentially the third method outlined above within a finite difference code. In order to obtain "realistic" results, i.e., results that are in agreement with the Kramers-Kronig relation, he used a Drude model of a metal. To our knowledge, no known metal is available that has a complex permittivity with a frequency dependence close to the one in Sakoda's simulations. For testing our codes, we reproduced Sakoda's results and obtained an excellent agreement. Beside the fact that the Drude model is often inaccurate at OF, band diagrams of PhCs with frequency dependent material properties only hold for a specific lattice constant a even when the normalized frequency fa/c is plotted. In Sakoda's computations, a was set in such a way that the real part of the complex permittivity is zero when fa/c is equal to 1. In fact, the Drude models are known to be very inaccurate when the real part is close to zero. Furthermore, when this happens, the assumption that the imaginary part of the permittivity is small compared with the absolute value is not valid. Therefore, such results are of questionable value.

For the design of a metallic PhC, the geometry must be optimized to produce the required transmission and reflection characteristics within a given frequency range. For the most simple case of a set of circular metallic rods arranged on a square lattice – as in Sakoda's paper, there are only two real parameters, i.e., the lattice constant a and the rod radius r. Furthermore, metal and the background material can be selected– with some restrictions imposed by the availability of corresponding materials. One of the most attractive features in the design of a PhC is the possibility to find a band gap over the entire frequency range of interest. In such a PhC, one then can easily embed waveguides and more complicated structures such as filters, resonators, power dividers, etc. Dielectric PhCs usually exhibit one or several bandgaps with a lower and an upper frequency limit. These band gaps often do not cover the entire frequency range of interest. As we will see below, metallic PhCs may exhibit a fundamental band gap – similar to the fundamental band gap of PEC PhCs at RF - that can cover the frequency range from infrared up to an upper limit in the visible light regime that depends on the material properties.

2.3.2.1 Hz modes

From the previous analysis of the scattering at a single wire, one might expect that plasmon resonance is the most important effect for obtaining a band gap, i.e., one might expect the most promising band diagrams when the relative permittivity of the rod is close to -1 for a free-space background material with relative permittivity +1. As one can see from band diagram computations of metallic PhCs described by the Drude model [23], one does not obtain a band gap in the frequency range where the relative permittivity of the rod is close to -1. Instead of this, one finds a flat band, i.e.,

a band that contains many modes corresponding to different plasmon resonances. The number of modes in the flat band is the higher the lower the imaginary part of the permittivity is. Therefore, it is obvious, that much more modes are obtained in unrealistic low-loss configurations than in realistic ones. The flat band modes are attractive because of the low group velocity associated with them. However, the flat band is almost the contrary of a band gap, i.e., the plasmon resonances within this band provide mechanisms for propagating waves through the crystal in all directions. Incidentally, this effect can already be observed for a very small finite PhC model with 9 rods as shown in Figs.2.6 and 2.7: When the angle of incidence is rotated, the field patterns in Fig.2.6 and the SCS curves in Fig.2.7 remain almost the same.

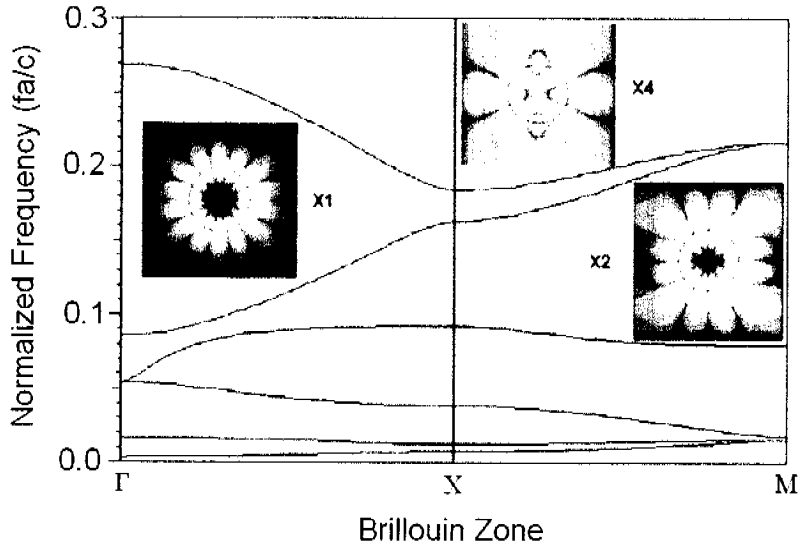

Fig.2.10 Band diagram for Hz waves on a PEC PhC consisting of circular cylinders (relative permittivity -1) in air on a square lattice. $r/a = 0.20$. Note that this diagram is not complete: Infinitely many additional higher order modes may be found near $fa/c = 0$. Insets: Hz field distribution for three modes at the X point. X1 is the first mode (lowest value fa/c) shown in the band diagram, X2 is the second one and X4 is the forth mode. Bright colors indicate a strong positive field, dark colors a strong negative field. The red area indicates low field values.

In order to obtain more information, we can also compute the band diagram for a fictitious PhC consisting of circular rods with relative permittivity -1 in a background medium with relative permittivity +1 as shown in Fig.2.10. Since the relative permittivity -1 is approximately obtained for a certain frequency for a given metal, one can consider fa/c as "normalized lattice constant" rather than as normalized frequency. This means that the diagram tells us what modes propagate in such a crystal at the given frequency depending on the size of the lattice constant a. It seems that no modes propagate when $fa/c = a/\lambda$, i.e., when a is very small compared with the wavelength λ. In fact, a flat band is observed here with infinitely many modes. Obviously, it is not possible to calculate characterize all modes. Furthermore, characterization of some of these modes it is very demanding– especially the modes that correspond to high order plasmon resonances - because a high numerical accuracy is required. As seen from the insets of Fig.2.10, high order modes are found close to $fa/c = 0$. When a realistic metal is used, the frequency or wavelength where the relative permittivity is near -1 is known. For example, for silver, this is near

882THz or 340nm. Since the lowest mode X1 (shown in Fig.2.10) has $fa/c = a/\lambda$ <0.01 at the X point, we obtain a < 3.4nm and r < 0.68nm. It is well known that the macroscopic description for silver is not valid for such small radii. Furthermore, it is currently not possible to fabricate PhCs with such a small lattice constant a. Thus, the consideration of the flat band near $fa/c = 0$ is only of theoretical interest.

We now can consider the band diagrams for fictitious PhCs with a negative permittivity different from -1 or with a complex one. When the relative permittivity is not close enough to -1, the plasmon effect does not play any role and the results become uninteresting. We therefore focus on the influence of losses, i.e., of the imaginary part of the permittivity. In the flat band area, the group velocity is very slow, which would offer attractive engineering applications. The slow group velocity is caused by strongly interacting plasmons on the surfaces of the wires. Therefore, we expect that losses play a very important role for these modes, i.e., even relatively small imaginary parts of the permittivity of the rods cause strong attenuation of the flat band modes. This assumption is also supported by the results of a small finite PhC illustrated in Fig.2.7, where the strong resonance peaks disappear as soon as losses are present. In fact, the higher order modes X1, X2 shown in Fig.2.10 disappear already for extremely small imaginary parts of the relative permittivity of the rods. For a realistic relative permittivity of -1 + 0.3i (silver at 340nm), even all of the modes shown in Fig.2.10 disappear. In fact, these modes may be traced in the complex plane and obtain a rapidly growing imaginary part with increasing loss. Thus, one will observe a "pseudo band gap", i.e., a band of modes with extremely high attenuation instead of the flat band for Hz modes in metallic PhCs. Within the pseudo band gap, infinitely many modes occur with low group velocity and a very high attenuation.

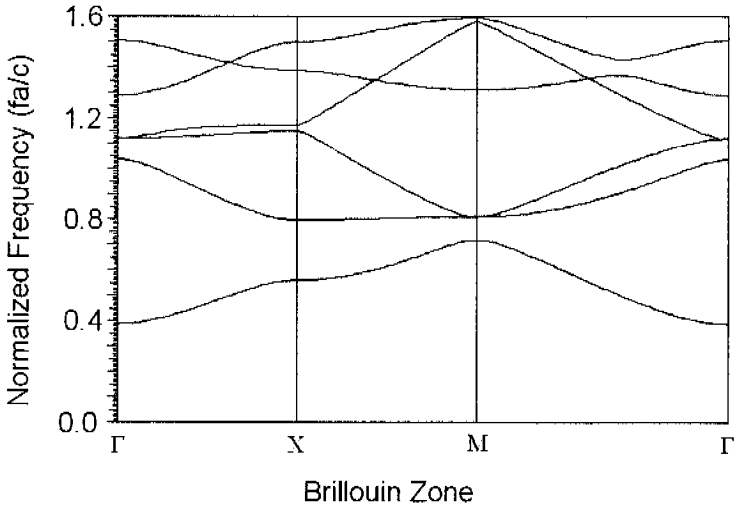

Fig.2.11 Same as in Fig.2.10 for Ez waves and relative permittivity of the rods equal to -20.

2.3.2.2 Ez modes

Computing the band diagrams for fictitious PhCs with negative permittivity inside the rods and positive permittivity outside – for the background material – a fundamental bad gap can be observed that is very similar to the one of PEC PhCs at RF. Fig.2.11 shows the band diagram for a fictitious PhC with rods of relative permittivity equal to -20 in air. As one can see, this PhC has a fundamental band gap for $0 < fa/c < 0.38$ and

a second one around 0.75. Although higher band gaps exist, we focus on the fundamental one in the following, because it is most attractive for practical reasons. Note also that the band diagram shown in Fig.2.11 is very similar to the one shown in Fig.2.8. Since the band diagram of a fictitious PhC with relative permittivity <-20 is not much different from the one shown in Fig.11, it can be concluded that the band diagrams of Ez modes on PhCs with sufficiently negative permittivity are similar to those of PEC PhCs.

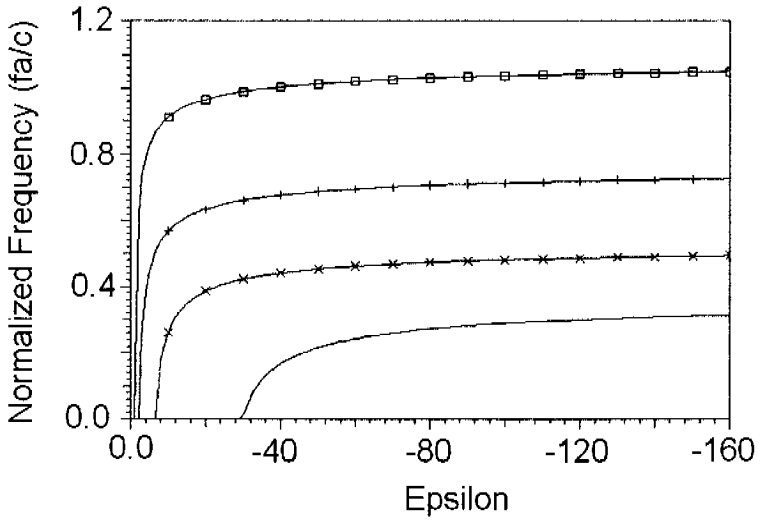

Fig.2.12 Upper limit of the fundamental band gap (normalized frequencies) of Ez waves for a PhC consisting of circular rods with negative permittivity on a square lattice vs. relative permittivity of the rods. Curves for: *r=0.10a* (no marker), *r=0.20a* (x marker), *r=0.30a* (+ marker), *r=0.40a* (square marker).

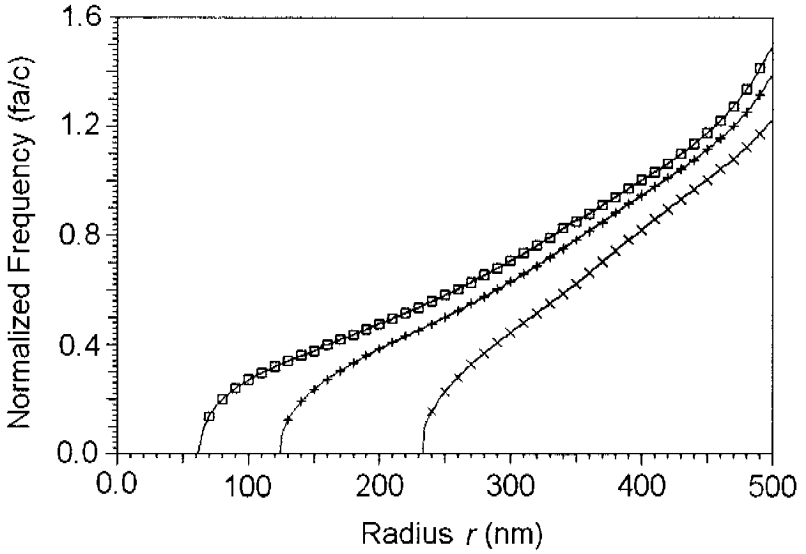

Fig.2.13 Upper limit of the fundamental band gap (normalized frequencies) of Ez waves for a PhC consisting of circular rods with negative permittivity on a square lattice vs. rod radius in nm. Curve with x marker: relative permittivity of the rods: -5; + marker: -20; square marker: -80.

Note that the permittivity is always "sufficiently negative" for metals like silver, copper, gold, etc. below some frequency or above some wavelength. For example, for silver we have a relative permittivity <-20 for wavelengths longer than 662nm. Thus, Ez waves in silver PhCs at red light and in the infrared regime should behave much the same as Ez waves at RF.

2.4 Analysis and design of the fundamental band gap

The fundamental band gap is only observed for Ez waves. It is characterized by its width, i.e., the maximum value of $a'_{max} = f_{max}a_{max}/c = a_{max}/\lambda$. As mentioned before, we now assume that f is a given frequency and that $a' = fa/c = a/\lambda$ is the normalized lattice constant (which is nothing else than the normalized frequency). When we want to design a metallic PhC that has a fundamental band gap with a maximum frequency f_{max}, we proceed as follows: We first compute the corresponding relative permittivity ε_{max}. Then, we compute the band diagram for a fictitious PhC with rods of permittivity ε_{max}. In this diagram, we search for a'_{max}. If it becomes possible to fabricate a PhC with this normalized lattice constant, it will exhibit a band gap for all frequencies provided that $\varepsilon<\varepsilon_{max}$ holds. Since this holds for most metals for all $f<f_{max}$ when $\varepsilon_{max}<-1$ a fundamental band gap is obtained also for the realistic metallic PhC. The maximum normalized lattice constant a'_{max} strongly depends on the rod radius r (or on the filling factor $r^2\pi/a^2$), on the material properties of the rods and of the background material.
As one can see from Figs.2.12-2.14, the fundamental band gap becomes broader for increasing filling factors or rod radii as well as for decreasing (negative) imaginary parts of the rod permittivity ε and for decreasing but positive background permittivity ε_b. Thus, a background with a relative permittivity close to 1 is preferable.

For a PhC with $\varepsilon_{max}<-1$ one obtains a'_{max} from the calculation of the first mode at the Γ point. Thus, it is not necessary to perform time-consuming band diagram computations for obtaining, for example, the dependence of a'_{max} on the rod radius or on the background material. The MMP implementation in MaX-1 allows one to trace a'_{max} as a function of an arbitrary model parameter using the MMP eigenvalue estimation technique [14, 15]. This allows us to efficiently obtain useful information (for example, the diagrams shown in the Figs.2.12, 2.13, 2.15) with short computation times even on a personal computer. This technique was applied for all computations shown in this chapter. It is important to know that this efficient procedure may fail in difficult situations, namely when the traced function varies rapidly and when the tracing step is too big. This explains the "noisy" shape of the curves in Fig.2.13 where the derivative is high, i.e., for low values of fa/c.

2.4.1 Influence of the geometry

Since we consider the most simple case of a metallic PhC consisting of circular rods on a square lattice, there are only two geometric parameters, the lattice constant a and the rod radius r. Fig.2.12 shows the dependence on the normalized lattice constant a'_{max} on r for the fundamental band gap. Obviously, this is a monotonous function that depends on the material properties of the rods and on the background material. For obtaining a broad fundamental band gap, i.e., a high value of a'_{max}, the rod radius r should be as big as possible. From this, one expects that non-circular rods that allow one to obtain bigger filling factors would be even more promising. However, in this initial study, we focus on circular wires.

2.4.2 *Influence of the background material*

The background material essentially depends on the fabrication process of the metallic PhCs. When the metallic rods are grown, for example, with a Focused Ion Beam (FIB), the background material may be air. As an alternative, one might first drill holes in a dielectric and fill the holes with the metal. In this case, the background material would be a dielectric. As illustrated in Fig.2.13, the width of the fundamental band gap is drastically reduced when the permittivity of the background material is increased. Thus, air is the best natural background material. Unfortunately, materials that are frequently used for the fabrication of holey dielectric PhCs (GaAs, InP, etc.) exhibit a high permittivity because a high dielectric contrast is required for dielectric PhCs. Therefore, these materials are not appropriate for metallic PhCs when a broad fundamental band gap is required. In order to clarify this, we consider a PhC consisting of silver wires with radii $r = 0.18a$, where a is the lattice constant. At 662nm, the relative permittivity of silver is around -20 + 0.45i. For longer wavelengths, the real part of the relative permittivity is <-20.

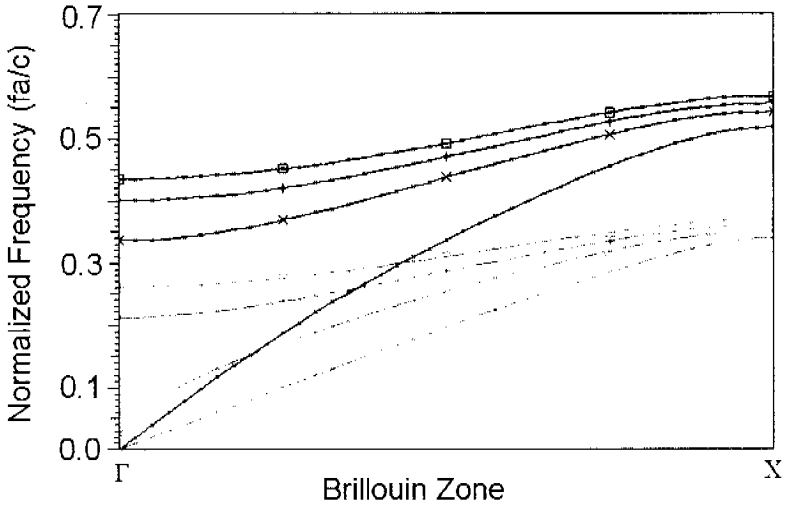

Fig.2.14 Normalized frequencies of the first Ez mode of a PhC consisting of circular rods with negative permittivity on a square lattice between the Γ and X points of the first Brillouin zone. Black color: relative permittivity of the background 1 (air); red color: relative permittivity of the background 2.25 (glass). No markers: relative permittivity of the rods -5; x markers: -20, + markers: -40, square markers: -80; *r=0.18a.*

From Fig.2.14 we can see that we obtain a fundamental band gap for $fa/c<0.33$ when the background material is air, i.e., for a lattice constant smaller than 0.33x662nm = 218nm. The corresponding rod diameter is d = 0.36x218nm = 78nm. It appears to be possible that such a PhC can be fabricated. When the background material has a refraction index n of only 1.5, i.e., a relative permittivity of 2.25, a fundamental band gap is found for $fa/c<0.025$. The lattice constant should then be less than 17nm and the wire diameter less than 6nm. Unfortunately, the fabrication of such a PhC is extremely difficult. Furthermore, the macroscopic material model used for our simulations is no longer accurate because of the small dimensions. For an even higher refraction index of the background material, the fundamental band gap disappears entirely. One then must find metals with a lower (more negative) permittivity or must operate at longer wavelengths (i.e., in the infrareds, where the

permittivity of silver is sufficiently negative) for obtaining a fundamental band gap also for a background material with n>1.5.

2.4.3 *Influence of the material loss*

We have already mentioned that there are different methods for taking material loss into account. The complex eigenvalue search is time-consuming. Furthermore, the interpretation of complex eigenvalues is not easy. Finally, when doing measurements, the frequency is scanned over a real interval and not in the complex plane. For these reasons, we perform simulations of lossy crystals in this chapter using a technique that mimics the measurement situation, i.e. we sweep the frequency and search for the resonance peaks. Finally, we plot the dependence of the resonance peaks on different model parameters as for loss-free PhCs.

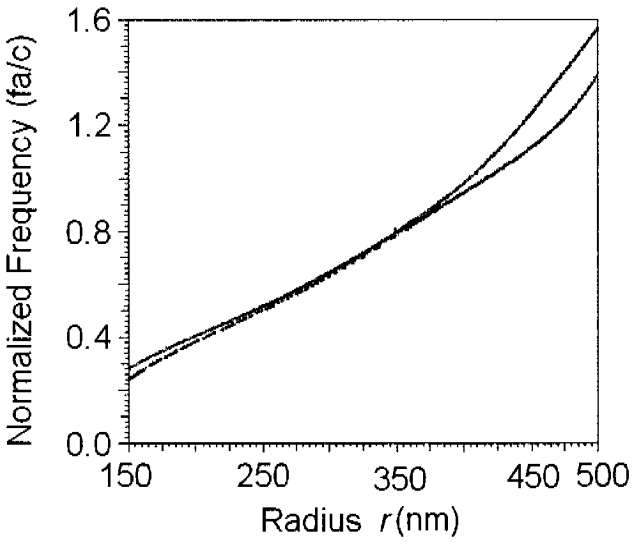

Fig.2.15 Upper limit of the fundamental band gap (normalized frequencies) of Ez waves for a PhC consisting of circular rods with negative permittivity on a square lattice vs. rod radius in nm. Black: relative permittivity of the rods is -20; red: -20+0.5i; blue: -20+10i.

We have already demonstrated that even small imaginary parts of the permittivity, i.e., small amounts of material loss may have a drastic influence on some of the modes. Of course, this makes the value of traditional, loss-free computations questionable. Fortunately, the drastic influence of the material loss was only observed for the flat bands of Hz modes and can be understood from the slow group velocities of these modes. The modes outside the flat band area do not suffer from such strong loss dependence. This also holds for Ez modes, as shown in Fig.2.15 – at least when the rod radii are not too big.

2.5 *Conclusions and Outlook*

We have demonstrated that the Ez waves on metallic photonic crystals at optical frequencies behave very much like the Ez waves at radio frequencies – provided that the real part of the permittivity of the metal is sufficiently negative and provided that the refraction index of the background material is not high, i.e., sufficiently close to 1. In this case a fundamental band gap is obtained without any lower frequency limit. The band diagrams look similar as the diagrams for perfectly conducting wires. This

is surprising because metals lose their conductivity at optical frequencies. Since the width of the fundamental band gap increases with the filling factor, we expect that non-circular wires might be attractive for obtaining wide fundamental band gaps. Since current fabrication technologies are not advanced enough for obtaining, for example, square nano wires, we have postponed a detailed study of the influence of the geometric shape although our software is not restricted to circular wires.

We have studied plasmon resonances of a single metallic wire, of a set of 9 wires, and of metallic PhCs. For cylindrical structures, plasmon resonances only exist for Hz waves. Although the scattering cross section of a single wire is increased for Hz waves (because of the plasmon resonance) as much as when Ez waves are considered, the plasmon resonances do not cause a band gap, i.e., a stop band. Instead of this, one obtains a flat pass band with a bundle of modes with slow group velocity. The modes in the flat pass band are very sensitive regarding material losses. Unfortunately, this spoils the attractive properties (slow group velocity of the modes) of the flat pass band. For well-known metals the losses are so high that these modes are attenuated to such a degree that they cannot observed at all. As a consequence, a "pseudo band gap", i.e. a stop band is obtained instead of the pass band that is obtained from loss-free computations. This extreme inversion of a pass band into a stop band makes clear that there is a high risk to obtain results without any practical relevance when loss-free models of metallic wires are considered. Since most of the work published on metallic PhCs relies on loss-free calculations, there is a strong need for a more careful analysis that accounts for the losses.

References

[1] P. B. Johnson, R. W. Christie, *Phys. Rev. B* **6**, 4370 (1972).

[2] M. J. Weber, *Handbook of Optical Material*, CRC Press, Boston (2003).

[3] J. Kottmann, *Numerical study of plasmon resonant nanowires*, thesis ETH **14247**, Zurich (2001).

[4] E. Yablonovitch, *Phys. Rev. Lett.* **58**, 2059 (1987).

[5] J. B. Pendry and A. MacKinnon, *Phys. Rev. B* **69**, 2772 (1992).

[6] D. R. Smith, S. Schultz and N. Kroll, *Appl. Phys. Lett.* **65**, 645 (1994).

[7] A. L. Pokrovsky, *Phys. Rev. B* **69**, 195108 (2004).

[8] V. G. Veselago, *Soviet Phys. Usp.* **10**, 509 (1968).

[9] D. R. Smith, W. J. Padilla, D.C. Vier, S. C. Nemat-Nasser, and S. Schultz, *Phys. Rev. Lett.* **84**, 4184 (2000).

[10] A. A. Houck, J. B. Brock, and I. L. Chung, *Phys. Rev. Lett.* **90**, 137401 (2003).

[11] D. R. Smith and N. Kroll, *Phys. Rev. Lett.* **85**, 2933 (2000).

[12] G. Shvets, *Phys. Rev. B* **67**, 035109 (2003).

[13] Ch.Hafner, The Generalized Multipole Technique for Computational Electromagnetics, Artech House, Boston (1990).

[14] Ch. Hafner, *Post-modern Electromagnetics*, John Wiley & Sons, Chichester (1999).

[15] Ch. Hafner, MaX-1, *A Visual electromagnetics platform,* John Wiley and Sons, Chichester (1998).

[16] http://alphard.ethz.ch/hafner/MaX/max1.htm (2004).

[17] J. B. Pendry, *Phys. Rev. Lett.* **85**, 3966 (2000).

[18] N. Fang and X. Zhang, *Appl. Phys. Lett.* **82**, No. 2 (2003).

[19] P. F. Loschialpo, D. L. Smith et al., *Phys. Rev. E* **67**, 025602 (2003).

[20] V. Kuzmiak, A. A. Maradudin, and F. Pincemin, *Phys. Rev. B* **50**, 16835 (1994).

[21] N. A. Nicorovici and R. C. McPhedran, *Phys.Rev.E* **52**, 1135 (1995).

[22] E. I. Smirnova, C. Chen, M. A. Shapiro, J. R. Sirigiri, and R. J. Temkin, *Journal of Appl. Physics* **91**, No.3 (2002).

[23] E. Moreno, D. Erni, and Ch. Hafner, *Phys. Rev. B* **65**, 155120 (2002).

[24] K. Sakoda and J. Kawamata, *Opt. Express* **3**, No. 1 (1998).

[25] K. Sakoda, N. Kawai, and T. Ito, *Phy. Rev. B* **64**, 045116 (2001).

3 Ultra-compact metallo-dielectric photonic crystal filters design

In chapter 2, metallic photonic crystals at RF and OF were analyzed, which exhibited many interesting features that can be exploited for engineering. In this chapter, filter characteristics of metallo-dielectric photonic crystal slabs are analyzed using the Multiple Multipole Program. In order to reduce the computation time of frequency characteristics, it is combined with the Model-Based Parameter Estimation (MBPE) technique. This approach takes losses and material dispersion into account and provides highly accurate results at short computation times. Starting from this analysis, different ultra-compact band-pass filters for telecommunication wavelengths are designed. By applying stochastic and deterministic techniques the filter structures are optimized to get the desired characteristics.

3.1 Introduction

Embedding metallic wires in a dielectric background material or coating Dielectric Photonic Crystals (DPhCs) with metals are obvious extensions that are called Metallo-Dielectric Photonic Crystals (MDPhCs) [1, 2]. In this chapter, both pure MPhCs and MDPhCs are considered. For reasons of simplicity, only 2D, i.e. cylindrical structures are studied. This means that the off-plane loss of realistic structures with finite size is not taken into account.

Up to now, most of the papers dealing with metallic photonic crystals describe the dispersive characteristics, i.e., the frequency dependence of the permittivity by a Drude model that is known to be not very accurate, especially near those frequencies where plasmon effects occur [3]. It is important to note that the Drude model itself takes material losses into account, i.e., it describes the permittivity by a complex, frequency-dependent number. Simplifications of the dispersive characteristics are essential for time domain codes such as those based on FDTD method currently most often used for the simulation of 3D DPhC structures. Since losses make the FDTD scheme more complicated and increase the required memory, losses are often entirely neglected. Unfortunately, this simplification has a profound impact on the simulation accuracy of MPhCs that are based on plasmon effects: When losses are accounted for, the flat bands disappear as shown in the previous chapter. Sample computations of various MPhC filters with Microwave Studio® [4] - a prominent commercial Finite Integral Time Domain (FITD) solver that includes lossy Drude models - show that even elaborated implementations of material models lead to substantial inaccuracies that considerably disturb the optimization process. Since numerical optimizations are highly valuable for the design of MPhC and MDPhC filters, MMP [5] was used in the following investigation. Furthermore, measured data was used to make the calculation more realistic [6].

DPhC filters have already been studied by several groups [7, 8, 9]. Often, the DPhC structure plays the role of a Bragg mirror, i.e., a nano-cavity is embedded between two DPhC mirrors [8]. For this purpose, the PhC structure operates within the Photonic Band Gap (PBG). DPhC filters may be embedded in conventional optical waveguides [10] or in PhC waveguides [11]. For the analysis of the DPhC filter characteristics one usually considers a simple DPhC slab that exhibits periodic symmetry in x direction and consists of a few layers of rods or holes in y direction [7,

8, 9]. In this chapter, we consider such PhC slabs made of metallic rods in free space or embedded in a dielectric.

Obviously, any DPhC structure can be replaced by appropriate MPhC or MDPhC structures. When doing this, one should be aware of the losses that are substantial in metals and reduce the quality of the band gap. In order to keep the losses as small as possible, it is important to reduce the number of PhC layers as much as possible, which is also highly desirable from the miniaturization point of view. The densification of filter structures causes strong interactions of the filter parts. This increases the complexity of the filter design. For the design of ultra-compact filters, standard design rules fail and one is forced to take advantage of numerical optimizers as demonstrated in the following.

Essentially, there are two different categories of numerical optimizers: deterministic and probabilistic or stochastic [12, 13]. The former are much faster when started sufficiently close to the optimum but they usually are trapped near local optima and are not able to find the global optimum in complicated cases as in the PhC filter design. For defining a good start point for an MPhC filter that can be improved with a deterministic optimizer, experience is needed. It may be obtained from extensive numerical simulations of relatively simple structures as outlined in the following sections.

In order to reduce the computation time as much as possible, the Model-Based Parameter Estimation (MBPE) was used [14-16]. It is important to note that MBPE is originally designed for linear filters. Therefore, it optimally works for PhC filters made of dispersion-free materials such as DPhC filters. When applied to MPhC structures, the pronounced frequency-dependence of the complex permittivity degrades the MBPE performance and requires the implementation of auxiliary routines that automatically subdivide the frequency range into reasonably small pieces. However, for the filter design at telecom wavelengths – where the frequency characteristics of low-loss metals are relatively smooth – no substantial problems with MBPE are encountered. The MMP-MBPE computation of the frequency dependence of an MPhC filter with 1000 frequency points and an accuracy better than 1% requires on the order of one minute on a personal computer [22]. For the same computations, Microwave Studio® takes at least 20 times more computation time, much more memory, and the results are considerably less accurate because it uses a Drude model and because it discretizes the space. However, the MMP-MBPE computation time is sufficiently short even for stochastic optimizations with not very efficient algorithms when there are no good start values for the initial filter design available.

3.2 Model-Based Parameter Estimation

Most EM phenomena require essentially a continuous representation of the system response over a specific frequency range. The computation of the observables (S parameters, transmission and reflection coefficients, field strengths in certain points of space, etc.) with sufficient resolution can be expensive especially when sharp resonances are present. MBPE allows us to obtain the system response over the entire frequency range by using a relatively small number of frequency samples [14, 15, 16]. The main concept of MBPE is the following. In the frequency domain, the response of a linear system may be optimally represented by Cauchy's method, i.e.,

$$F(s) = \frac{N(s)}{D(s)} + Error(s) = \frac{\sum_{i=0}^{n} N_i s^i}{\sum_{i=0}^{d} D_i s^i} + Error(s) \tag{1}$$

where F is the response of the system and s is the complex frequency that also may be limited to the radian frequency $i\omega$. The error of this approximation depends on the maximum orders n and d of the power series expansions in the nominator N and denominator D as well as on the method that determines the parameters N_i and D_i. A simple technique to compute the parameters is to multiply (1) by D and rewrite (1) in a set of m frequency points s_k:

$$F(s_k)\sum_{i=0}^{d} D_i s_k^i - \sum_{i=0}^{n} N_i s_k^i = Error(s_k)\sum_{i=0}^{d} D_i s_k^i = E_k, k \tag{2}$$

where E is an unknown error vector. When F is known in $m \geq n+d+1$ points s_k, (2) is a linear system of m equations. One then can evaluate the parameters D_i and N_i in such a way that the square norm of the error vector is minimized. Before this is done, one should note that not all parameters are independent because nominator and denominator in (1) may be scaled with an arbitrary factor. For this reason, one of the parameters may be set equal to 1. It is reasonable to set $D_d = 1$. One then obtained:

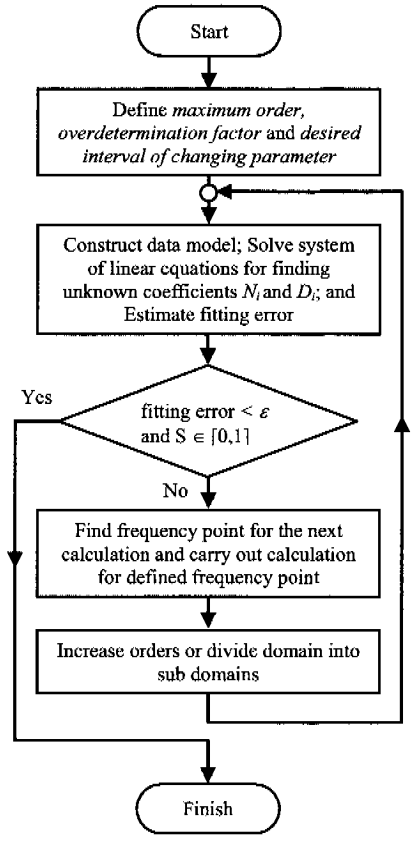

Fig.3.1: MBPE procedure for PhC filters analysis

$$F(s_k)\sum_{i=0}^{d-1} D_i s_k^i - \sum_{i=0}^{n} N_i s_k^i = -F(s_k)s_k^d + E_k = R_k + E_k, k = 1,...m \tag{3}$$

where R is a known, right-hand-side vector. Note that (3) can be solved in such a way that the error vector E is zero when $m = m_0 = n+d+1$, because one then obtains a square matrix system. This does not imply that $Error(s)$ becomes zero as well. Especially when the sample values $F(s_k)$ are only approximately known – which is always the case in practice – it is more reasonable to work with an overdetermined system of equations with $m > m_0$. Reasonable overdetermination implicitly provides smoothing of "noise" and "ripples" caused by inaccurate Maxwell solvers. When highly accurate codes such as the MMP [19, 20, 21] and the Method of Auxiliary Sources (MAS) [17, 18] are used, very weak overdetermination (with overdetermination factors m/m_0 around 1.1) is sufficient. This obviously reduces the number of frequency points required. Since the time-consuming part of the MBPE is the computation of the sample values by the Maxwell solver, weak overdetermination saves computation time.

The most difficult problem is to determine the required maximum orders n and d of the power series of the nominator and denominator. Both depend very much on the size of the frequency range of interest, the desired accuracy, and the complexity of the system. Since metals within MPhCs and MDPhCs are strongly dispersive at optical frequencies, MPhC and MDPhC filters are non-linear and may be linearized only over a sufficiently short frequency interval. Therefore, it is reasonable to limit the maximum orders n and d by a value of typically not higher than 10 and to subdivide the frequency interval into two or more parts when the MBPE approximation is not accurate enough.

The block scheme of the MBPE procedure used for the PhC filter analysis is presented in Fig.3.1. The MBPE procedure is adaptive and starts with small orders, i.e., n and d values and with a small number of test points according to the overdetermination factor specified by the user. It then increases the order by 1 and compares the resulting MBPE approximations. When the differences between the two approximations are below a user-defined error bound over the entire frequency range and when all S parameters are within the range 0...1, the MBPE approximation is good enough and the procedure stops. Otherwise, it inserts new test points within the frequency range as follows: If an S parameter is out of the range, it inserts the new test point at the frequency where the biggest distance from the range 0...1 is encountered. Otherwise, it searches for the maximum difference between the current and previous MBPE approximation and sets the new test point at the corresponding frequency. The evaluation of the filter response, e.g., the S parameters, in the new test point is then performed by the field solver, for example, MMP or MAS. When the number of test points is high enough, the MBPE order is increased – provided that the user-defined maximum order is not yet reached. As soon as the maximum order is reached, the frequency interval is split into two intervals with half the length of the original interval and a separate MBPE approximation is started for each interval. This procedure is recursively continued if required.

One is often interested in the frequency dependence of several characteristic values, for example, the S parameters. Usually, the field solver can simultaneously evaluate all parameters with almost the same numerical costs as for a single parameter. Therefore, it is reasonable to implement an MBPE procedure that simultaneously evaluates the frequency response of several observables, for example, all S parameters. All that needs to be done for such a multi-parameter MBPE is to define the maximum fitting error over all model parameters – typically the sum of the square errors of all model parameters. Beside this, the procedure outlined in Fig.3.1 remains the same.

3.3 Metallic photonic crystal analysis

As for DPhCs the band diagrams of MPhCs and of MDPhCs provide a quick overview over the most important properties. As for DPhCs, the band diagrams of MPhCs and MDPhCs are usually normalized. Fig.3.2(a) shows the normalized band diagrams for a MPhC consisting of circular silver rods with different radii on a square lattice with lattice constant a. It is very important to note that such band diagrams are only valid for a single lattice constant a because of the frequency dependence of the material properties (permittivity). Furthermore, it should be mentioned that the standard band diagrams do not contain any information on the material losses.

The goal is to design a band pass filter with low transmission loss at the telecom wavelength 1.55μm. By properly selecting the lattice constant a and the wire radius r, one can easily design the MPhC in such a way that 1.55μm is either in the

fundamental band gap that extends from zero frequency to some cutoff frequency for the first mode or in one of the higher band gaps. The green line in Fig.3.2 represents a wavelength of 1.55μm which is inside the fundamental band gap for the lattice constant a = 820nm when the radius of the silver wires is large enough. One therefore could use such an MPhC as a Bragg mirror and embed an appropriate nano cavity between two identical MPhC pieces. Of course, these MPhC pieces must be of finite size, i.e., MPhC slabs with a finite number of layers. For a finite MPhC slab one can easily compute the frequency dependence of the transmission coefficient T for an incident plane wave. As one can see from Fig.3.2(b), the band diagram of the perfect MPhC and the frequency dependence of T are strongly correlated when the number of layers is large enough.

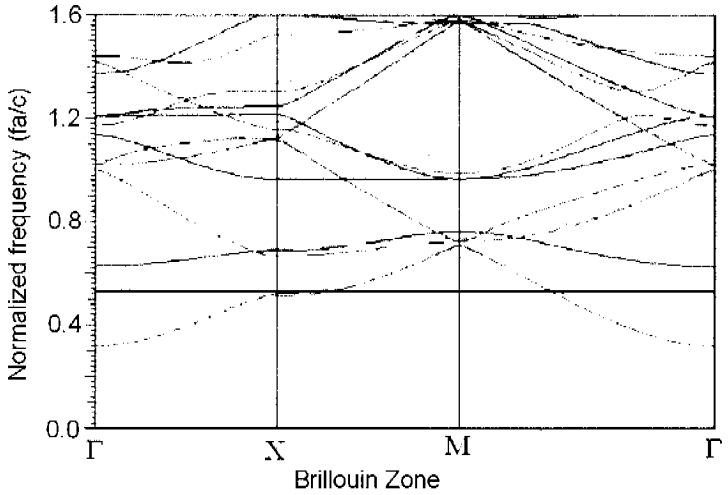

(a)

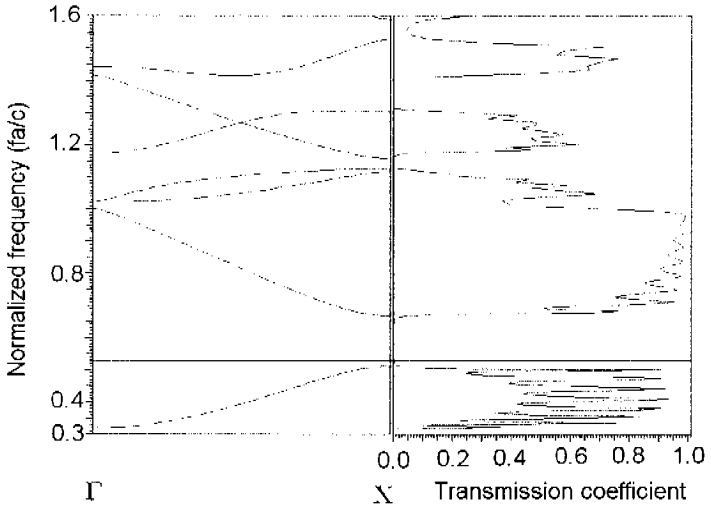

(b)

Fig.3.2 (a) Band diagram for silver photonic crystals consisting of circular rods with radius r on a square lattice with lattice constant a = 820nm, *Ez*-polarization (electric field parallel to the silver rods); black: r/a = 0.2683; red: r/a = 0.1114; blue: r/a = 0.089. Green line: Wavelength 1.55μm. (b) Part of the band diagram of an infinite MPhC (left) and frequency dependence of the transmission coefficient of a 9 layer MPhC slab (right) for silver wires on a square lattice with a = 820nm, r/a = 0.0894, *Ez*-polarization. Green line: Wavelength 1.55μm.

In those areas of the frequency spectrum where a mode between the Γ and X points is present, one observes a useful behavior of $T(\omega)$, similar to a higher order bandpass filter. The number of peaks with high transmission increases with the number of MPhC layers. In order to obtain a band pass filter one therefore might design a single MPhC in such a way that the band pass area is simply the frequency range of the first mode between the Γ and X points, i.e., one essentially designs a PhC operating between two band gaps. For obtaining a band pass around 1.55μm wavelength, i.e., 193.55THz, one could reduce the radii of the silver rods or reduce the lattice constant. However, from Fig.3.2(b) it is seen that such a band pass filter shows not a very good performance.

In order to improve the filter performance, filters with different characteristics can be combined. For example, by cascading two filters with different pass bands that overlap only within a short frequency range a narrow pass band is obtained. However, when two MPhC slabs are cascaded, these slabs strongly interact with each other and this substantially modifies the individual filter characteristics. This makes the design of such filters very demanding and numerical optimizers become highly desirable.

3.4 Deterministic filter optimization

Instead of cascading different PhC slabs and finding ways to reduce undesired interactions between the slabs, a PhC filter is designed that consists of N strongly interacting 1-layer slabs. This may also be considered as a single N-layer slab with arbitrary radii to be optimized. For reasons of simplicity and in order to keep the computation time short, only $N = 5$ is considered in the following. Increasing the number of layers is similar to increasing the filter order in classical filter design: With a relatively low order, no high-performance filter can be achieved. At first sight, one might therefore conclude that $N = 5$ is far from being enough for obtaining a reasonable band pass filter with desired center frequency and band width. It will be demonstrated below that the filters with $N = 5$ layers can be optimized in such a way that 1) the desired center frequency is obtained precisely, 2) the insertion loss is reasonably small, 3) and that the bandwidth may be modified within some limits.

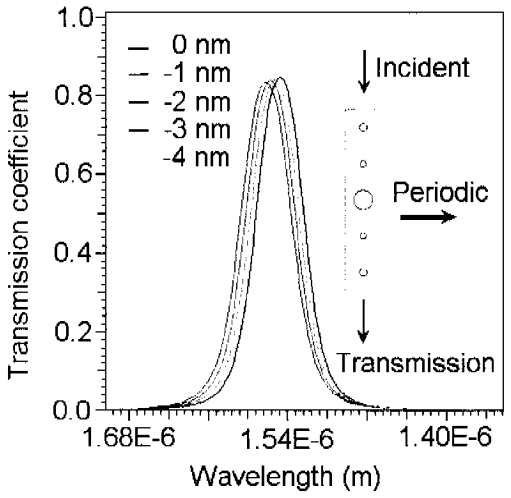

(a)

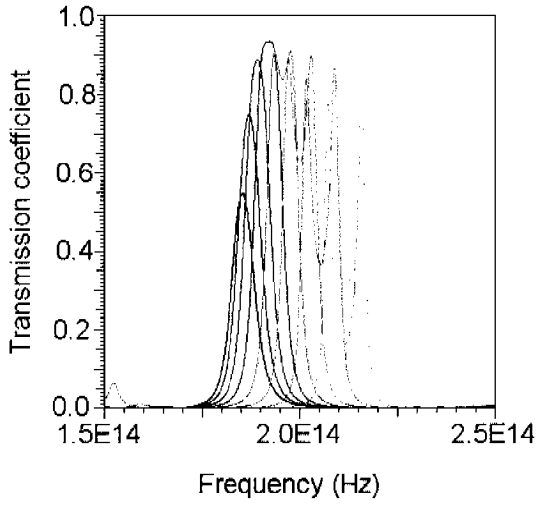

(b)

Fig.3.3 Transmission characteristics for MPhC band pass filters, operating at 1.55μm; 5 layers of silver rods; lattice constant a=820nm. (a): version optimized for maximum transmission at 1.55μm; radii of the wires: r_1=r_5=91nm, r_2=r_4=73nm, r_3=220nm. The colored curves show the transmission response when all radii are simultaneously decreased by 1, 2, 3, 4nm, respectively. (b): Radii r_1=r_5=89.8nm, r_3=207.44nm, r_2=r_4 tuned from 20nm (dark color) to 200nm (bright color).

Note that one may not only optimize the radii of the N PhC layers but also the locations of the rods or even the shape and material properties of the rods. This increases the search space and offers the chance of finding better or more compact filters at the price of longer computation time. However, for a first exploratory study it is reasonable to start with low numbers of model parameters to be optimized. Therefore, we assume that the rods are not displaced and have circular cross sections, i.e., we only optimize $N = 5$ radii r_i. Assuming symmetry of the structure, i.e., $r_4 = r_2$ and $r_5 = r_1$, further simplifies the optimization, that is the optimization is carried out in the 3-dimensional parameter space r_i, where $i = 1, 2, 3$. Starting with a reasonable initial guess – obtained from the analysis of various 5 layer structures – the optimization procedure presented in [14] finds the filter response shown in Fig.3.2. This Figure also illustrates the dependence of the filter response on the radii of the silver rods. When the radii of all rods are simultaneously increased or decreased, one essentially observes a shift of the center frequency with a slight change of insertion loss and width of the pass band. When only a symmetric pair of rod radii is modified, one observes a much more drastic change of the filter characteristic. For small radii of the four outer rods, no pass-band ripple is observed. The center frequency shifts towards higher frequencies with increasing radii and the bandwidth is increased. At some size of the radii, substantial pass-band ripple is observed. The dependence of the filter characteristic on the center rod is similar but moves in opposite direction: For an increasing radius of the center rod, the center frequency shifts toward lower frequencies. This allows one to tune both the center frequency and the band width. Of course, this optimization has some limitations. For filters with wider bandwidths and low pass band ripple as well as for filters with narrower band widths and low insertion loss, the optimization space with N=3 (5 symmetric circular rods on a equidistant lattice) is too small. Note that shifting the center frequency is relatively easy within

the frequency range considered in Fig.3.3. For stronger frequency shifts, not only the rod radii but also the lattice constant must be modified – which is also not difficult.

3.5 Stochastic optimization

A good initial guess is essential for the deterministic optimization. When this is not available, the optimizer may converge toward a local optimum that is far away from the desired goal. The Fig.3.4(a) shows one of the filter responses for randomly defined radii. As one can see, the variety of responses is huge and only a small fraction of possible designs is in the vicinity of the desired filter response. Therefore, it is a time-consuming task for a stochastic optimizer to find a reasonable solution. However, as soon as the stochastic optimization has found a roughly acceptable design, it is reasonable to pass it to a deterministic optimizer that rapidly converges as shown in Fig.3.4(b).

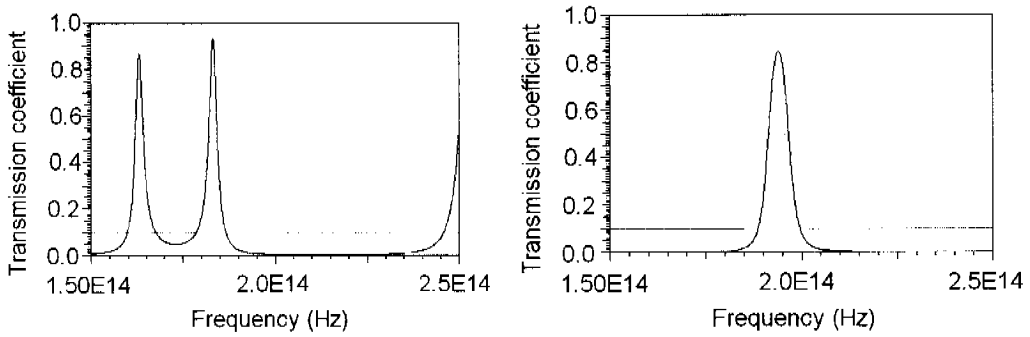

Fig.3.4 Transmission characteristics for various MPhC structures with 5 layers of silver rods. (a) One of the filter responses for random search; (b) One of the filter responses for deterministic search, starting at a reasonable initial guess. The desired filter characteristic is indicated by the red and green lines: For the frequency ranges marked red/green line, maximum/minimum transmission is desired.

3.6 Dielectric background MDPhC filters

The design of MDPhC filters, i.e., of metallic wires embedded in a dielectric background material can be carried out exactly as for the MPhC case. First, an initial guess is found either from experience, trial and error, or stochastic search. Deterministic optimization then quickly leads to the desired optimum – provided that such an optimum exists, which essentially means that the number of model parameters N and the search space are big enough. The dielectric background material essentially allows one to reduce the size of the filter structure. At the same time, the contrast of the permittivity $|\varepsilon_{metal}|/|\varepsilon_{background}|$ is reduced which in turn can deteriorate the filter performance.

Figure 3.5 shows the optimization result for two MDPhC filters consisting of 5 silver rods in dielectrics with slightly different permittivities. The lattice constant was reduced to *500nm* because the wavelength in glass is shorter than in free space. Thus, the size of this filter is shorter than the MPhC filter considered before. One can see that the width of the pass band is increased. This has two reasons: First, it is more difficult to obtain narrow band pass filters when the contrast of the permittivity is reduced as mentioned above. Second, the fitness definition of the optimization

procedure affects not only the center frequency but also the bandwidth. Here, the fitness definition widens the bandwidth, i.e., the goal of the optimization was not to find a minimum bandwidth solution. Note that such wide-band solutions are difficult to obtain with the concept of a cavity embedded between two PhC layers acting as mirrors.

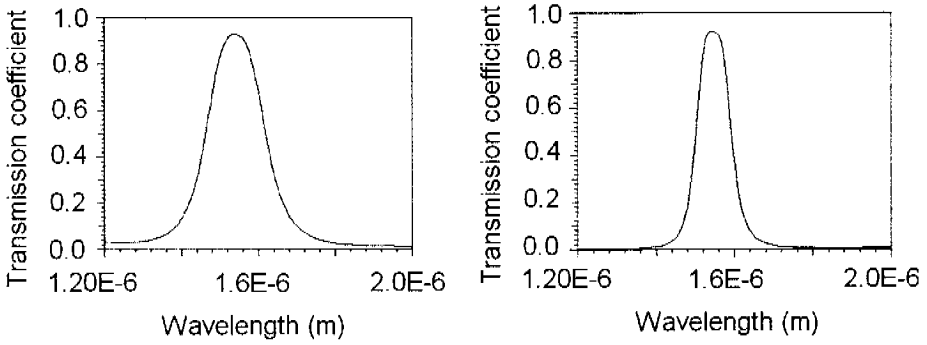

Fig.3.5 Transmission characteristics optimization of two MDPhC structures with 5 layers of silver rods, lattice constant a = 500nm. (a) Relative permittivity of the background material ε_B = 2.0, r_1 = 40nm, r_2 = 20nm, r_3 = 90nm; (b) ε_B = 2.5, r_1 = 40nm, r_2 = 64nm, r_3 = 125.6nm.

3.7 Summary and conclusion

Metallic and metallo-dielectric photonic crystal slabs have been analyzed using MMP solver that can easily account for material losses and dispersion. In order to speed up the computation, MMP has been combined with MBPE that was originally designed for the efficient analysis of linear microwave filters. Ultra-compact band pass filters with a total length of 4100nm for the MPhC case (without background material) and 2500nm for the MDPhC case (with glass as background material) have been designed. In the design process both experience and stochastic search algorithms were used for finding an initial model that was then optimized with efficient deterministic optimization procedures. It has been demonstrated that the center frequency of the filter can be shifted to any desired frequency by optimizing the wire radii, provided that a reasonable lattice constant is used. Furthermore, the bandwidth may be tuned within some limits – that depend on the number of PhC layers. Finally, the insertion loss and pass-band ripple can be kept reasonably small.

References

[1] Ch. Hafner, Cui Xudong, R. Vahldiek, "Metallic Photonic Crystals at Optical Frequency," *J. Comp. Theor. Nanoscience* **2**, No.2, pp. 240-250 (2005).

[2] Takayama, and M. Cada, "Two-dimensional hexagonal metallic photonic crystals embedded in anodic porous alumina for optical wavelengths," *Applied Physics Letters* **85**, No. 8, pp.1311-1313 (2004).

[3] Ch. Hafner, "Drude Model Replacement by Symbolic Regression," *J. Comp. Theor. Nanoscience* **2**, 88-98 (2005).

[4] http://www.cst.de/Content/Products/MWS/Overview.aspx.

[5] http://alphard.ethz.ch/hafner/MaX/max1.htm.

[6] P. B. John, R. W. Christie, *Phys. Rev. B* **6**, 4370 (1972).

[7] S. Jugessur, P. Pottier and R. M. De La Rue, "Engineering the filter response of photonic crystal microcavity filters," *Opt. Express* **12**, 1304-1312 (2004),

[8] W. Nakagawa, Pang-Chen Sun, Chyong-Hua Chen, and Y. Fainman, "Wide-field-of –view narrow-band spectral filters based on photonic crystal nanocavities," *Opt. Lett.* **27**, 191-193 (2002).

[9] C. Ciminelli, F. Peluso, M. N. Armenise, "Modeling and Design of Two-Dimensional Guided-Wave photonic band-gap devices," *Journal of Light. Tech.* **23**, 886-901 (2005).

[10] R. Costa, A. Melloni, M. Martinelli, "Bandpass Resonant filters in Photonic-Crystal Waveguides", *IEEE Photo. Tech. Lett.* **15**, 401-403 (2003).

[11] J. Smajic, Ch. Hafner, and D. Erni, "On the design of photonic crystal multiplexers," *Opt. Express* **11**, 566-571 (2003),

[12] Ch. Hafner, J. Smajic, D. Erni, "Simulation and Optimization of Composite Doped Metamaterials," Chapter in M. Riedt, et al "Handbook of Theoretical and Computational Nanotechnology," *American Scientific Publishers* (2005).

[13] J. Smajic, Ch. Hafner, D. Erni, "Optimiztion of photonic crystal structures," *J. Opt. Soc. Am. A* **21**, 2223-2232 (2004).

[14] E. K. Miller, "Model-Based Parameter Estimation in Electromagnetics: Part I. Background and Theoretical Development," *IEEE Antennas and Propagation Magazine* **40**, No. 1, February (1998).

[15] E. K. Miller, "Model-Based Parameter Estimation in Electromagnetics: Part II. Applications to EM Observables," *IEEE Antennas and Propagation Magazine* **40**, No. 2, April (1998).

[16] E. K. Miller, "Model-Based Parameter Estimation in Electromagnetics: Part III. Applications to EM Integral Equations," *IEEE Antennas and Propagation Magazine* **40**, No. 3 (1998).

[17] D. Karkashadze and R. Zaridze, "The Method of Auxiliary Sources in Applied Electrodynamics," *Latsis Symposium on Computational Electromagnetics, Zurich*, Sept. (1995).

[18] R. Zaridze, G. Bit-Babik, K. Tavzarashvili, N. Uzunoglu, D. Economou. "Wave Field Singularity Aspects Large-Size Scatterers and Inverse Problems." *IEEE Trans. on Antennas and Propagation* **50**, No. 1 (2002).

[19] E. Moreno, D. Erni, Ch.Hafner, R. Vahldieck, "Multiple multipole method with automatic multipole setting applied to the simulation of surface plasmons in metallic nanostructures" *J. Opt. Soc. Am. A.* **19**, No. 1 (2002).

[20] Ch. Hafner "Multipole multipole program computation of periodic structures" *J. Opt. Soc. Am. A* **12**, No. 5 (1995).

[21] Ch. Hafner, "Post-modern Electromagnetics," John Wiley & Sons, Chichester, (1999).

[22] Kakhaber Tavazrashivli, Christian Hafner, Cui Xudong, Ruediger Vahldieck, "Model based parameter estimation for metallic photonic crystal filters design," *ACES Journal*, 2006, Nov..

4 Design of filters based on photonic crystal slabs

In chapter 3, ultra-compact MDPhC filters were designed with MMP + MBPE. Simple stochastic and deterministic optimizers were linked with these solvers and applied to obtain the desired filter characteristics. Since a good initial guess was obtained from experience or by chance via simple stochastic optimizers, the design procedures shown in chapter 3 are not general. Furthermore, the structures with periodicity in one direction as considered in chapter 3, becomes relatively big for practical purposes, i.e. for integrated circuits application. In this chapter, a more general routine is presented, again based on MMP simulation. This includes fitness definitions and more powerful stochastic and deterministic optimizers, namely genetic algorithms, evolutionary strategies and gradient based algorithms. Two methods a) using conducting walls instead of periodic boundary conditions of the PhC slab and b) embedding a PhC filter in a conventional waveguide structure are investigated to demonstrate the possibilities of realizing slab based structures in practice.

4.1 Introduction

By introducing point or line defects in a perfect PhC structure, the light can be localized or guided at the defect region with the frequency in the gap. These two types of defects were utilized for optical filters design in wavelength-multiplexed communication systems [1-3]. A typical structures is the PhC slab based structure shown in chapter 3 [1]. This structure has infinite size in the direction perpendicular to the wave propagation. Therefore, it is impractical for engineering fabrication because many periods are needed for obtaining a good approximation. This makes the structure size very big and inappropriate for integration in optical circuits.

At microwave frequencies, a PhC filter can be embedded inside a rectangular waveguide [5]. The waveguide walls act as almost perfect mirrors that may be replaced by periodic boundary conditions for the PhC slab case when the wave vector has only negligible components along the periodic direction. At optical frequencies, PEC walls are not available. Instead, highly reflective materials like noble metals can be used as substitutions for PECs, although metals at optical frequencies are more absorptive and dispersive than in the microwave region. Another approach is to embed a PhC filter in a photonic crystal waveguide [2] or in a ridge waveguide [3]. In this chapter, the focus is on how to realize a PhC slab based filter centered at 1.55μm for telecommunication applications.

To obtain high quality, compact-size, and controllable filter characteristics, conventional design rules are impractical because of strong interaction between these small elements leading to unexpected results. Therefore, optimization methods must be used. The methods presented in the following are utilized to design the structures in this chapter.

4.2 Numerical optimization

As there is a shortage of design rules for PhC filters, one often resorts to the inverse design approach especially when new structures with new functionality can not be obtained via physical intuition. The best way for finding compact filter structures is to combine accurate field solvers with appropriate numerical optimizers, as shown in the following.

4.2.1 Stochastic Optimizers

The main advantage of stochastic optimizers such as Genetic Algorithms (GAs) [7, 8] and Evolutionary Strategies (ESs) [8] is that such optimizers are not trapped in local optima and need not to be started with a sufficiently good initial guess of the solution. This is advantageous for optimization. Although GAs are currently widely used for the optimization in high-dimensional real-valued parameter spaces, these algorithms are not really efficient when difficult engineering problems are solved, where the numerical evaluation of a single model is time-consuming. In such cases one would like to find maybe not the global optimum but a sufficiently good local optimum with a very small number of model evaluations of order 100 or 1000. Since the population size of standard GAs is of the same order, it is evident that such optimizers are not much better than random search, which is certainly not good enough. Therefore, one either must use micro-GAs – with a typical population of only 5 individuals – or ESs with small populations, for example, (1+6) ESs or (1,6) ESs. For difficult cases that require hundreds of model evaluations, the population size of the ESs should be increased, whereas the performance of micro-GAs usually is not improved when its population size is increased. Beside the population size, GAs and ESs have several additional parameters that influence their performance. The optimization of these parameters is extremely time-consuming and often poses severe problems for the user. To overcome these problems, we first designed simplified test examples that have a behavior similar to that of the PhC filters. These test examples were then used to find optimal tuning of the GAs and ESs [9]. Since the ESs outperformed the GAs and micro-GAs (as well as other algorithms based on random search, particle swarm optimization, simulated annealing, and downhill simplex with random restart), ESs algorithms were used for the results presented in the following.

4.2.2 Deterministic Optimizers

The fitness function near a local optimum is usually smooth – provided that the field solver used for the fitness evaluation is accurate and does not cause any discretization noise. In smooth areas of the fitness landscape, deterministic optimizers perform much better than stochastic optimizers. Therefore, it is reasonable to stop stochastic optimization when a more or less reasonable structure is found, and pass the fine tuning of the structure to a deterministic optimizer.

Fast deterministic optimizers usually require gradient information that may be derived analytically only when the mathematical definition of the fitness function of all model parameters is simple enough. When the fitness function is evaluated by a field solver, the gradient information may be approximated, for example, by finite differences. In high-dimensional parameter spaces, the evaluation of gradient information is very time-consuming. Therefore, standard gradient optimizers must be replaced by procedures that work with a few gradient approximations [6].

4.2.3 Fitness definitions

For the design of arbitrary PhC structures with any kind of filter characteristics one first defines the goal of the optimization by defining a fitness function as illustrated in Fig.4.1 for a band pass filter. Note that the definition of the fitness function is not unique. Often one defines several barriers for either low or high transmission. For each barrier area one then evaluates the error of the transmission function $T(f)$. Then, the fitness may be defined as

$$Fit(p_1, p_2, \ldots, p_M) = 1 / \sum_{n=1}^{N_b} E_n \tag{2}$$

where N_b is the number of barriers and E_n the error over the area of the n-th barrier. It is usually reasonable to use weighted error sums with weights w_n when one of the barriers spans only a small frequency range – i.e. in the design of narrow band filters. In that case, one can define each weight as the inverse of the frequency span of the respective barrier. Furthermore, one can introduce some function F of the error terms instead of simply defining the fitness according to (2):

$$Fit(p_1, p_2, \ldots, p_M) = 1 / \sum_{n=1}^{N_b} \left[w_n \int_{barrier_n} F(e_n(f)) \mathrm{d}f \right] \tag{3}$$

where $e_n(f)$ is the error along barrier n at frequency f. For example, to avoid small areas with high errors, one can integrate over the squares (or even higher order powers) of the errors.

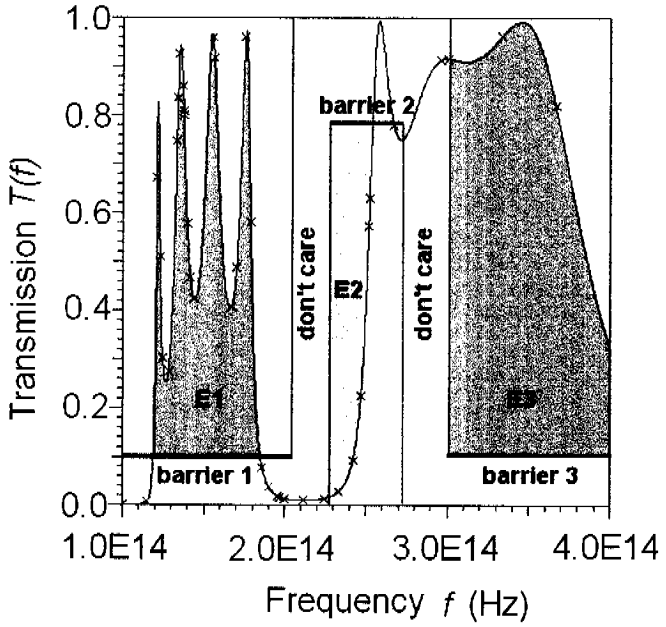

Fig.4.1: Fitness function definition for a band pass filter. In the diagram of the frequency dependence of the transmission coefficient $T(f)$, three barriers are defined. T is requested to be below barrier 1 and 3 but above barrier 2. Between the barrier areas one has two don't care areas where arbitrary values of T are accepted. The gray areas E1, E2, E3 indicate the error integrals in the three barrier areas.

The fitness function depends on the model parameters p_m and often has thousands of different local optima. Most of the local optima deliver impractical solutions. Stochastic optimizers may then be used to select the few promising structures, characterized by high fitness values. This initial optimization step may be extremely time-consuming, in particular for a high number of optimization parameters. Typically, on the order of thousands or even millions of models need to be evaluated. However, to demonstrate the concept, only relatively simple cases with a relatively small number of model parameters are considered in this chapter. Such simple cases may be optimized on a personal computer within a few hours or days.

4.3 *Design and realization of a photonic crystal based filter*

A typical PhC slab based filter structure is shown in Fig.4.2(a), where air columns are drilled in the background dielectric material or dielectric (metallic) rods are arranged in air background. The structure has finite size in one direction (corresponding to wave propagation direction), while the structure is periodic in the perpendicular direction.

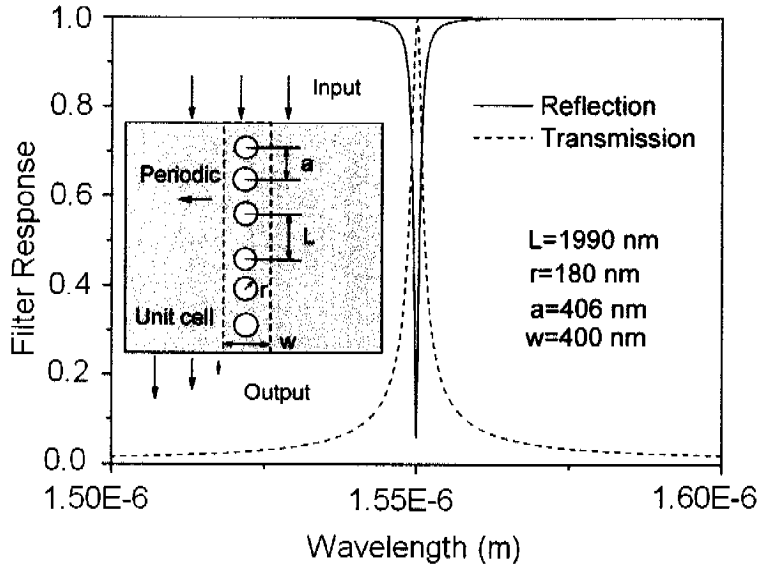

(a)

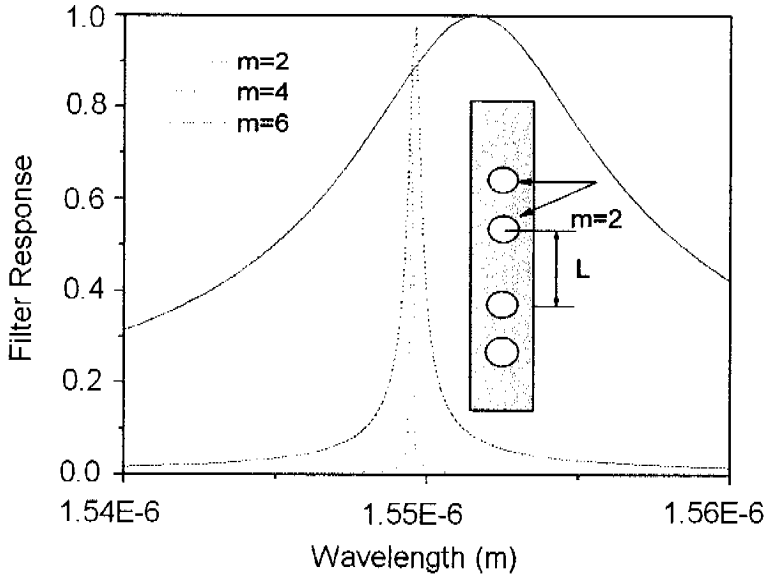

(b)

Fig.4.2: (a) Photonic crystal slab filter and its response using simple design rules, TE polarization (H field is perpendicular to the page plane), dashed rectangular: periodic unit cell in calculation; (b) Filter response with different layers on both sides of cavity as shown in (a).

A simple design rule for this kind of filter structure (only for lossless materials) is: First, a photonic crystal structure is designed with a band gap that covers the interesting frequency range; then defects are introduced to form the cavity (as shown in Fig.4.2(a) inset, by removing one or more columns). Through adjusting the cavity length, the desired filter behavior can be obtained. Actually, as the structure is passive and the material with low loss, it can be scaled down to microwave frequency range while still keeping the same behavior in optical frequencies.
Therefore, one can make use of the structures that have been designed as pass band filters for some frequencies with the help of the structure properties mentioned before. Since the filter operates at optical frequencies, only a PhC structure consisting of air columns drilled in a dielectric medium with $\varepsilon = 10.4753$ on rectangular lattice is considered. For other lattices and other material properties, the same design method might be used. In Fig.4.2(a), the PhC structures on both sides of the cavity have identical parameters (lattice constants and hole radii). This limits the filter response because of a reduced degree of freedom. At the same time, this reduces the search space and therefore the computation time of the optimizer.

From Fig.4.2(b) one can see that with increasing number of PhC layers on the two cavity sides, the quality factor is increased, the bandwidth is reduced, and the center frequency is shifted. Tuning the cavity length L and the PhC parameters doesn't help to improve the filter quality (especially bandwidth and transmission top width) if the central wavelength is fixed to 1.55μm. This is an intrinsic drawback of such a simple configuration. To control the filter characteristics flexibly, more degrees of freedom are needed. For instance, the radii of the air columns may be different, the distances between two adjacent air columns may be unequal, and so on. A simple compromise is to keep the lattice constant a fixed while only the air column radii are optimized. By doing this, the filter response can be controlled more efficiently, i.e., the bandwidth may be tuned and flat top or singly-peaked top transmission may be achieved [1]. Note that - based on the initial structure shown in Fig.4.2(a) - the same method can be employed to get different filter responses according to different fitness definitions.

As the structure shown in Fig.4.2(a) is not practical for engineering applications, alternative approaches using PEC walls or high reflective material (for example, silver) coated on the sides of the unit cell shown in Fig.4.2(a) may be used. The coated structure is shown in Fig.4.3(a). The reason for the partial coating is the high attenuation of metal coated waveguides at optical frequencies. As one can see, the partially PEC walls slightly disturb the filter response: the central wavelength of the filter has a tiny shift and radiation loss increases a little bit because of mode mismatching at transition areas between coated and uncoated waveguide. Since PECs can not be found at optical frequencies, real metal was used to replace the PEC parts (Fig.4.3(b)). Unfortunately, the realistic metal coatings completely spoil the filter response (not shown here). To overcome this difficulty, the entire filter structure needs to be redesigned by the optimization procedure. This allows one to reestablish a band pass filter response although less transmission and wider bandwidth are obtained as shown in Fig.4.3(b). To keep the symmetry of the structure and to save computation time, only 6 PhC layers with 4 optimization parameters (r_1, r_2, r_3, r_4) were considered. To improve the quality of this filter, further optimization with more than 4 parameters (additional air columns, variable distances, tapered shape of the transition from coated to uncoated waveguide) is needed.

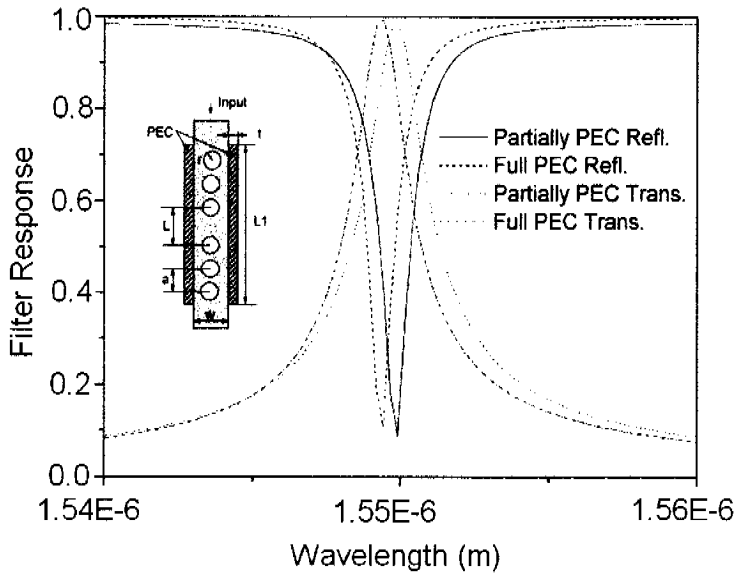

(a)

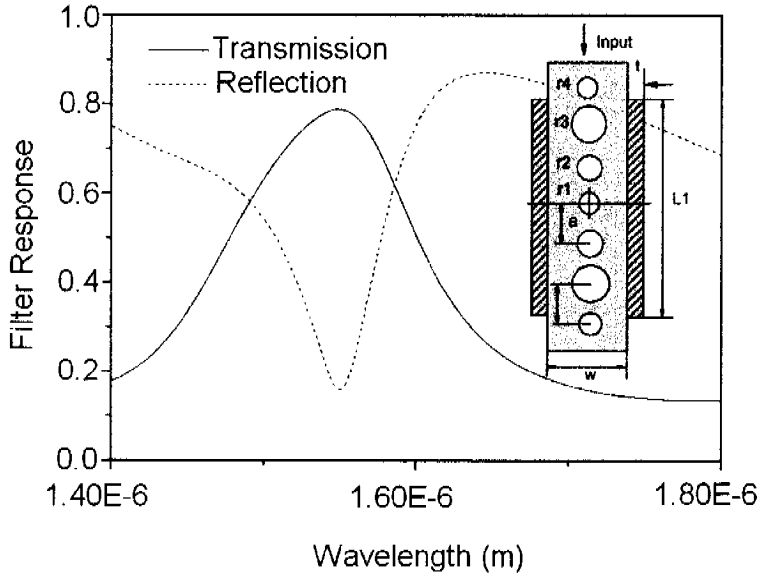

(b)

Fig.4.3: (a) Comparison of filter responses when PECs are fully or partially coated on the unit cell sides in Fig.1a. t = 100nm, L_1 = 4200nm; (b) PEC parts are replaced by silver, the result shown here is partially optimized: r_1 = 75nm, r_2 = 175nm, r_3 = 185nm, r_4 = 85nm, w = 400nm, t = 100nm, L = 1020nm.

4.4 Photonic crystal in a trench waveguide

In optical engineering, PhC slab based filters can be realized by inserting PhC air columns or rods into trench waveguides [3] as shown in Fig.4.4a. For reasons of simplicity, only a 2D model is used here. The 2D effective refractive index is obtained from real 3D structures, for example, a deeply etched InP-based dielectric waveguide, with the help of effective index method approximation. The design procedure shown in the second part may also be applied here for obtaining, for example, a narrow band pass filter. Two identical PhC parts are placed on both cavity sides. To obtain high

quality filter response or to manipulate the filter response in general, mode matching air columns inside or outside the cavity may be introduced [3], which is equivalent to add phase shift regions to the Bragg-mirror type PhC areas (see Fig.4.4(b)). Actually, this is just a special case for the general optimization procedures outlined above.

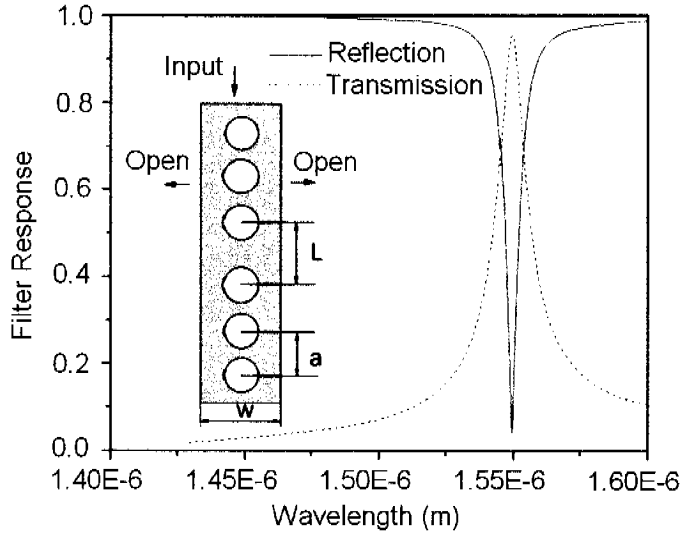

(a)

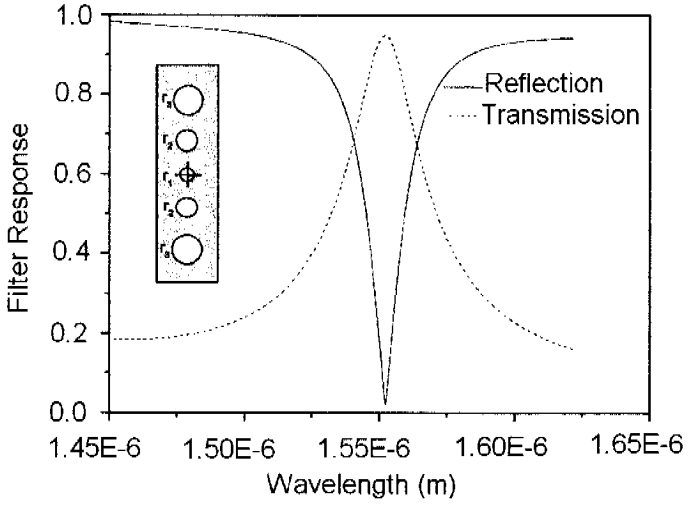

(b)

Fig.4.4 PhC filter in trench waveguide using simple design rule: L = 564nm, a = 400nm, r = 125nm, w = 400nm; (b) Cascaded design structure using our methods (not optimal). a = 480nm, r1 = 88nm, r2 = 130nm, r3 = 160nm, w = 400nm.

4.5 Conclusion

In this chapter, PhC slab based filters are designed and analyzed. To realize PhC slab based filters at optical frequencies, two approaches are proposed, namely, coated and trench waveguide based structures. With the help of the optimization procedures, two designs were successfully realized although further optimization is needed for the real metal coated structures. For the design of filters with extremely high quality or with

complicated filter response, the degree of freedom of the model, i.e., the dimension of the model parameter space may become high. Here, we have focused on extremely compact filters with relatively low-dimensional model parameter spaces for demonstrating the general procedure.

References

[1] Cui xudong, Christian Hafner, Ruediger Vahldieck, "Design of ultra-compact photonic crystal filters," *Opt. Express* **13**, pp.6175-6180, August (2005).

[2] R. Costa, A. Melloni, M. Martinelli, "Bandpass Resonant filters in photonic-crystal waveguides," *IEEE Photo. Tech. Lett.* **15**, pp.401-403(2003).

[3] S. Jugessur, P. Pottier, R. M. De La Rue, "One dimensional periodic photonic crystal microcavity filters with transition mode matching features, embedded in ridge waveguides," *Electron. Lett.* **39**, pp367-368 (2003).

[4] http://alphard.ethz.ch.

[5] L. Mendioroz, R. Gonzalo, C. del Roi, "Design of electromagnetic crystal filters for rectangular waveguides," *Microwave and Opt. Technol. Lett.* **30**, Feb (2001).

[6] J. Smajic, Ch. Hafner, D. Erni, "Optimiztion of photonic crystal structures," *J. Opt. Soc. Am. A* **21**, pp. 2223-2232 (2004).

[7] G. Winter, J. Périaux, M. Galan, P. Cuesta, *Genetic Algorithms in Engineering and Computer Science,* Chichester, John Wiley & Sons, pp. 1-464 (1995).

[8] D. Quagliarella, J. Périaux,C. Poloni, G. Winter, *Genetic algorithms and Evolution Strategies in Engineering and Computer Science*, Chichester, John Wiley & Sons, pp. 1-391 (1998).

[9] Christian Hafner, Cui Xudong, Ruediger Vahldieck, "Stochastic parameter optimizers for optical nanostructures," *International Journal of Microwave and Optical Technology* **1**, vol. 1 (2006).

5 Minimization of radiation near a sharp optical waveguide bend

In this chapter, a sharp trench optical waveguide bend in dual mode operation with small photonic crystal for suppressing radiation has been analyzed. Through optimization, different configurations with low reflection, low radiation, low mode conversion, and therefore high transmission for the dominant mode are obtained. Three different types of bends are analyzed and compared: mirror-based structures, resonator-based structures, and structures with small photonic crystals in the bend area. The local photonic crystal helps not only suppressing radiation but also provides solutions with fewer fabrication tolerance problems. Finally, fabrication and measurement results are given in this chapter to validate the optimization results.

5.1 Introduction

Waveguide bends are key components in integrated optics devices and circuits that have a strong impact on the integration density. In order to avoid power loss due to radiation [1], the radii of conventional waveguides are much bigger than the wavelength which leads to huge size of conventional integrated optics structures. Additionally, substantial mode conversion is observed in the case of multi-mode waveguides. Several propositions were made for reducing the radiation and enhance the transmission [2-6]. Recently, PhC waveguides attracted much attention because sharp bends with zero reflection and radiation are theoretically possible for certain frequencies or even over almost the entire band gap of the PhC [5]. The main problems of integrating such PhC waveguide bends in conventional integrated optics waveguides are the coupling of the shallow-etched rib or deeply-etched trench waveguides with PhC waveguides and the high impact of fabrication imperfections.

For sharp 90° bends in high-index contrast waveguides, several approaches were described [7], namely corner mirrors and waveguide resonators [6] as well as PhCs acting as 45 degree corner mirrors [8]. To the authors' knowledge, single mode operation is assumed throughout and this leads to very narrow, deeply etched trench waveguides (typically 200nm width) that are very hard to fabricate. For wider waveguides, multimode operation poses the additional problem of mode conversion that makes the numerical analysis substantially more difficult. The waveguide bend must be then designed in such a way that not only radiation but also mode conversion is avoided. However, by combining an accurate field solver with an efficient numerical optimizer one still may find ultra-compact bend configurations with almost 100% transmission of the fundamental mode, as demonstrated below, where we consider a 450nm wide trench waveguide that exhibits two propagating modes. In addition to the optimization of mirror- and resonator-based sharp bend structures, we introduce an ultra-small local photonic crystal in the bend area. Simulations have shown that this local PhC suppresses radiation and reduces problems caused by fabrication imperfections at the same time.

5.2 Simulation and optimization issues

Figure 5.1 shows the 3D model of the trench waveguide that will be fabricated on an InP substrate. Note that the wave is weakly confined in the vertical direction but strongly confined in the horizontal direction.

Since we intend to optimize the bend geometry, we need a highly efficient field solver that should be robust and accurate at the same time. Brute-force 3D time-domain computations are time consuming and often exhibit discretization noise that disturbs the optimization process. Therefore a 2D effective index model [9] is used and solved with the 2D MMP solver contained in the MaX-1 platform. The simplified 2D structure (width 450nm) is shown in Fig.5.1 (right-hand side) with effective index $n_{eff} = 3.236558$ ($\varepsilon_{eff} = 10.4753$), surrounded by air. The waveguide exhibits two TM modes (E field perpendicular to the 2D plane) at the telecommunication wavelength 1.55 μm. This wavelength choice is based on the constraints of our research. The propagation constants and field distributions of both modes are easily obtained from the MMP eigenvalue solver.

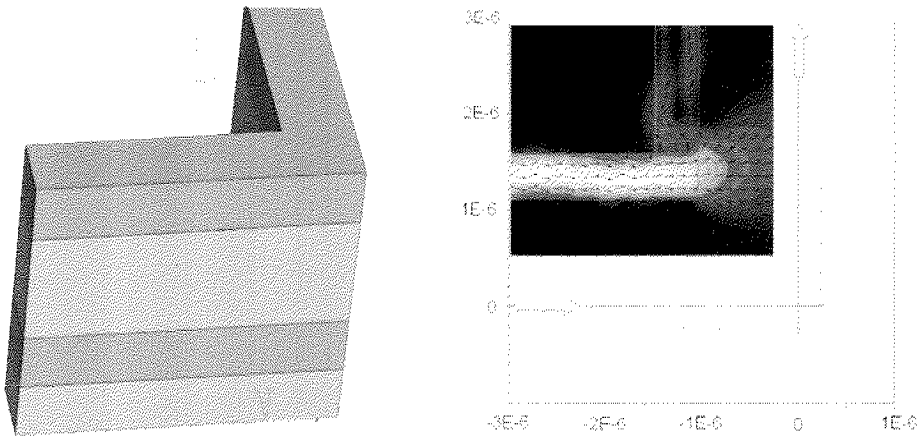

Fig.5.1 Schematic of the 3D structure (left hand side) and its effective 2D structure (right hand side) in our simulation, inset: Poynting vector at 1.55 μm.

Pioneering work for ultra-sharp bends were presented by Melloni et al. [11, 12], Manolotou et al. [6], Espinola et al. [7]. These configurations - based on complex physical rules and direct design methods - are difficult to master and limited in many ways. First of all, new structures with enhanced functionality can often not be obtained by physical intuition [15]. Like in the Inverse Design procedure (ID), we optimize the design parameters within some constrains in such a way that the transmission coefficient of the fundamental TM mode is maximized.

For complex optimization problems with many local optima, conventional optimization methods are not favorable. Genetic Algorithms (GA) [12] and Evolutionary Strategies (ES) are therefore widely used for solving such problems [10]. An (n + m) ES with n = 15, m = 100 and adaptive deviation values was used for obtaining the results shown in the following. Global optima were usually found within less than 25 generations. The parameter search space was limited to compact bend structures because structures with size much larger than the width of the waveguide are not desirable. The fitness function was specified as the transmission coefficient of the fundamental mode. Since high transmission may only be obtained when radiation, reflection, and mode conversion are simultaneously low, this simple fitness definition implicitly minimizes radiation, reflection, and mode conversion.

5.3 *Mirror type and resonator type bends*

The original sharp 90 degree waveguide bend structure is shown in Fig.5.1. The wave is incident from the left side while the output port is at the top of the figure. In this configuration, the transmission and reflection coefficients of the first and the second mode are T_1 = 1.83e-3, R_1 = 0.24, T_2 = 2.75e-2, R_2 = 1.02e-2. Obviously, most of the energy is radiated away from the bend, resulting in extremely poor transmission.

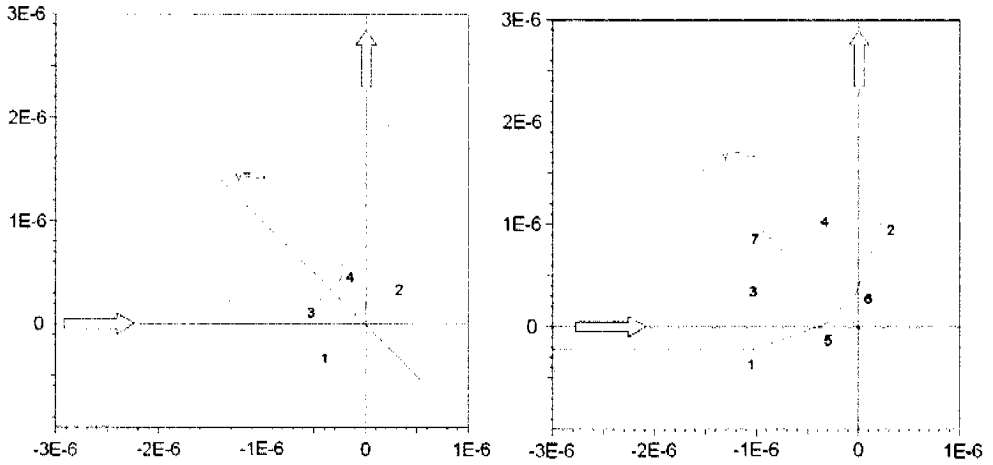

Fig.5.2 (a) 'Mirror' structure for the first optimization; (b) 'Resonator' structure used for the second simulation.

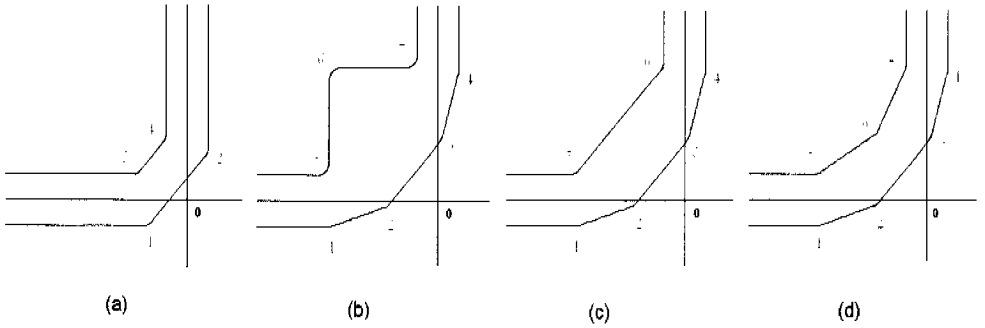

Fig.5.3 Selected optimization results with transmission above 90%. The global optima exhibit transmission above 98%.

When a 45 degree mirror or a 45 degree waveguide piece is introduced at the corner (see Fig. 2a), the transmission may be improved [6, 7]. Actually, many known structures [6, 7, 11, 12] may be obtained by changing the positions of the corner points 1, 2, 3, 4 shown in Fig.5.2(a) and Fig.5.2(b). When the designed structures are symmetric with respect to the line y = -x (dashed line in Fig.5.2(a)), only two parameters need to be optimized, i.e., the x coordinates of points 1 and 3. Optimization of two real-valued parameters is relatively easy and quick, but with more degrees of freedom one has the chance to find better solutions. Since it is reasonable to keep the symmetry with respect to y = -x, one may, for example, insert two points between the points 1 and 2 and another point (7) between the points 3 and

4 (see Fig.5.2(b)). This provides 3 additional real parameters for the optimization, namely the x and y coordinates of the new point 5 and the x coordinate of the new point 7.

Several selected results of the optimization procedure are shown in Fig.5.3. Note that the optimizer may find various local optima. As special cases, structures similar to those presented in other papers [6, 7, 11, 12] were found with the optimization procedure shown here. Note that the optimizer does not always find a structure proposed by other authors. This is either because it finds better solutions or because of optimization constraints that do not allow finding certain solutions. Since we search for ultra-compact solutions (i.e, ultra-compact structure), our constraints do not allow the optimizer to find big ones. Figure 5.3 lists the geometry of four typical configurations with high transmission. The global optima of these structures exhibit transmission coefficients above 98%. Each of these solutions has different properties concerning radiation, reflection, mode conversion, as well as sensitivity with respect to fabrication imperfections such as accuracy of the locations of the corner points and surface roughness. In order to overcome fabrication imperfection problems, one can add small PhCs as demonstrated in the next section. Note that PhCs will be added to a sub-optimal solution that might be obtained from an optimal one when fabrication tolerances of around 20nm affect both the locations of the corners and the radii of curvature in the corners.

5.4 Local PhCs in the bend region

Because of its photonic band gap, a PhC can act similar to a 'perfectly reflecting wall' within some frequency range. By properly selecting the geometry and material properties, one can design a PhC that provides total reflection within the desired frequency range. Instead of introducing a PhC acting as a 45 degree mirror [6, 7] near the waveguide corner, we arrange two very small PhCs on both sides of a not very well optimized 45° waveguide bend, for example, the one shown in Fig.5.3(a). When the coordinates of four corner points of the 45° bend (see Fig.5.2(a)) are set at 1: (-4.017e-7, -2.25e-7), 2: (2.25e-7, 4.017e-7), 3: (-4.41e-7, 2.25e-7), and 4: (-2.25e-7, 4.41e-7) - which corresponds to a sub-optimal solution that might be obtained due to fabrication imperfections - the transmission and reflection coefficients for the first and the second mode are $T_1 = 0.932$, $R_1 = 5.95e\text{-}4$, $T_2 = 1.43e\text{-}3$, $R_2 = 8.42e\text{-}4$, respectively. The resulting structure after adding two PhC parts is shown in Fig.5.4(b). The positions of the rods A and B are (1e-7,-1e-7), (-6e-7, 6e-7), respectively. The PhCs consists of circular rods with radii r = 120 nm on a square lattice with lattice constant a = 600 nm, the circular rods have the same material properties as the waveguide. Therefore, the PhCs can be fabricated in one step together with the trench waveguide, only the mask for the etching needs to defined using electron-beam lithography accordingly. Furthermore, the normalized band diagram (not show here) shows that the operation wavelength $\lambda = 1.55$ μm is in the center of the first band gap (Note that $a/\lambda = 0.3\text{-}0.42$ corresponds to the wavelength range $\lambda = 1.43\text{-}2.0$μm.).

The Poynting vector of the structure in Fig.5.4(b) is shown in Fig.5.4(c). The transmission of the first mode has improved to $T_1 = 0.9830$ but this structure is still not optimal. The additional 21 rods provide 63 additional optimization parameters (coordinates and radii). Using symmetry constraints, with respect to y = -x, the number of additional parameters is 31. For current solvers, it would be extremely time consuming to optimize this parameter space. From the optimization of the 90 degree PhC waveguide bend [5] it is known that the transmission is most sensitive to rod A.

When moved a little bit, i.e., from its original location (1e-7,-1e-7) to (2e-7,-2e-7), the transmission of the first mode is improved to T_1=0.9964 (see Fig.5.4(d)). Since this value is very close to the ideal value 1, further optimization is not required.

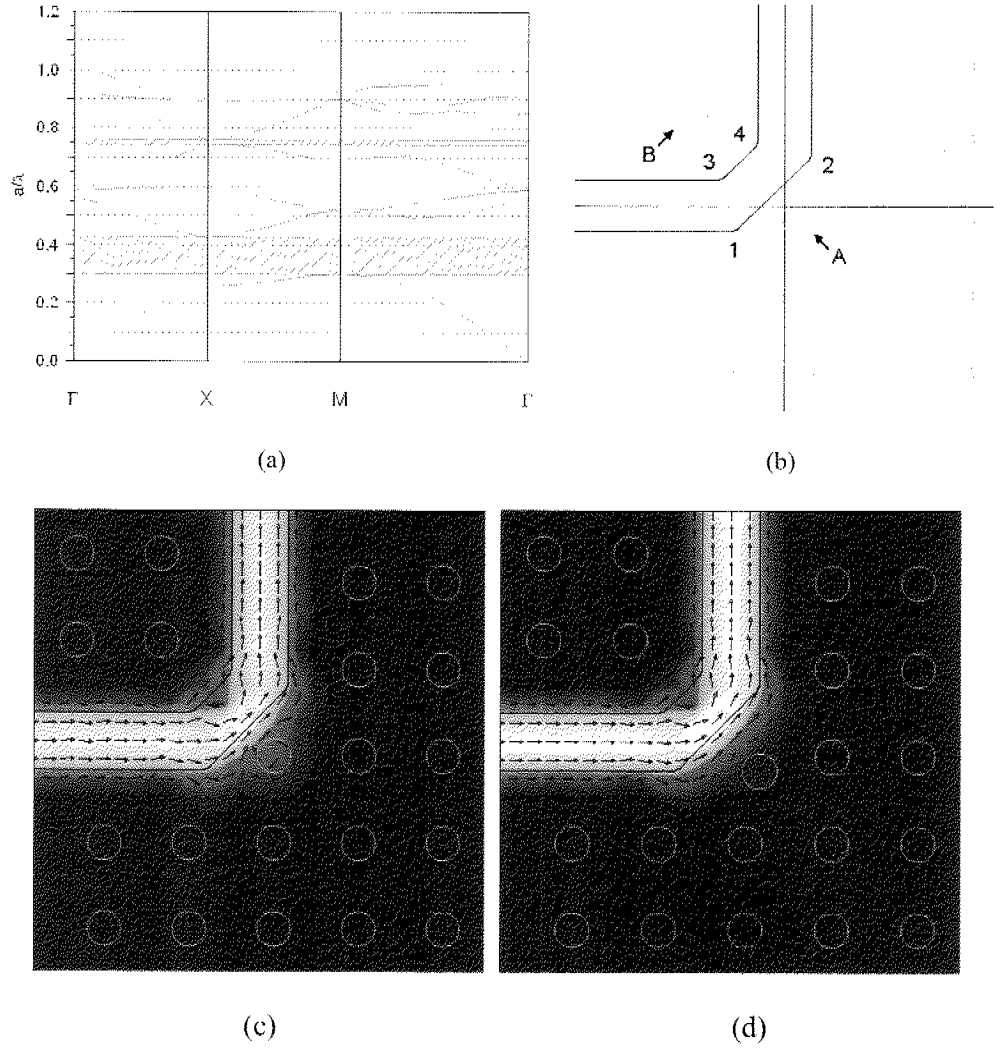

Fig.5.4 (a) Band diagram of PhCs; (b) Schematic of Bend structure shown in Fig.5.3(a) after PhC rods are put on the bend corners; (c) Poynting vector field for the structure shown in Fig.5.4(b). At λ = 1.55 μm one has T_1 = 0.9830, R_1 = 4.35e-3, T_2 = 1.40e-3, R_2 = 9.48e-4. (d) Rod A moved from (-1e-7, 1e-7) to (2e-7,-2e-7). At λ=1.55μm one now has T_1=0.9964, R_1=4.24e-4, T_2=4.95e-4, R_2=3.82e-5.

5.4.1 Fabrication imperfections and perturbations

Because of fabrication imperfections, one has to face several problems caused by the etching process. Many of them have to do with 3D aspects that cannot be taken into account in a 2D model but some of them can at least be estimated with 2D models. Two of them are considered in the following: 1) inaccurate locations of the bend corners and inaccurate radii of curvature in the corners and of the PhC rods and 2) surface roughness. Scattering loss due to surface roughness was investigated decades ago [13] based on perturbation theory. According to this theory, the roughness can be interpreted as a superposition of gratings with different periods, where each grating period causes coupling to specific radiation modes. For the sake of simplicity, only a

periodic, sinusoidal perturbation along the sidewalls of the trench waveguide is introduced to characterize the roughness. Table 1 shows that the local PhC reduces the influence of the roughness on the transmission of the fundamental mode. As one can see, the transmission reduction of the first mode of the structure without photonic crystal (case 1) is larger than when the PhCs are present (case 2).
To check the influence of displacement of the corner points of the bend (shown in Fig.5.3(a), as Fig.5.4(a)), two schemes are used: (1) corner 1, 3 are shifted along the x direction and corner 4, 2 are shifted along the y direction; (2) Corner 1 and 2 are shifted along the x and y direction respectively while the other corners are fixed. Figure 5 shows the change in the transmission as a function of the displacement error due to fabrication. From this one can see that also the influence of inaccurate corner locations is reduced when the small local PhCs are present.

Table 5.1 Comparison of the transmission of the fundamental mode for a bend structure (shown in Fig.4a) without and with local PhCs after perturbation was introduced.

Perturbation Amplitude (nm)	T_1 without PhCs (case 1)	T_1 with PhCs (case 2)
0	0.9330	0.9969
5	0.9003	0.9677
8	0.8730	0.9473
10	0.8492	0.9267
20	0.6736	0.7665
30	0.4491	0.5427

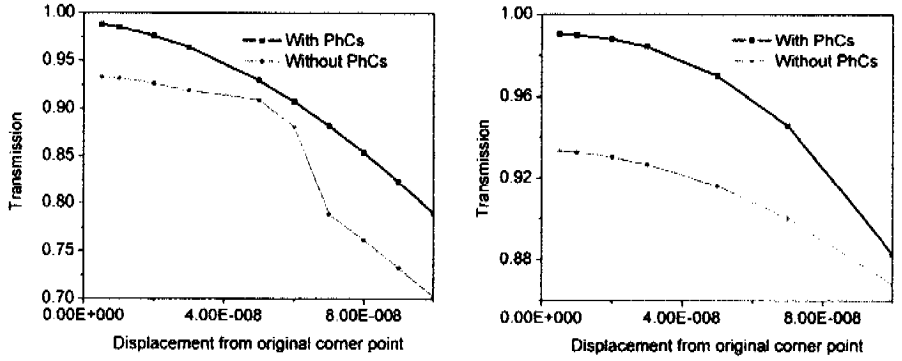

Fig.5.5 Corner displacement .vs. transmission at 1.55μm. (a) for scheme 1; (b) for scheme 2 with (black curve) and without (red curves) the local PhCs.

5.5 *Fabrication and measurement*

5.5.1 Fabrication

General fabrication steps for semiconductor devices include wafer growth, oxidation, photo lithography, etching, ion implantation, and metallization. Each step also includes several different methods according to the requirements of material characteristics, fabrication accuracy, etc.

The fabrication of the bend structures presented here has been done by people in the Electronics Laboratory. For this, the facilities in the FIRST lab at ETH were used. The fabrication process uses three mask layers. The first mask is for the deposition of the alignment markers, they are used for the alignments of the subsequent masks, which contains the bend structures. The second mask step is the fabrication of the

bend structures and accessing trench waveguides. The mask consists of 400nm silicon nitride, 30nm Titanium, and 210nm Polymethyl methacrylate (PMMA) [16]. The design is firstly patterned onto the PMMA layer by electron beam lithography. Then it is subsequently transferred by reactive ion etching to the Ti and the SiN layers, using the upper layer as the mask [16]. Finally, the whole structure is deeply etched into the InP/ InGaAsP semiconductor stack by inductively coupled plasma reactive ion etching [17].

The final three-dimensional structure has a 200nm top cladding layer with InP and a 400 nm InGaAsP core layer followed by a 500nm InP bottom layer. The substrate also was etched and the whole etching depth is close to 3μm [19].

5.5.2 Experiment setup and characterization

To measure the transmission of the fabricated bend structure, a system based on end-fire technology has been built in the FIRST lab of ETH. The schematic configuration and layout of the measurement system are shown in Fig.5.6 and Fig.5.7 [19]. A tunable laser with span range 1465-1631nm was used, followed by a series of polarization controllers, combiners, and inline polarizers. At the end of the in-coupling system, a polarization-maintaining tapered lensed fiber with a spot size of 3.5 ± 0.5μm is used to couple light into the sample through the fiber holder [18]. The holder used for fixing the fiber can be moved in the spatial direction with a linear micrometer. The x and y directions are motorized [18]. The sample is put on the stage with 6-axis adjustments. At the output part, the same lensed fiber and holder are used and the fiber is connected with an IR InGaAsP photodetector. Since the spot size of the output fiber is larger than the output waveguide of the sample, a pinhole is placed between the fiber and sample to ensure that only the light from the waveguide is measured [16, 19].

The measurement results are shown in Fig.5.11 and Fig.5.12. Unfortunately, the manufacturer did not fabricate a reference waveguide (on the same chip or using the same fabrication procedures for the straight reference waveguide). As a consequence, one can get less information about the device performance from the measurement results, because there is no reference waveguides that could be used to calibrate the device measurements and to extract the transmission properties of the sample itself. From Figs.5.11 and 5.12, we can see that the transmission of the mirror-type bend improved almost 2dB compared with the sharp bend (see, Fig.5.11). Also from Fig.5.12, we found that the local PhC parts not only help to suppress the radiation but also provide the solution to fabrication tolerance: when local PhCs are present, higher transmission is possible. But we also need to be aware of that the simplified model in 2D, fabrication process, measurement setup are worth of checking regarding the performance. In the next section, we will try to find the approaches to improve the performance of the device based on the limited information provided by the manufacturer.

5.5.3 Data analysis and error checking

The steps shown below are used to check the possible inaccuracies that are caused by the fabrication, measurements, and also in the simulation.

First, the exact dimensional size of the fabricated structures from SEM micrographs is extracted for additional 2D simulations. The measured size is shown in Fig.5.13 with ± 10 nm errors. As one can see from the extracted dimension size, the straight waveguide part along horizontal is 423nm ± 10nm while the vertical part is 435 ± 10 nm. Furthermore, both are less than the 450nm width used during the

numerical design optimization. The locations of the bend corners are displaced more than 20 nm (average value) from optimal design positions. Since the fabricated structure is not uniform and the bend part is not easy to be characterized, only average values of important bend data are used for the additional 2D simulations where the original 450nm width is kept. The simulation result in Fig.5.14 shows that perturbations of the geometry are one of the possibilities that could cause lower transmission compared with the optimal design results.

When one checks the fabrication procedures, the following can be found. When the wafer is ready, the designed waveguide bend is defined in an e-beam resist by e-beam lithography, that is, the bend design is patterned onto the PMMA layer. After this, the bend design is subsequently transferred by reactive ion etching. Finally, the waveguide is deeply etched. The most likely reason for reduced waveguide widths and displacements is from a mask alignment error. From the SEM micrographs, some substantial proximity effects can be observed and thus a deliberate proximity effect correction is needed when transferring the design pattern onto the resist layers. This also holds when PhCs are present during fabrication.

Furthermore, we check the measurement setup. The lensed fiber has a spot size 3.5μm lager than the waveguide core cross section. Therefore, the coupling to the waveguide is a big issue. If the in-coupling wave is not well focused on the core layer of the trench waveguide, some energy will go into the substrate and some energy will propagate along the etched air part, resulting in less transmission and higher substrate loss and scattering loss. In most experiments with end-fire technology, a micro-lens (or conventional injection aspherical lens) with high Numerical Aperture (NA) was used to efficiently focus the in-coupling light on a small spot size. Compared with fiber injection, coupling with a lens is easier and the spot size can be controlled better. Thus the light could be concentrated on the core region of the trench waveguide. Another issue is the role of the pinhole. In the experiment, the role of pinhole is to shield unwanted in-coming light, i.e., eliminate scattering light [18]. Actually, one can explain the effect of the pinhole by means of the imaging system. Generally, a small pinhole will result in better image resolution when the projection is smaller at the image plane. When the hole is extremely small, significant diffraction effects can be produced which will result in a less clear image [20]. Shading also affects the quality of imaging. The optimal pinhole diameter is given by Lord Rayleigh [20]:

$$d = 1.9\sqrt{f\lambda} \tag{2}$$

where d is diameter, f is focus length (here, it is the distance from the hole to the lensed fiber) and λ is the wavelength of light. As one can see in the following, if the diameter of pinhole is 1μm and when the wavelength of light is 1.55μm, the optimal focus length is 0.17μm for a good resolution. This causes severe difficulties to align the lensed fiber. Therefore, without very good alignment and measurement setup considerations, bad results are inevitable. Another aspect that can not be neglected is that the shielded light by the pinhole may be partly reflected back into the trench waveguide. Thus it affects the measurement results at the out-coupling side.

Finally, three-dimensional structure simplifications in the simulations should be carefully treated. When two-dimensional models based on the effective index method are used, the off-plane loss of realistic 3D structures with finite size is omitted. To make the 2D results – required during the optimization for reducing the computation time - comparable with realistic 3D results, more precise 2D approximation methods are needed.

5.6 Summary

Sharp dielectric trench waveguides with small photonic crystals for suppressing radiation have been analyzed using the highly accurate MMP solver combined with Genetic Algorithm and Evolutionary Strategy optimizers. The simulation shows that the bend structures with photonic crystals are less sensitive to the displacement of bend corner positions and surface roughness because of fabrication errors. The improvement of the performance provides additional advantage to integrate it into high density optical circuits. As the first fabrication test was not so successful, possible reasons that were caused by inaccurate fabrication processes, measurement setup, and also inaccuracies of the numerical models were discussed.

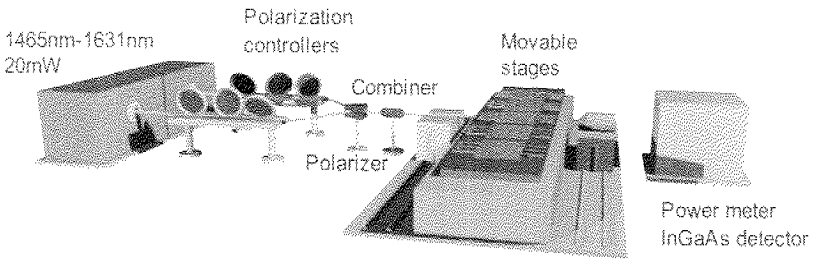

Fig.5.6 Schematic of the end-fire setup for the measurement of transmission of waveguide bend structures.

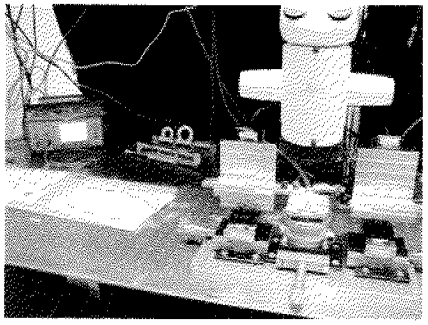

Fig.5.7 Experimental layout.

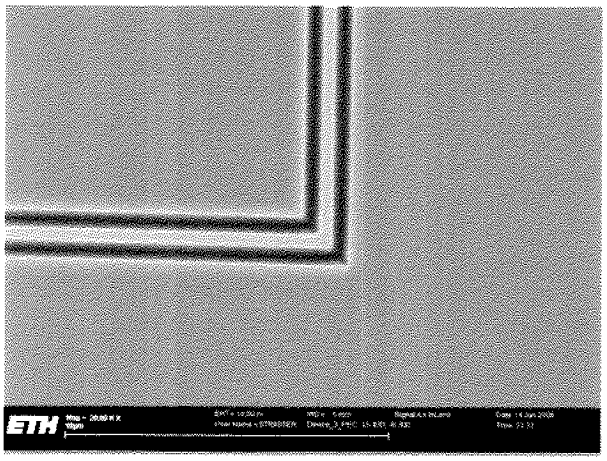

Fig.5.8 SEM of original sharp trench waveguide bend.

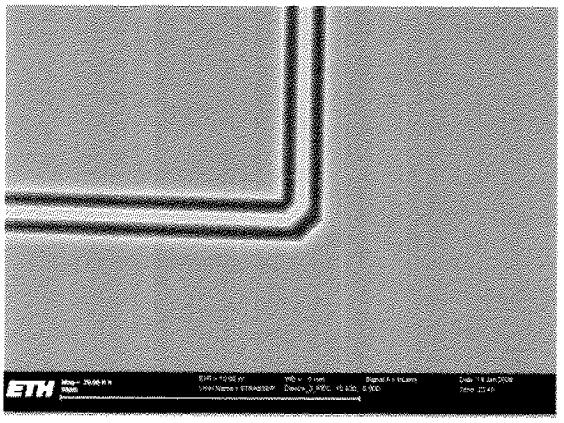

Fig.5.9 SEM of mirrors-type trench waveguide bend.

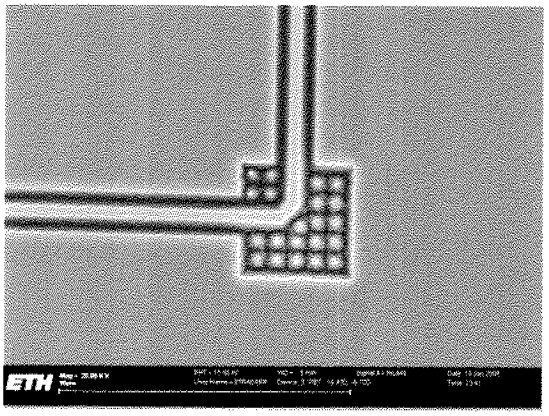

Fig.5.10 SEM of mirror-type bend with photonic crystals

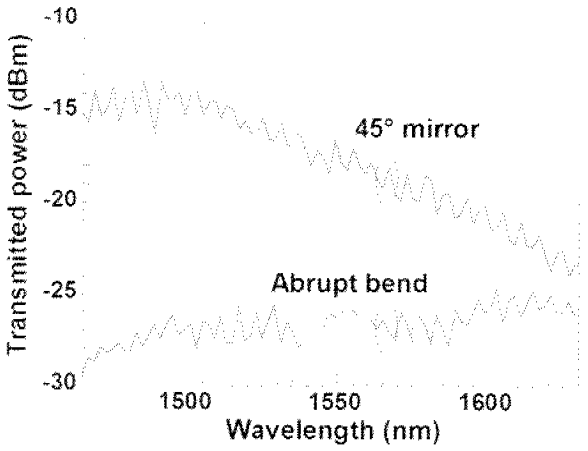

Fig.5.11 Transmission measurement results of abrupt bend and 45 degree mirror structures.

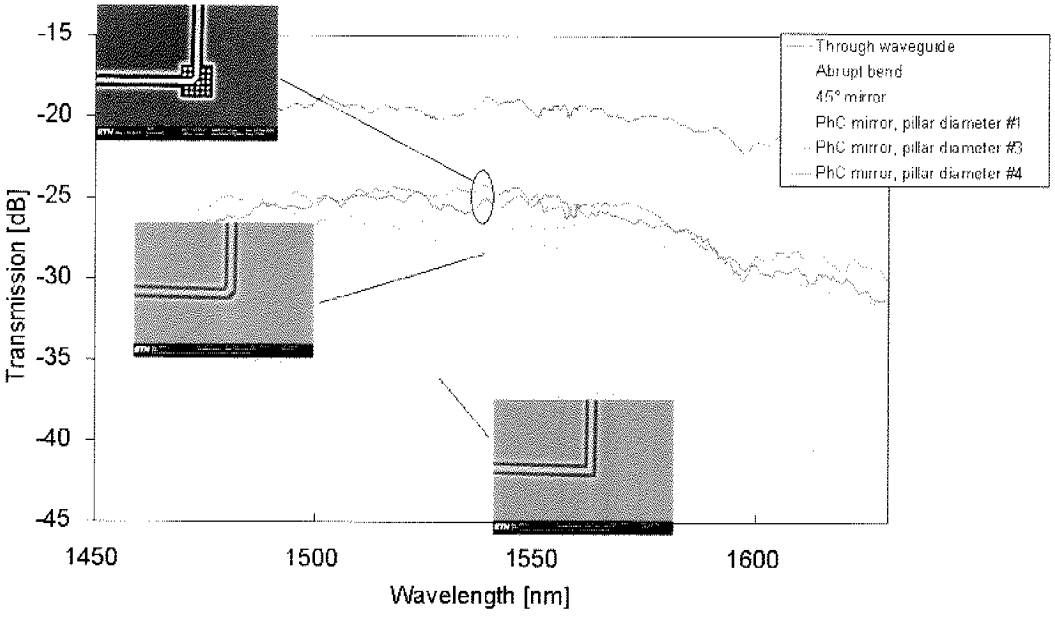

Fig.5.12 Comparison of measured transmission data for different bend structures with and without PhCs.

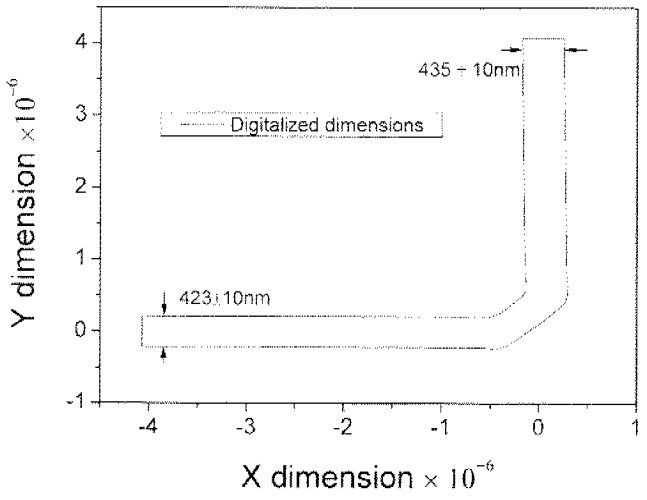

Fig.5.13 Digitalized dimensions of bend from SEM picture shown in Fig.9.

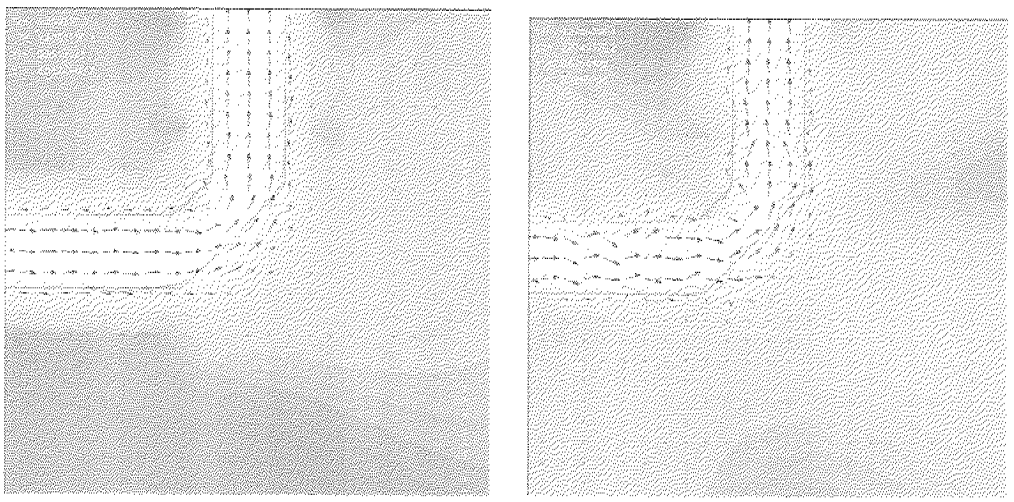

(a) (b)

Fig.5.14 Perturbation simulation for the waveguide bend part. The boundaries with green and red color denote perturbed locations. Random periods are used in simulation. (a) The perturbation amplitude for the outer boundary is less than for the inner boundary, T1=0.95; (b) The perturbation amplitude for the outer boundary is bigger than for the inner boundary, T1=0.62.

References

[1] H.F. Taylor, "Losses at corner bends in dielectric waveguides," *Appl. Optics* **16**, No. 3, pp 711-716 (1977).

[2] Toru Shiina, Kazuo Shiraishi, and Shojiro Kawakami, "Waveguide-bend configuration with low-loss characteristics," *Opt. Lett.* **11**, No. 11, pp736-738 (1986).

[3] Han-Bin Lin, Jung-Young Su, Pei-Kuen Wei, and Way-Seen Wang, "Design and Application of Very Low-loss Abrupt Bends in Optical Waveguides, " *IEEE J. Quantum Electronic* **30**, No. 12, December, pp 2827-2835 (1994).

[4] http://alphard.ethz.ch/hafner/MaX/max1.htm.

[5] Jasmin smajic, Christian hafner and Daniel Erni, "Optimization of photonic crystal structures," *J. Opt. Soc. Am. A* **21**, 2223-2232 (2004).

[6] C. Manolatou, Steven G. Johnson, Shanhui Fan, Pierre R. Villeneuve, H. A. Haus, and J. D. Joannopoulos, " High-Density Integrated Optics, " *Journal of Lightwave Technol.* **17**, No. 9 (1999).

[7] R. L. Espinola, R. U. Ahmad, F. Pizzuto, M. J. Steel and R. M. Osgood, Jr. "A study of high-index-contrast 90 degree waveguide bend structures, " *Opt. Express* **8**, No. 9, pp 517-528 (2001).

[8] http://wwwhome.math.utwente.nl/~hammer/eims.html.

[9] Gregory P. Nordin, Seunghyun Kim, Jingbo Cai, and Jianhua, Jiang, "Hybrid integration of conventional waveguide and photonic crystal structures," *Opt. Express* **10**, No.23, November (2002).

[10] Cui Xudong, Christian Hafner, Ruediger Vahldieck, "Design of ultra-compact metallo-dielectric photonic crystal filters," *Opt. Express* **13**, pp. 6175-6180, August (2005).

[11] Andrea Melloni, Federico Carniel, Raffaella costa, and Mario Martinelli, "Determination of Bend Mode Characteristics in Dielectric Waveguides," *J. lightwave technol.* **19**, No. 4, April (2001).

[12] Andrea Melloni, Paolo Monguzzi, Raffaella Costa, and Mario Martinelli, "Design of curved waveguides: the matched bend," *J. Opt. Soc. Am. A* **20**, No.1, January (2003).

[13] D. Marcuse, "Mode conversion caused by surface imperfections of a dielectric slab waveguide," *Bell system Technical J.* **48**, pp 3187-3215 (1969).

[14] J. Merle Elson, "Propagation in planar waveguides and the effects of wall roughness," *Opt. Express* **9**, No. 9, pp 461-475 (2001).

[15] Andreas Hakansson, Jose Sanchez-Dehesa, and Lorenzo Sanchis, " Inverse Design of Photonic Crystal Devices, " *IEEE Trans. On Selected Areas in communications* **23**, No. 7, pp1365-1371 (2005).

[16] R. Wuesst, P. Strasser, F. Robin, D. Erni, H. Jaeckel, "Fabrication of a hard mask for InP based photonic crystals: Increasing the plasma-etch selectivity of PMMA versus SIO_2 and SIN_x," *J. Vac. Sci and Techn. B* **23**, No. 6, pp3197-3201, (2005).

[17] P. Strasser, R. Wueest, F. Robin, K. Rauscher, B. Wild, D. Erni, H. Jaeckel, "An ICP-RIE etching process for InP based photonic crystals using $Cl_2/Ar/N_2$ chemistry," *17th Int. Conf. Indium Phosphide Related Materials*, pp. TuP-24 (2005).

[18] K. Rauscher, *DISS. ETH. Nr.* **16516**, PhD dissertation, ETHZ (2006).

[19] F. Robin, *INIT meeting powerpoint*, ETHZ (2006).

[20] http://en.wikipedia.org/wiki/Pinhole_camera.

6 Resolution of negative index slabs

After the fabrication of metamaterials with negative index of refraction, the research of negative index materials became a hot topic. Negative Index Metamaterials (NIMs) essentially are metallic PhCs with lattice constants considerably smaller than a wavelength. Their most promising application is the so-called 'perfect-lens' or 'super-lens', made by negative index slabs. To clarify some issues still under debate, the resolution of negative index slabs is discussed in this chapter. Different definitions of the optical resolution of NIM slabs and of classical optical lenses with magnification 1 are presented and evaluated for both cases. Several numerical codes – based on domain and boundary discretizations, working in the time- and frequency-domain – are applied and compared. It is shown that super resolution depends very much on the definition of the resolution and that it may be obtained not only for NIM slabs but also for highly refracting classical lenses when the distances of the image and source points from the surface of the lens or slab are shorter than the wavelength.

6.1 Introduction

Materials with a negative index of refraction are obtained when the permittivity and the permeability are simultaneously negative. The fundamental electromagnetic properties of such materials were first theoretically studied by Veselago [1]. Since negative permittivity is common for metals at optical frequencies, it was natural to think about NIMs or Left-Handed Materials (LHMs), but almost no attention was paid to this early work (because such materials were never observed in nature). This situation changed dramatically after 1) Pendry [2] realized that artificial metamaterials with negative refractive index might be fabricated and that such materials might be used to create a new type of optical lens that was first called "perfect" lens, and after 2) such materials were fabricated and characterized at microwave frequencies [3]. It soon became apparent that the declaration of a NIM slab as a "perfect" lens was an exaggeration and that such a slab does not image a point source S on an image point or focus point F as suggested by the simplified ray model illustrated in Fig.6.1. Note that an internal focus point X is present also inside the NIM slab. However, numerical simulations [13, 14, 15, 23, 25, 28] show that areas of strong fields around the points X and F are present and that these areas may be smaller than half the wavelength. This would allow to obtain an imaging system that breaks the well-known optical limit of conventional lenses. Detailed analytical studies [4] show that super-resolution is only obtained when the slab is not thick compared with the wavelength.

When the NIM slab is thin, quasi-static considerations become valid because of weak electromagnetic coupling. Therefore, super-resolution can be obtained without a negative index when either the permittivity or the permeability is negative. Thus, a thin metallic slab with negative permittivity is sufficient for observing super-resolution imaging in the near field [5, 6]. To prove this, the photoresist in the experiment published in [6] was placed directly on the silver film (i.e., on the slab with negative permittivity). Therefore, this experiment is closer to contact lithography than to optical imaging with a lens. Furthermore, the absolute values of the refractive indices of the slab, with photoresist on one side, and the PMMA on the other side of the slab are almost 1.5. Thus, the wavelength in this structure is shorter than the wavelength of free space, which automatically improves the resolution. Beside this

modified configuration, the experimental verification of "super-resolution" of a NIM slab at optical frequencies is still outstanding.

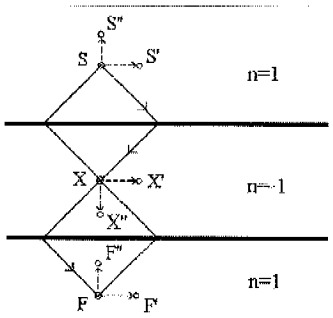

Fig.6.1 A point source S illuminates a NIM slab. Inside the slab, an internal focus point X and on the other side of the slab the image point (focus point) F is obtained.

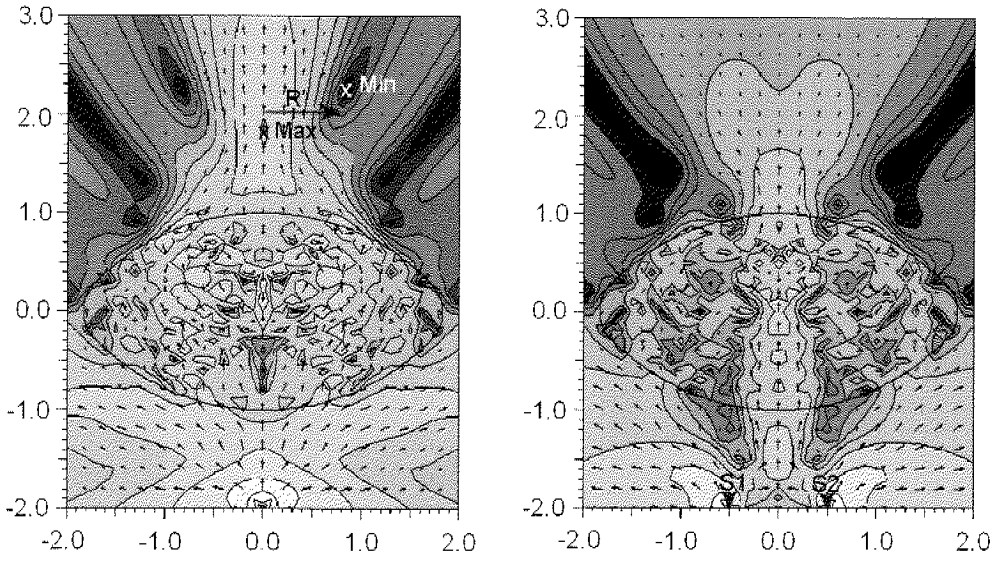

Fig.6.2 2D model of a small, conventional lens with refractive index n = 2.5 illuminated by a centered point source (left) and by two symmetric point sourced (right). Time average of the Poynting vector field obtained from the MMP solver in the MaX-1 platform. Coordinates indicated in wavelengths.

Since the fabrication of metamaterials for microwaves is much easier than for optical frequencies, various microwave experiments were performed. In recent experiments [13, 14], a NIM slab (dimensions not further specified) and a 3D photonic crystal with NIM properties were fabricated and illuminated by two microwave sources at wavelength λ = 27.8mm and 18.4mm, respectively. "Sub-wavelength" resolution of 0.44λ was observed in both experiments with two sources.

The term super-resolution is often used in NIM and LHM papers when the wavelength between neighboring peaks in the image space of below 0.5λ is observed for 2 [14] or more [15] sources, and it is implicitly assumed that 0.5λ is the limit of resolution for classical lenses. In fact, the classical Rayleigh criterion for the optical resolution is based on the distance between two point sources, i.e., it is defined in the object space rather than in the image space. To clarify the situation, we consider numerical simulations of classical lenses in the following section, where we introduce different definitions of the resolution (based on observations in the object and image

space) and demonstrate that also classical lenses can have a resolution below 0.5λ. After this, we perform a detailed numerical analysis of NIM slabs and consider the influence of size, shape, material loss, and photoresist properties on the resolution.

NIMs may have very different electric and magnetic properties. For obtaining low or even no reflection of waves impinging from free space on a NIM, one usually considers only NIMs with a complex relative permittivity that is equal to n = a+ib, where *a* is usually -1 and *b/a* is the loss tangent assumed to be small. In the following, we focus on such impedance-matched NIMs with n = -1+ib.

6.2 *Resolution of conventional lenses*

Simple conventional lenses consist of an almost loss-free dielectric medium with an optical index n>1 and a piecewise spherical shape. Usually, the resolution is defined by the Rayleigh criterion. First, it is observed that the image of a point source consists of a bright spot surrounded by Airy rings caused by negative interference. When a second point source is placed in such a way that its central image spot is on the first Airy ring around the first spot, the two spots may be detected. The distance between these two source points is then defined as the resolution $R_{Rayleigh}$.

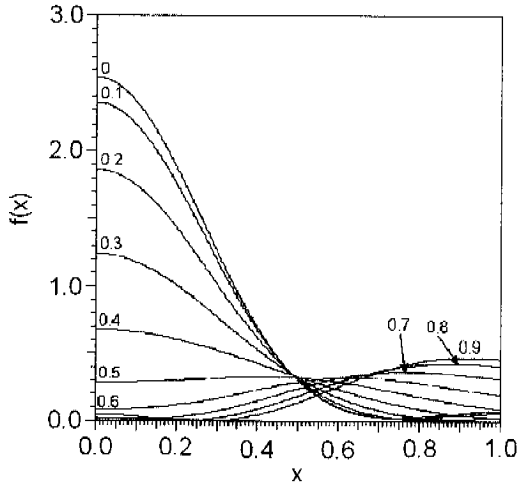

Fig.6.3 Illumination (time average of the y component of the Poynting vector field) along the line at y=2λ for two sources shown in Fig. 2, with coordinates ±x, y = -2λ. The location x is indicated as parameter of the different curves.

For lenses with magnification 1 (the NIM or LHM slab can only have magnification 1!), the resolution R_1' (the prime indicates the image plane, the index indicates the number of source points required for the definition) may be defined simply from the image of a single point source as the distance between the maximum and the first local minimum (first Airy ring) in the image plane, which considerably simplifies the numerical computation of the resolution. This definition of the resolution is usually used when configurations with a single source are considered. As mentioned in the introduction, one can also define the resolution R_2', which is the distance between two image peaks obtained from two point sources. Another alternative is to define the resolution R_2 as the distance between two point sources that cause an image with two visible maxima in the image plane. For lenses with magnification 1 one might expect that R_2' is equal to R_2. In fact, this is not the case. When the distance d between the source points is small enough, only one image spot

is observed. This spot is broadened with increasing d until two spots become visible. When this happens, the distance d' between the spots is strongly different from the distance d. A more sophisticated definition of the resolution of a lens with magnification 1 is therefore the following. When the distances d and d' are observed simultaneously while d is increased, one obtains d = d' at several distances d_i. R_2' may then be defined as the smallest d_i. These definitions of the resolution will be considered in more detail in the following.

For large lenses with a focal plane that is relatively far away from the lens, the Rayleigh resolution approaches 0.5λ, but for small lenses it is above this value as illustrated in Figs 6.2 and 6.3. Note that, for reasons of simplicity, only 2D models are considered in the following. Despite of this simplification, the situation is still rather complicated. First of all, the location of the image plane for a small lens is not obvious. In Fig.6.2, one observes a maximum field intensity near y' = 1.8λ and the first local minimum near y' = 2.2λ. Note that coordinates with primes indicate image points. When the image plane is at y' = 1.8λ, one obtains a better resolution than for the image plane at y' = 2.2λ - at the price of lower contrast because the ratio of the amplitudes of the maximum illumination and illumination of the first local minima at y' = 1.8λ is smaller than at y' = 2.2λ.

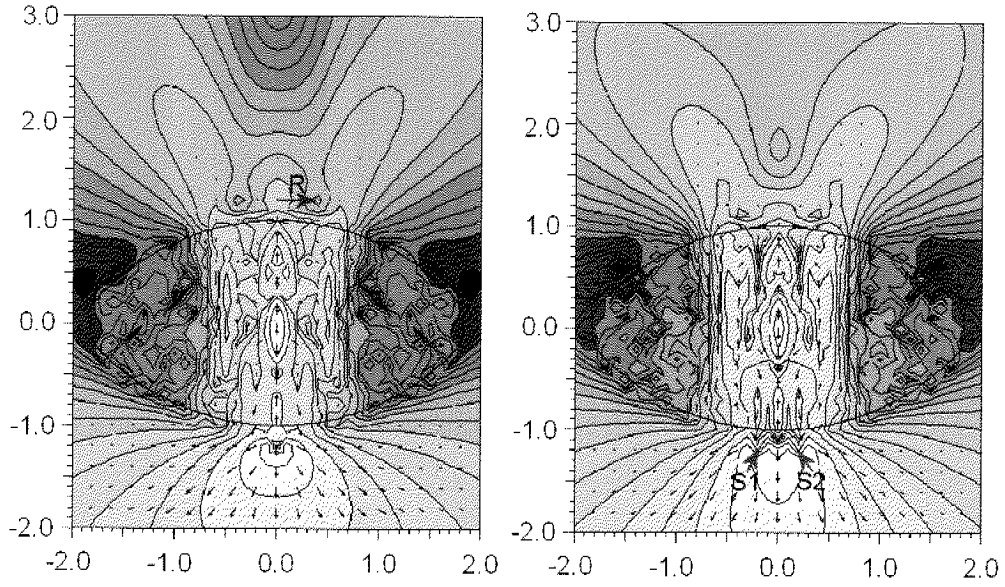

Fig.6.4 Same as in Fig.6.2 but for a lens with a high optical index of n = 10.

As a compromise, Fig.6.3 shows the illumination along the line y' = 2λ for two symmetric point sources at y = -2λ. This also implies that the magnification is equal to 1. The curve in Fig.6.3 with x=0 corresponds to a single source. As seen from this, the resolution R_1' is around 0.75λ, i.e., considerably above 0.5λ. From the curves for two different sources it is obvious that a single maximum at x' = 0, y' = 2λ is present as long as the distance d = 2x between the sources is smaller than the wavelength. This also means that when the two sources are placed according to the Rayleigh criterion, with a distance d = 0.75λ between the sources, one only observes a single maximum. Thus, this criterion is of questionable value for small lenses. For bigger distances d, one observes two equal maxima along the image line y' = 2λ with distances d' = 2x'. It can be seen from Fig.6.3 that R_2 is slightly below 1λ for the lens considered in Figs 6.2 and 6.3 because only a single maximum at x'=0 is observed for two source located

at x = d/2 = 0.4λ, whereas 2 maxima are observed near x' = ±0.5λ. Furthermore, R_2' is slightly above 1λ. Note that for a precise computation of R_2, R_2', and R_2' many simulations with varying d must be carried out and analyzed. This not only causes considerable computation time but also some post-processing of the data that is rather cumbersome for many codes, especially because numerical inaccuracies my lead to some noise which causes difficulties in the accurate detection of maxima and distances between maxima.

Figures 6.4 and 6.5 show that the resolution of a small lens can be drastically improved when the index of refraction of the lens is increased in such a way that the distances of the source and image points from the surface lens are below one wavelength. For a small lens with n = 10 and distances of the sources and image plane from the lens surface around 0.2λ, one obtains R_1' = 0.37λ and R_2 = 0.42λ, i.e., super-resolution in the sense R_1'<0.5λ and R_2<0.5λ. Incidentally, R_2' and R_2' are above 1λ, i.e., whether super-resolution is observed or not also depends on the definition of the resolution. Note that super-resolution of a conventional lens requires distances of the image and source points from the surface of the lens that are smaller than the wavelength, but the distances between source and image points may exceed the wavelength.

6.3 Time domain analysis

Currently, time domain methods that discretize the entire field domain are most frequently used in computational electromagnetics. Among these, FDTD is most prominent and widely used because of the simplicity of its concept. As all time-domain codes, FDTD has substantial problems with frequency-dependent material properties, i.e., dispersive media. Veselago already pointed out that NIMs must be dispersive for making sure that the group velocity in such a medium does not exceed the speed of light. In order to avoid explicit convolution integrals and for obtaining codes with reasonable performance, only relatively simple models such as the Debye, Drude, and Lorentz model are implemented in commercial FDTD solvers such as XFDTD [16], OptiFDTD [17], Empire [18], and closely related FITD solvers such as Mafia and Microwave Studio [19].

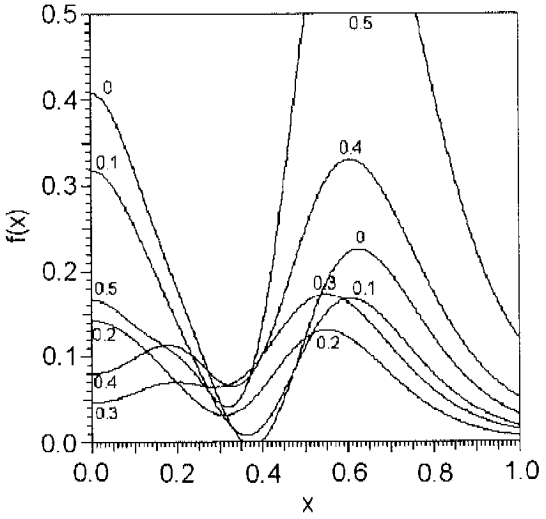

Fig.6.5 Same as in Fig.6.3 but for a lens with a high optical index of n = 10.

For NIM simulations such dispersive models must be implemented for both the permeability and the permittivity. Currently, most commercial FDTD solvers provide dispersive models for the permittivity only, with one exception: XFDTD. Therefore, FDTD simulations of NIM slabs [10, 16] are either based on non-commercial software or on XFDTD.

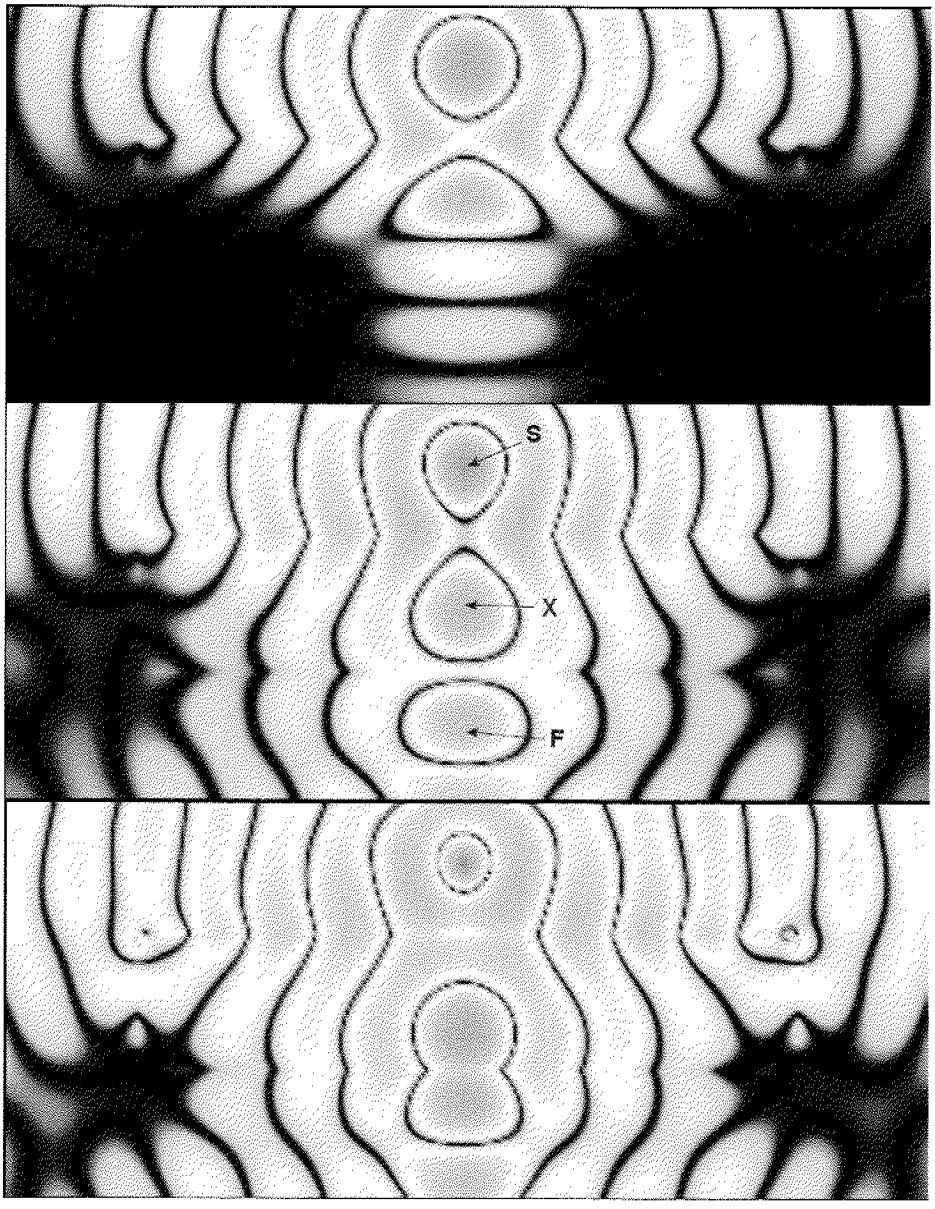

Fig.6.6 XFDTD simulation of a 2D NIM slab of width 1λ, length of 5λ, illuminated by a point source S with electric field E perpendicular to the plane, E field intensity at different times. Top: after 5 periods, center: after 10 periods, bottom: after 20 periods.

Figure 6.6 shows the evolution of the electric field for a NIM slab of finite length (rectangular shape) illuminated by a point source obtained from an XFDTD simulation with a lossy Debye model for the permittivity and permeability (plasma frequency 2.655e11 *rad/s*, collision frequency 10e-8 *rad/s*; at a frequency of 30GHz, the complex relative permittivity and permeability are -0.99+0.00106*i*). It can be observed that first a strong field along the surface near the source S is established.

With the field propagating in the slab, a field along the surface on the opposite side is established. Finally the focus point F is illuminated. The field around F has a beam-like shape coming out of the slab with a width broader than 0.5λ. Then the field becomes more complicated and the spot around F becomes smaller. The convergence of the field around F toward steady state is rather slow. Therefore, thousands of FDTD iterations are required for obtaining sufficiently accurate estimates of the steady state.

Similar observations are made when Mefisto3D [9], another commercial time domain solver is applied, as one may see from Fig.6.7. Mefisto3D is a TLM-TD code that is based on a grid of transmission lines. For handling NIMs, this code uses a special network of transmission lines, i.e., the dispersion characteristics of the NIM slab are different from those of the FDTD simulation.

In general it has been our experience that because of the high number of iterations to reach steady state, the limited accuracy and the difficulties in the post-processing of the results, time domain codes are not very well suited for extensive studies on the resolution of the NIM slab. Therefore, frequency domain codes are applied in the following.

6.4 Finite Element Analysis

Beside FDTD, the Finite Element Methods (FEM) is widely used both in frequency and time domain. Prominent FEM codes are HFSS [20] and FEMLAB [21]. The latter allows relatively simple post-processing of the results using MATLAB [22]. Frequency domain codes have no essential problems with NIMs. Therefore, the frequency domain version of the FEM [21] in the commercial coded FEMLAB is often used for the NIM analysis [13, 29].

It is well known that the unstructured mesh used in FEM is advantageous because it provides a better approximation of the material boundaries, but at the same time the mesh generation is crucial and has a strong influence on the results. Therefore, commercial FEM codes provide automatic mesh generation and mesh refinement. Figure 6.8 shows the mesh for a NIM slab obtained from the automatic mesh generator of FEMLAB after the first and second automatic refinement. Obviously, the mesh is extremely fine near the source point. In fact, FEMLAB does not allow to use point sources. Instead small, circular source areas can be introduced. Depending on the size of these sources, the mesh surrounding them becomes very fine which leads to large FEM matrices, i.e., memory requirement and long computation time. It is important to note that FEM matrices usually are sparse. Therefore, iterative matrix solvers such as GEMRES may reduce the computation time for large matrices. FEMLAB contains various direct and iterative matrix solvers with different preconditioners. For the NIM slab analysis most of these solvers encounter severe problems, especially when the NIM losses are small. For this reason, only direct matrix solvers could be used. Furthermore, FEMLAB allows one to select the finite element order. For NIM slabs, second or forth order is appropriate. The results shown are computed with second order elements.

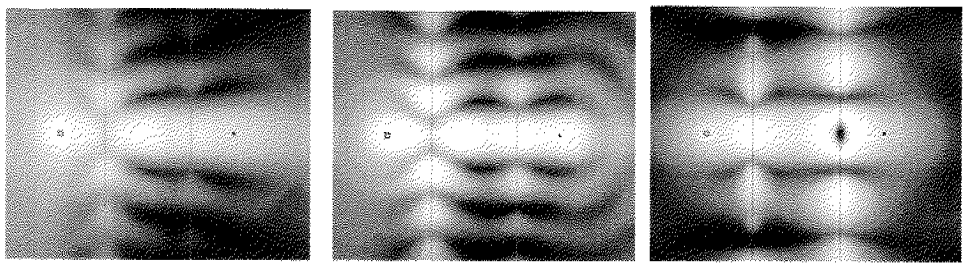

Fig.6.7 Mefisto3D simulation of an infinite NIM slab of width 1λ, illuminated by a point source S with electric field E perpendicular to the plane, time-averaged E field intensity at different times. Top: after 10 periods, center: after 25 periods, bottom: after 50 periods.

Figure 6.8 shows a reasonable convergence of the results when the automatic mesh refinement is used, but when the illumination of the focus line, i.e., the y-component of the time-averaged Poynting vector field along a line in x-direction through the focus point F is calculated (see Fig.6.9), one can see that substantial asymmetries are obtained although the geometry is symmetric, and that there are considerable differences between the three models. Furthermore, one can also see some noise in the solution obtained with the second model. This noise would cause failures when an automatic detection procedure for the maxima and minima would be applied. Since such an automatic detection is required for extensive studies of the resolution, such noise cannot be accepted. Figure 6.10 shows that the asymmetries and noise increase when the loss tangent is reduced. The FEM computation of nearly perfect NIMs with very low losses is therefore extremely time-consuming.

The mesh obtained in Fig.6.8 is obviously not well adapted to the specific features of the NIM slab which exhibits strong fields along the NIM boundary and near the focus points X and F. Of course, it would be possible to generate meshes that are more appropriate and lead to more accurate FEM results with smaller matrices, but this would require a substantially higher effort on the user side which is unacceptable for extensive studies.

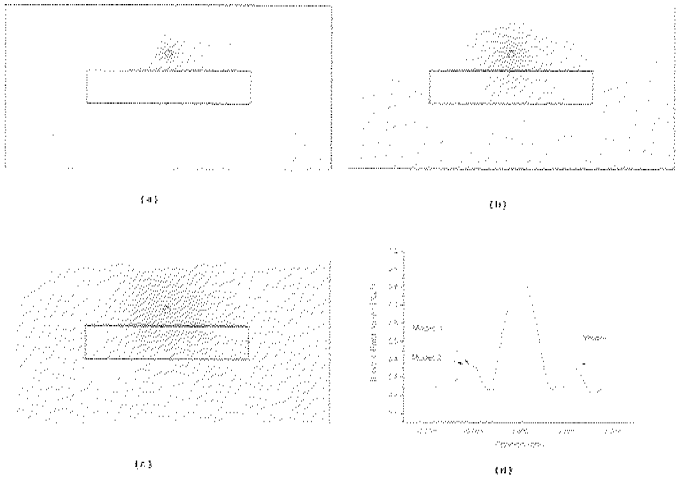

Fig.6.8 Three FEMLAB meshes for the simulation of a NIM slab of width 1λ, length of 5λ, illuminated by a small circular source S with electric field E perpendicular to the plane and norm of the electric field along the focus line (horizontal line through the focus point F). The loss tangent of the NIM is 0.01.

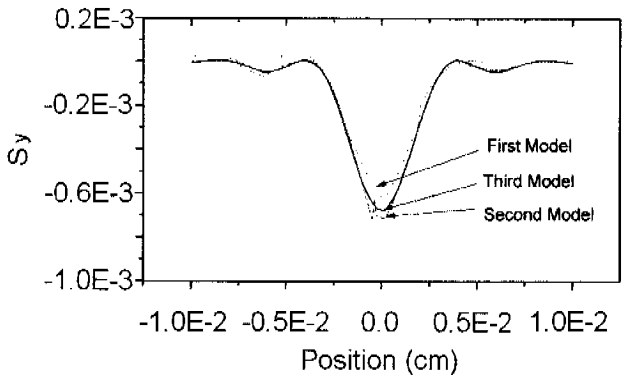

Fig.6.9 Same models as in Fig.6.8, y component of the time average of the Poynting vector field of the focus line.

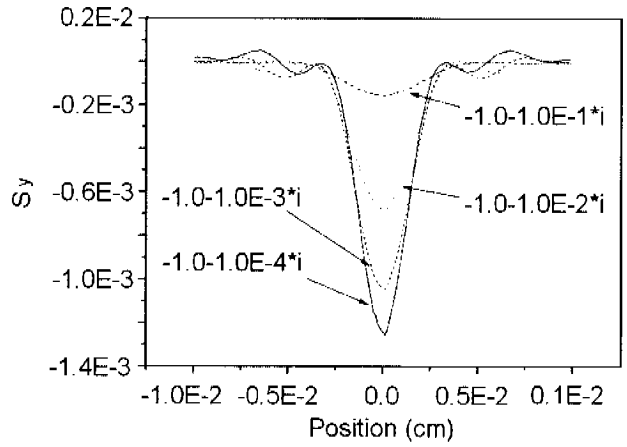

Fig.6.10 Model c of Fig.6.8, y component of the time average of the Poynting vector field along the focus line for different loss tangents of the relative permittivity and permeability of the NIM.

6.5 MMP analysis with a single source

For 2D frequency domain simulations, boundary methods that discretize only the 1D boundary of the NIM slab lead to much smaller matrices than FEM. Since one cannot take advantage of the sparsity of the FEM matrices by using iterative matrix solvers, boundary methods are superior to domain methods for this kind of applications. Furthermore, boundary methods need no truncation of the infinite space that is surrounding the NIM slab, i.e., no Absorbing Boundary Conditions (ABCs) that may affect the accuracy of the results.

MMP is based on the analytic Mie-Vekua theory [11] and provides exponential convergence for problems with boundaries that are infinitely many times differentiable. Therefore, results with extremely high accuracy of many digits may be obtained also for NIM slabs with very low losses. In the following, the latest MMP implementation of the MaX-1 [12] software package is used for exploring the optical properties and limitations of a NIM slab. This code also contains advanced features for the post-processing of the results, for the automatic detection of maxima and minima of a function, etc.

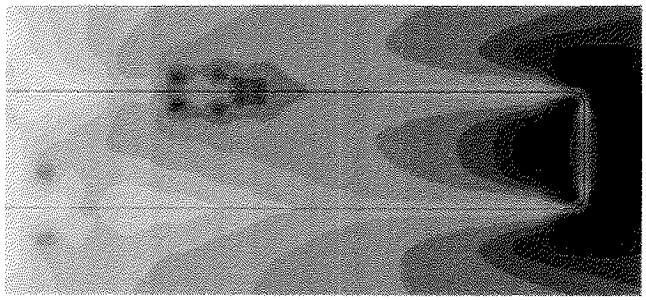

Fig.6.11 MMP simulation of a NIM slab of width 1λ, length of 10λ, illuminated by a small monopole source S with electric field E perpendicular to the plane. Intensity plot of the time-averaged Poynting vector field, logarithmic gray scale. The model is symmetric, only the right half is shown.

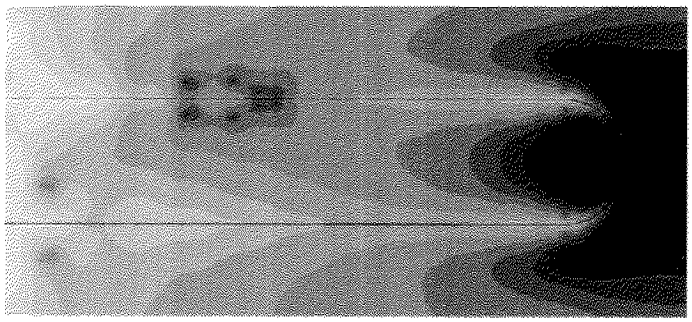

Fig.6.12 Same as in Fig.6.11 with circular endings of the slab.

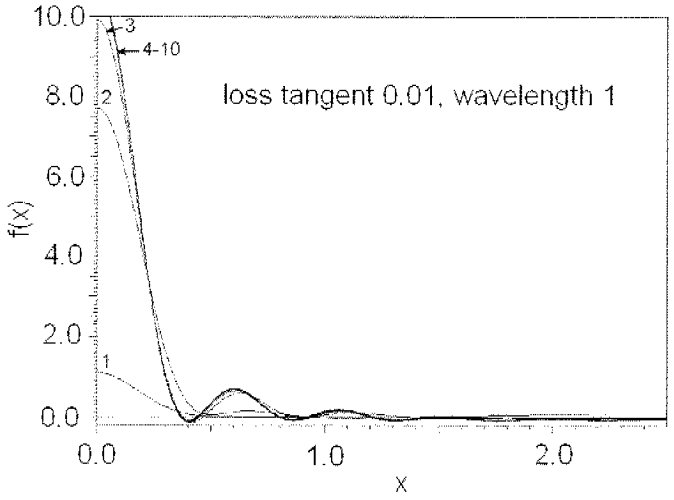

Fig.6.13 Illumination (negative y component of the time average of the Poynting vector field) of the focus line for a NIM slab with loss tangent 0.01 of width 1λ, length 1λ…10 λ.

First, a NIM slab illuminated by a single point source is considered. As seen from Fig.6.11, the field near the ending of the slab is rather high, even when the slab is so long that its endings are far away from the source. Therefore, one might assume that the shape of the endings and the length of the slab play important roles for its resolution. Figures 6.11 and 6.12 show the field of a NIM slab with rectangular and circular ending. Although the field near the ending is rather strong and depends much

on the shape of the ending, the field in the center area, where the source and focus points are located is almost not affected. Therefore the shape of the ending is negligible as long as the distance of the source point from the ending is big enough, i.e., in the same order as the width of the slab.

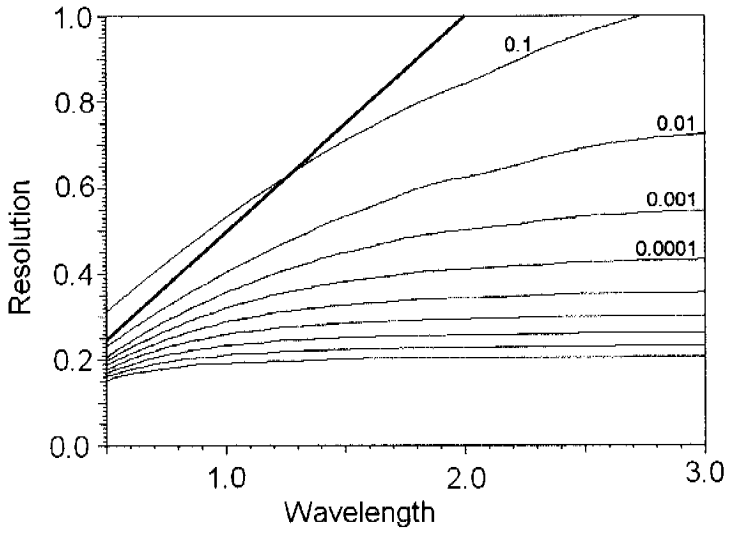

Fig.6.14 Resolution R_1' for a NIM slab of width 1λ and length 6λ with loss tangent varying from 0.1 to 10^{-9}. The thick line indicates the optical limit of resolution 0.5λ. Below this line, super-resolution in the sense of R_1' is obtained.

Figure 6.13 shows the illumination of the focus line for a NIM slab with moderate loss, width 1λ, and different lengths. From the locations of the first minima one obtains the resolution R_1'. As can be seen the resolution remains almost the same when the length of the slab is more than three times the width, whereas it becomes worse for shorter slabs.

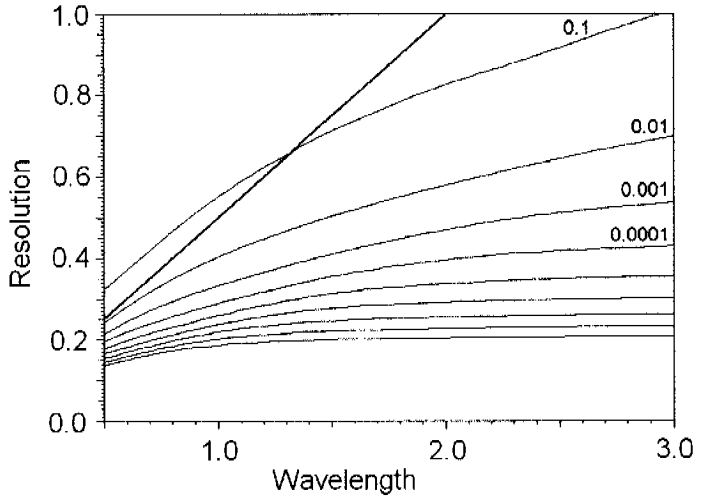

Fig.6.15 Same as in Fig.6.14 when a rectangular absorber is placed below the focus line. The size of the absorber is the same as the size of the NIM slab. Its relative permittivity and permeability are 2+2i and 1 respectively.

Since MaX-1 can automatically detect the locations of the first minima in Fig.6.13, it also can compute the resolution R_1'. Figure 6.14 shows R1' depending on the wavelength for different loss tangents of the NIM. The aspect ratio length/width is equal to 6. The wavelength is given in terms of slab width, i.e., the horizontal axis indicates wavelength/width.

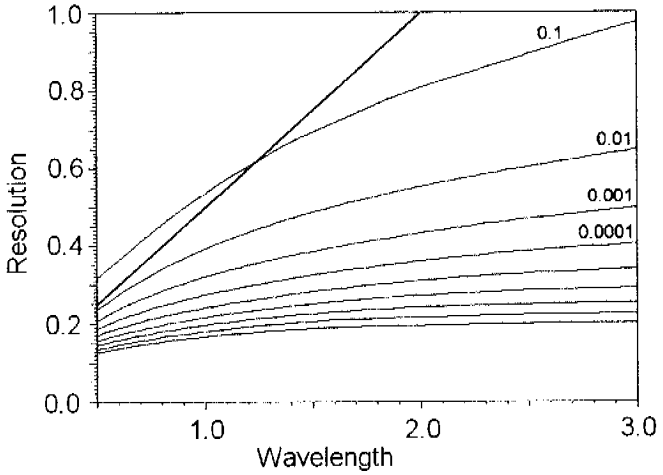

Fig.6.16 Same as in Fig.6.15 with an impedance matched absorber with both relative permittivity and relative permeability equal to 1+1i.

Fig.6.13 shows that the illumination near the first minimum is negative, i.e., the Poytning flux crosses the focus line from the wrong side because waves from the lateral sides of the slab turn back towards the slab in these areas. In practical experiments, an absorber (photoresist) is placed along the focus line and this absorber absorbs "lateral waves". Therefore, no negative illumination can be observed. For checking the influence of an absorber, a rectangular absorber can be placed directly below the focus line and the Poynting flux through its surface is computed again. Depending on the material properties of the absorber, the field is partially reflected and illuminates the NIM slab again. Fig.6.15 shows that an absorber with relative permittivity 2+2i and relative permeability 1 has no strong influence on R_1' although it suppresses the negative illumination and causes some reflections. In fact, the absorber even improves the resolution a little bit. A further improvement may be obtained when a hypothetical, impedance-matched absorber with relative permittivity 1+1i and relative permeability 1+1i is considered (see Fig.6.16). Incidentally, such an absorber might be obtained from an appropriate metamaterial design.

However, Figs. 6.14-6.16 indicate that a NIM slab exhibits super-resolution in the sense $R_1'<0.5\lambda$ when the loss of the NIM is small enough and when the width of the slab is not too big compared with the wavelength. The resolution of R_1' improves with smaller losses and smaller slab width.

6.6 MMP analysis with two sources

It was shown in the second section of this chapter that the super-resolution in the sense $R_1'<0.5\lambda$ does not guarantee super-resolution in the sense $R_2'<0.5\lambda$ or $R_2'<0.5\lambda$. To obtain more information on the optical properties of a NIM slab, we now consider a NIM slab illuminated by two symmetric point sources at $x = \pm x_{source}$. For a perfect lens with magnification 1 one would expect image points, i.e., locations with

maximum illumination in the focus plane at $x_{max}=x_{source}$ but - as for the conventional lens - a single peak is observed at x' = 0 when the distance d = $2x_{source}$ between the two sources is less than R_2. Thus, when the global maxima of the illumination are detected by an automatic routine, their location x_{max} remains at position 0 until the distance between the sources reaches R_2. For distances d>R_2, two symmetric maxima are detected at $\pm x_{max}$. For increasing x_{source}, the function x_{max} (x_{source}) oscillates around the diagonal $x_{max}=x_{source}$ as one can see from Fig.6.17 and Fig.6.18. The difference $x_{max}-x_{source}$ is an undesired imaging error. For large distances, this error disappears but in the regime of superresolution it is rather big. Obviously, R_2 considerably depends on the wavelength and on the NIM losses. For a reasonable loss tangent of 0.01 (Fig.6.18), and a short wavelength of 0.5 (times the slab width), R_2 is approximately 0.3 (the corresponding curve leaves the horizontal axis near x_{source} = 0.15 = $R_2/2$). Thus, the resolution R_2 is approximately 0.6λ which does not correspond to super-resolution. From Fig.6.14 it can be seen that R_1' is below 0.5λ for this case. However, when the wavelength is big enough, super-resolution is also obtained for R_2. For example, for wavelength 2.5 one has the minimum value of x_{source} near 0.6 and therefore R_2 near 1.2/2.5 slightly below 0.5λ. From Fig.6.17 one can see that R_2 is near 0.8/2.5, i.e. considerably below 0.5λ when the loss tangent of the NIM is reduced to 0.0001.

From the Fig.6.17(a) and Fig.6.18(a) one may also obtain the values $R_{2'}$, by searching the points where x_{max} (x_{source}) crosses the diagonal x_{max} = x_{source} for the first time. As one can see, these points are not much above the points where x_{max} (x_{source}) becomes >0. Therefore $R_{2'}$ is somewhat larger than R_2. The function $x_{max}(x_{source})$ is a smooth, monotonic function that starts at x_{max} = 0. Therefore, the resolution R_2' that is based on the shortest distance between the two maxima is always zero. Note that this is not the case for the classical lens (Fig.6.5), where one encounters either a single maximum at x' = 0 or two maxima at x'>0 with a local maximum at x' = 0 between the two global maxima that are relevant for R_2'. However, for the description of the NIM slab, R_2' is useless.

A perfect lens with magnification 1 should not only image a point source at x_{source} on a sharp peak of illumination at x_{max}, it should also provide proportionality between the amplitude of the source and of the image point. The Fig.6.17 and Fig.6.18 also show the scaled amplitudes of the maxima detected along the focus line as functions of the source locations. For a perfect lens, these curves should be equal to 1 for all locations of the sources. However, for small distances d, positive interference is observed and therefore the normalized amplitudes reach the value 4. For increasing distance d, the amplitudes decay and start oscillating around the line where the amplitude is 1. One can see very well that these oscillations remain rather strong with increasing x_{source}. Thus, for obtaining an image that accurately reproduces not only the location but also the intensity of the sources, the distance between the sources must be rather large. Note that this effect is not reduced when the loss tangent of the NIM slab is reduced. It seems that the NIM slab provides a mechanism that couples the sources over long distances.

From the curves shown in the Fig.6.17 and Fig.6.18 one can derive more sophisticated definitions of the resolution and additional characteristic values that describe the optical properties of the NIM slab, for example, the variation of the amplitudes of two symmetric sources for $x_{source}>R_2/2$. The computation of such characteristic values is very demanding for standard field solvers and requires advanced post-processing routines.

The consideration of a NIM slab with a symmetric pair of sources is a rather special case, but the more general case of two arbitrary sources can be decomposed in a symmetric and antisymmetric case – as long as the sources are sufficiently well centered. For the antisymmetric case one obtains the curves x_{max} (x_{source}) as for the symmetric case, but mirrored at the diagonal $x_{max}(x_{source})$. Because of destructive interference for short distances the amplitudes of the maxima are 0 for $x_{source} = 0$. With increasing x_{source} the amplitudes also oscillate around the line where the amplitude is 1, very much so as for the symmetric case.

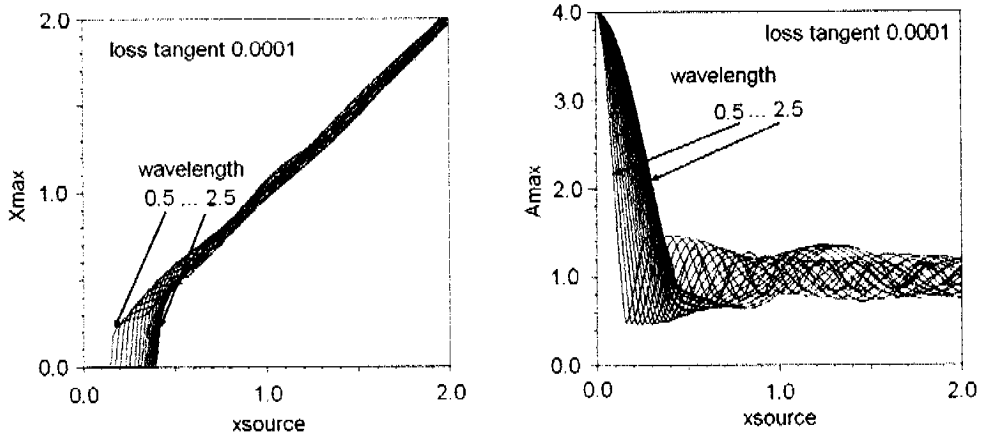

Fig.6.17 NIM slab with loss tangent 0.0001 of width 2 and length 20 (arbitrary units) illuminated by two symmetric monopole sources located at x = ± xsource (horizontal axis), at distance 1 from the slab, for different wavelengths, ranging from 0.5 to 2.5. Left hand side: Location xmax of the maxima detected along the focus line versus xsource. Right hand side: Amplitudes (arbitrary units) of the maxima detected along the focus line versus xsource.

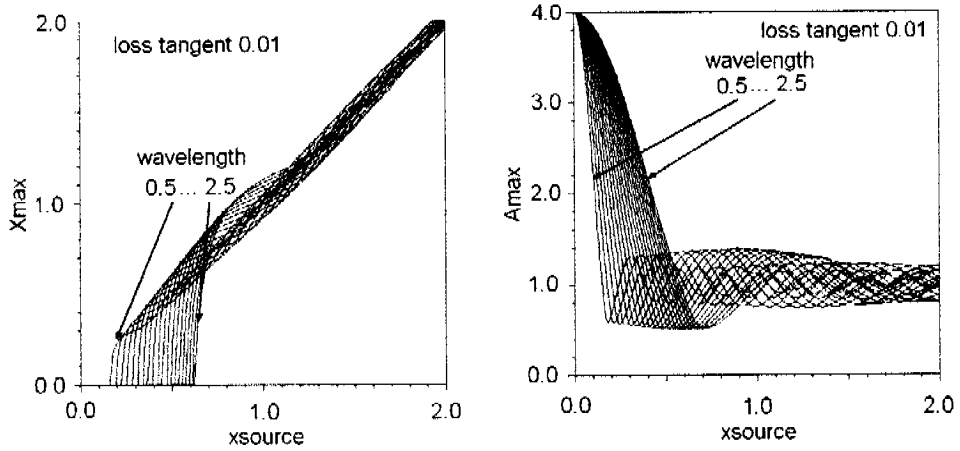

Fig.6.18 Same configuration as in Fig.6.17, for a more realistic loss tangent of 0.01.

In all simulations, the electric field was assumed to be perpendicular to the 2D plane. The alternative case with magnetic field perpendicular to the 2D plane may be simulated with all codes mentioned above. As long as all material properties have the same relative permittivity as the relative permeability, exactly the same results are obtained. The only exception is Fig.6.15, where the absorber has a relative permittivity different from the relative permeability.

The codes used in this chapter could also be used for studies with more than two sources: NIMs with a real part of the relative permittivity and permeability different from -1, or more general NIMs with more complicated geometry. The big number of model parameters of such general studies would go beyond the scope of this work.

6.7 Conclusions

Different definitions of the resolution of optical lenses and NIM slabs based on the locations of source and image points were introduced in addition to the well-known Rayleigh criterion for the optical resolutions. Some of these definitions are easier to compute and provide additional information. It has been demonstrated that whether super-resolution is obtained or not also depends very much on the definition of the resolution. Furthermore, super-resolution in the sense of resolution smaller than half of the wavelength may be also observed for classical dielectric lenses when the distances of source and image points from the surface of the lens are small enough. The near field effect of increasing resolution with decreasing distance of the source and image points from the surface of the lens is also typical for NIM slabs.

Different numerical Maxwell solvers were compared and applied to the NIM analysis. Finally, extensive and highly accurate studies of the resolution were carried out with the MaX-1 code. In addition to the influence of NIM loss and size, also the length of the slab and the shape of its endings are considered. Furthermore, it was demonstrated that an absorber near the focus plane has some influence on the resolution and that a higher resolution may be obtained with an appropriate absorber than without it.

Obtaining superresolution for a NIM slab with all kind of reasonable definitions of the resolution is only possible for sufficiently thins slabs with sufficiently low loss.

References

[1] V. G. Veselago, "The electrodynamics of substances with simultaneous negative values of ε and μ." *Sov. Phys. Usp.* **10**, 509-514 (1968).

[2] J.B. Pendry, "Negative refraction makes a perfect lens," *Phys. Rev. Lett.* **85**, 3966-3969 (2000).

[3] R.A. Shelby, D.R. Smith, S. Schultz, "Experimental verification of a negative index of refraction," *Science* **292**, 77-79 (2001).

[4] M. Nieto-Vesperinas, "Problem of image super-resolution with a negative-refractive-index slab, *J. Opt. Soc. Am. A*, **21**, 491-498 (2004).

[5] D.O.S. Melville, R.J. Blaikie, "Near-field optical lithography using a planar silver lens," *J. Vac. Sci. Technol. B* **22**, 3470-3474 (2004).

[6] N. Fang, H. Lee, C. Sun, X. Zhang, *Science* **308**, 534 (2005).

[7] N.-C. Panoiu, R.M. Osgood Jr., "Influence of the dispersive properties of metals on the transmission characteristics of left-handed materials," *Phys. Rev. E* **68**, 016611 (2003).

[8] A. Grbic, G.V. Eleftheriades, "Overcoming the diffraction limit with a planar left-handed transmission-line lens, *Phys. Rev. Lett.* **92**, 117403 (2004).

[9] P.M. So, H. Du, W.J.R. Hoefer, "Modeling of metamaterials with negative refractive index using 2-D shunt and 3-D SCN TLM networks," *IEEE Trans. MTT*, **53**, 1496-1505 (2005).

[10] P.F. Loschialpo, D.W. Forester, D.L. Smith, F.J. Rachford, "Optical properties of an ideal homogeneous causal left-handed material slab," *Phys. Rev. E* **70**, 036605 (2004).

[11] Ch. Hafner, Post-modern Electromagnetics: Using intelligent Maxwell Solvers, John Wiley & Sons, Chichester (1999).

[12] Ch. Hafner, *MaX-1, a visual electromagnetics platform for PCs*, John Wiley & Sons, Chichester (1999).

[13] J.-S. Lih, Y.-S. Wang, M.-C. Lu, Y.-C. Huang, K.-H. Chen, J.-L. Chern, L.-E. Li, "Experimental realization of breaking diffraction limit by planar negative-index metematerials in free space," *Europhysics Lett.* **69**, No.4, pp. 544-548, Feb. (2005).

[14] Z. Lu, S. Shi, C. A. Schuetz, J. A. Murakowski, D. W. Prather, "Three-dimensional photonic crystal flat lens by full 3D negative refraction," *Opt. Express* **13**, No. 15, pp. 5592-5599, July (2005).

[15] J. L. Garcia-Pomar, M Nieto-Vesperinas, "Imaging of extended objects by a negative refractive index slab," *New Journal of Physics* **7**, No. 160 (2005). (http://www.njp.org).

[16] http://www.remcom.com/xfdtd6/index.html.

[17] http://www.optiwave.com/2005/products/optifdtd/index.html.

[18] http://www.empire.dc

[19] http://www.cst.de/Content/Products/MWS/Overview.aspx

[20] http://www.ansoft.com/products/hf/hfss/

[21] http://www.comsol.com/products/

[22] http://www.mathworks.com

[23] Viktor A. Podolskiy, Evgenii E. Narimanov, " Near-sighted superlens", *Opt. Lett.* **30**, No. 1, January (2005).

[24] Akhlesh Lakhtakia, "On perfect lenses and Nihility", *Int. J. Infra. and Mill. waves* **23**, No. 3, March (2002).

[25] N. Garcia, M. Nieto-Vesperinas, "Is there an experimental verification of a negative index of refraction yet? ", *Opt. Lett.* **27**, No. 11, June (2002).

[26] Sebastien Guenneau, Boris Gralak, J. B. Pendry, " Perfect corner reflector, " *Opt. lett.* **30**, No. 10, May (2005).

[27] D. R. Smith, D. Schurig, J. B. Pendry, "Negative refraction of modulated electromagnetic waves, " *App. Phy. Lett.* **81**, No. 15 (2002).

[28] K. J. Webb, M. Yang, D. W. Ward, K. A. Nelson, "Metrics for negative-refractive-index materials, ", *Phy. Rev. E* **70**, 035602 (2004).

[29] J. L. Garcia-Pomar, M. Nieto-Vesperinas, "Transmission study of prisms and slabs of lossy negative index media," *Opt. express* **12**, No. 10, 17 May (2004).

7 Summary, conclusions and outlook

In this chapter, the main results obtained in this dissertation are outlined, conclusions are drawn, and the future work is sketched.

7.1 Metallic photonic crystals at RF and OF

In chapter 2, metallic photonic crystals at radio and optical frequencies are studied. At RF, metals are more reflective and less lossy than at OF and can be regarded as perfect electric conductors due to their high conductivity, which drastically simplifies the models and numerical computations when metallic photonic crystals are analyzed at RF and even in the far infrared region. At OF, metals lose their conductivity due to the mass of electrons, and the absorption of metal can not be ignored any more. This increases difficulties for the simulation, namely when one attempts to take loss into account. Therefore, the analysis of metallic photonic crystals at OF is much more demanding than the analysis of metallic photonic crystals at RF. Additional problems are the strong frequency dependence of the material properties and the material losses that are too high for simplified, loss-free computations with real-valued eigenvalues, i.e., resonance frequencies.

The band diagrams of two-dimensional metallic photonic crystals with Ez and Hz polarization are calculated respectively by using the well-developed MaX-1 platform with its MMP solvers. In Ez polarization, metallic photonic crystals have a fundamental band gap with frequency range from zero to cutoff frequency of the first mode. This is very interesting for engineering. It means that there is no low-frequency limit for metallic photonic crystals which opens a door for applications at long wavelengths including negative index metamaterials; In Hz polarization, flat-bands appear in the dispersion curve which are caused by surface plasmon effects and can result in very low group velocity and thus can be used for threshold-less laser sources and as sources for the excitation of surface plasmons. Unfortunately, as demonstrated in this thesis, the modes in the flat pass band are very sensitive regarding material loss. This spoils the attractive properties of the flat pass band.

Currently, most of the work published on metallic photonic crystals relies on loss-free calculation that completely ignores absorption and therefore may be misleading. In addition to the study of the influence of losses, the impact of other parameters, namely, the properties of the dielectric background material was analyzed in chapter 2.

7.2 Compact metallo-dielectric photonic crystal filter design

Filters are widely used in different areas. As shown in chapter 1, metallic photonic crystals may have smaller sizes than their dielectric counterparts. This makes them attractive for ultra-compact structures, including filters. From chapter 2, one can see that RF models are much closer to realistic metallic photonic crystals as long as the frequency is not very high and the material loss is acceptable. To verify the conclusions drawn from chapter 2, ultra-compact metallo-dielectric photonic crystal filters are designed and simulated including material loss and dispersion. To shorten the computation time, a speed-up technology, model-based parameter estimation is used. Combing with highly accurate field solvers, reliable results are obtained in very short computation time. The analyzed filters consist of only five silver wires

embedded in a waveguide structure. The total length of these filters is as short as 4100 nm. However, to design higher quality factor filters, more layers and additional optimization variables are needed. However, the methods and routines shown in chapter 3 are still valid and efficient for bigger filter structures.

Although the numerical problems caused by material loss are solved, the realization of such structures is still a problem because of the large extent required to establish photonic crystal properties. In Chapter 4, this problem is solved and ultra-compact photonic crystal filters are proposed and optimized with more efficient optimization procedures.

7.3 Design of filters based on photonic crystal slabs

An important aspect of the simulation work is that the theoretical design should finally provide useful information for engineering. To realize the structures shown in chapter 3 in practice, i.e., in integrated optical circuits of small size, two methods are presented in chapter 4: a) using conducting walls that replace the periodic boundary conditions of the PhC slab and b) embedding a PhC filter in a conventional waveguide structure.

In chapter 3, silver photonic crystal filters with different background materials were designed. Although silver is less absorptive than other well-known noble metals, it is still so absorptive at OF that silver parts within filter structures may cause high loss and drastically reduce the filter quality. In order to minimize these undesired effects, in chapter 4 only short periodic dielectric structures are considered with short metallic coatings. The principles and optimization procedures are not affected by this. When silver coatings are added near the PhC structure, the filter response is completely destroyed, while for idealized PEC coatings, less influence on the filter characteristics is observed. An attempt to reestablish the desired filter response by a new optimization that takes the silver coatings into account is successful. This demonstrates that it is possible to design ultra-compact filters embedded in dielectric waveguides with short coatings.

Concerning the fabrication issues, currently it is possible to realize such filter structures in a laboratory. But as material loss causes low quality filter response, the application of such passive filter structures at OF still has a long way to go, i.e., unless metals with low loss and high reflectivity at OF have been found. On the other hand, this is also a challenge for numerical methods that need to take material loss into account.

7.4 Minimization of radiation near a sharp waveguide bend

Waveguides bends are of major importance for the integration density. Conventional waveguides exhibit unacceptable radiation loss except for large bend radii that cause low integration density. In chapter 5, a new design method with efficient optimization procedures is presented to show that without increasing the bend radius and without using complex design rules, sharp bends with high transmission are possible. Three types of bend structures are analyzed and compared: mirror-based, resonator-based and mirror-based with photonic crystals in the bend area. The promising features of the third are that the photonic crystals not only suppresses radiation but also provide solutions with fewer fabrication tolerance problems.

In chapter 5, all structures are designed for Ez polarization. For Hz polarization, the design rules remain the same. But it should be pointed out that there are some limitations when one selects 'rods in air (dielectric columns)' photonic crystal

structures for Hz polarization. The main reason is because of small band gaps of such structures. This also holds for other lattices without metallic inclusions. For Hz polarization, the 'rods in air' structure in a squre lattice has no reasonable band gap. Therefore, a triangle lattice is employed in this case as shown in Fig.7.1.

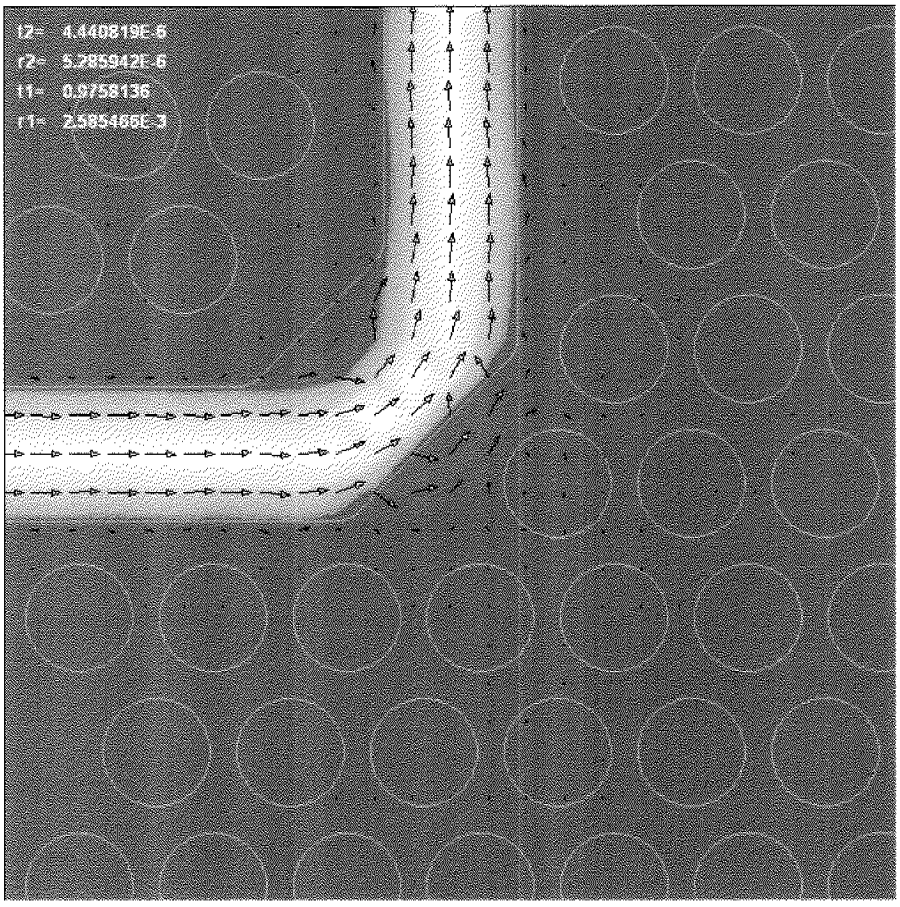

Fig.7.1 Mirror-type bend structure with photonic crystal for Hz polarization. Photonic crystals are arranged on a triangular lattice.

Metals at optical frequencies exhibit high reflectivity although absorption can not be avoided. As the results in chapter 4 show, they act as mirrors even though they are not perfect at all. Silver was added to the bend part of the waveguide and then the transmission coefficient of the first mode was evaluated. When the results with and without metal coatings are compared, one can see that there is no big difference in the transmission provided that the bend part is well-designed. Because of mode mismatching at the transitions from the uncoated to the coated waveguide sections, also high order modes may be excited. In fact, mode conversion is observed as shown in Fig.7.2. However, when the coatings are well designed and optimized, high transmission is still possible as shown in Fig.7.2b. This means the absorption caused by metal loss may be small enough.

The theoretical studies give us many surprises but unfortunately, the fabrication and measurement results are beyond what we expected. In this chapter, the author also analyzed the possible reasons of inaccuracies caused by fabrication and measurements. Highly accurate fabrication operation and measurement methods are needed in future

research, as well as a more efficient effective index approximation method for simulation.

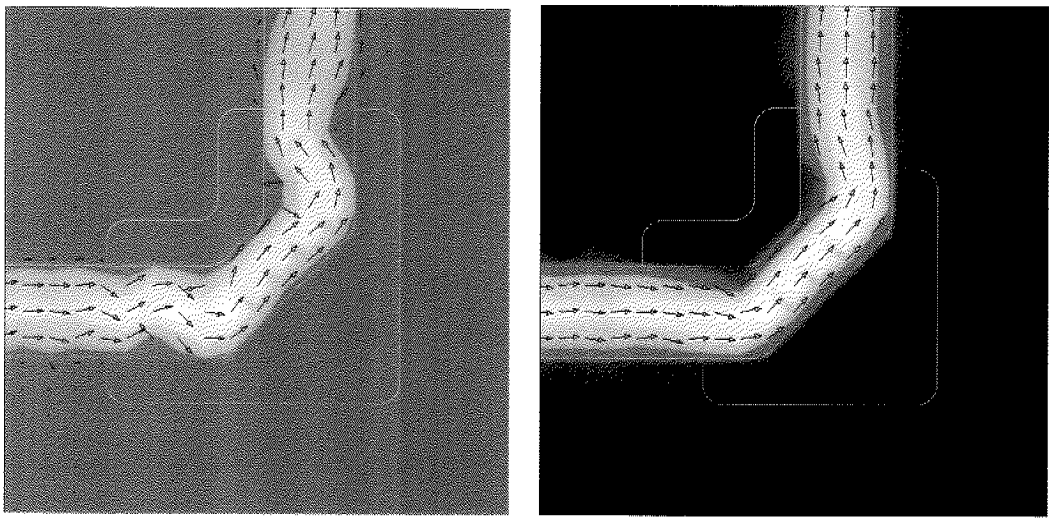

(a) (b)

Fig.7.2 Bend structure with metallic coatings, the pure bend structure shown in Fig.4(b) in chapter 4 was used. (a) $T_1 = 0.7248$; (b) $T_1 = 0.9565$.

7.5 Resolutions of negative index slabs

Negative index materials (NIMs) attract much attention because of their unusual physical phenomena, i.e., inverse Doppler effect, inverse Cerenkov radiation, reversal of Snell's law etc. One of the important applications of NIMs is the so-called 'perfect lens' that firstly was proposed by Pendry. A planar 'perfect lens' made by NIMs with refractive index -1 could amplify the evanescent waves thus the degradation of the image caused by an imaging system can be recovered without any other help. In chapter 6, this issue was considered in more detail and it was demonstrated that superresolution only is obtained for thin NIM slabs, i.e., superresolution remains a near field effect.

Many research groups announced that they already fabricated a 'super-lens' and observed super-resolutions. All these results show that the resolutions are 0.44λ just a little bit below the diffraction limit 0.5λ. This is of questionable value if one thinks about numerical, fabrication, and experimental errors. Furthermore, the resolution definition used by these researchers is not the same as the Rayleigh definition for classical optical lenses which is a source of confusion. To clarify these problems, different definitions of the resolution of negative index material slabs are given and discussed in chapter 6. It is found that super resolution depends very much on the definition of the resolution and that it may be obtained not only for NIM slabs but also for highly refracting classical lenses when the distances of the image and source points from the surface of the lens or slab are shorter than the wavelength.

The efforts of searching low loss NIMs are still ongoing. It is worth noting that photonic crystals with appropriate arrangements have 'refractive-like' behavior. Usually photonic crystals and negative index metamaterials are considered to have essential difference: photonic crystal structures are operated at the frequencies where the lattice constant is comparable with the guided wavelength, while the lattice

constant of NIM cells is much shorter than the wavelength. As a consequence, the role of the lattice in photonic crystals is crucial for the properties of photonic crystal structures, i.e., they are operated in the Bragg regime and the structure is inhomogeneous. NIMs are operated in the long wavelength regime where the properties are determined by the nature of the unit cell, thus the lattice is not necessary to be periodic and the structure is homogenous. However, it should be pointed out that metallic photonic crystals (see chapter 2) operating in the fundamental band gap considerably below the upper frequency limit also have a lattice constant much shorter than a wavelength. In this sense, NIMs may also be considered as metallic photonic crystals.

The research of NIMs is just beginning. As NIMs are extraordinary artificial materials, people start thinking about many interesting applications they never considered before. More and more new functional metamaterials effects are expected to be exploited in the future!

List of publications during PhD study

Peer-reviewed journal papers

[1] Cui Xudong, Christian Hafner, Ruediger Vahldieck, Franck Robin, "Sharp trench waveguide bend in dual mode operation with small photonic crystal for suppressing radiation," *Opt. Express* **14**, No. 10, pp. 4351-4356, May (2006).

[2] Cui Xudong, Christian Hafner and Ruediger Vahldieck, "Design of ultra-compact metallo-dielectric photonic crystal filters," *Opt. Express* **13**, No. 16, pp. 6175 - 6180, August (2005).

[3] Cui Xudong, Christian Hafner, Ruediger Vahldieck, "Dielectric and Metallic photonic crystal filters design with the Multiple Multipole Program," *J. Opt. Soc. Am. A*, 2007, accepted.

[4] Cui Xudong, Christian Hafner, Jasmin Smajic, Ruediger Vahldieck, "Efficient procedures for the optimization of defects in photonic crystal structures," *J. Opt. Soc. Am. A*, accepted.

[5] Ch. Hafner, Cui Xudong, and R. Vahldieck, "Metallic photonic crystals at optical frequencies," *Journal of Computational and Theoretical Nanoscience*, 2(2):240-250, June 2005.

[6] Christian Hafner, Cui Xudong, Ruediger Vahldieck, "Resoultions of Negative-Index Slabs," *J. Opt. Soc. Am. A* **23**, no. 7, July 2006.

[7] Christian Hafner, Cui Xudong, Ruediger Vahldieck, "Stochastic parameter optimizers for optical nanostructures," *International Journal of Microwave and Optical Technology*, vol. 1, 2006.

[8] F. Robin, D. Erni, S. Costea, P. Cristea, X. Cui, Y. Fedoryshyn, E. Gini, C. Hafner, R. Harbers, J. Holzman, H.-J. Lohe, P. Ma, K. Rauscher, R. Scollo, G. Stark, P. Strasser, W. Vogt, R. Wüest, and H. Jäckel. Photonic integration for high density and multi-functionality in the InP-material system. *Proc. SPIE*, 6124:612415-1-15, March 2006. Invited Paper.

[9] Kakhaber Tavazrashivli, Christian Hafner, Cui Xudong, Ruediger Vahldieck, "Model based parameter estimation for metallic photonic crystal filters design," *ACES Journal*, 2007.

[10] Roman Kappler, Daniel Erni, Cui Xudong, N.Lovtny, "Field computation of optical antenna, " J. Comput. Theor. Nanosci., Accepted, October 2006.

[11] Jasmin Smajic, Christian Hafner, Cui Xudong, Ruediger Vahldieck, "Numerical optimization of photonic crystal structures, " J. Comput. Theor. Nanosci., Accepted, October 2006.

[12] Kakhaber Tavazrashivli, Christian Hafner, Cui Xudong, Ruediger, Vahldieck, D. Kakulia, G. Ghvedashvili, D. Karkashadze, "Method of Auxiliary Sources and Model-Based Parameter Estimation for the Computation of Periodic Structures," J. Comput. Theor. Nanosci., Accepted, October 2006.

International conference papers with referees

[1] Cui Xudong, Christian Hafner, Nicolas Guerin, Ruediger Vahldieck, "Metallicphotonic crystal at optical frequencies," *In IEEE AP-S, Washington*, 2005.

[2] Cui xudong, Christian Hafner, Kakhaber Tavazrashivli, Ruediger Vahldieck, "Metallic photonic crystal filter design using MMP method," *In IEEE APMC 2005.*

[3] Cui xudong, Christian Hafner, K.Tavazrashivli, Ruediger Vahldieck, "Surface Impedance Boundary conditions to metallic photonic crystal," *In IEEE APMC* 2005.

[4] Cui xudong, Christian Hafner, K. Tavazrashivli, R.Vahldieck, "Design of filters based on photonic crystal slabs," *International Conference on Mathematical Methods in Electromagnetic Theory (MMET'06)* June 26 - 29, 2006, IEEE, Kharkov, Ukraine.

[5] Cui xudong, Christian Hafner, K. Tavazrashivli, R.Vahldieck, "Parameters extraction from inhomogeneous metamaterials with model based parameter estimation," *International Conference on Mathematical Methods in Electromagnetic Theory (MMET'06)* June 26 - 29, 2006, IEEE, Kharkov, Ukraine.

[6] K. Tavazrashivli, Christian Hafner, Cui xudong, R.Vahldieck, "Model based parameter estimation (MBPE) for solving non-linear eigenvalue problems," *International Conference on Mathematical Methods in Electromagnetic Theory (MMET'06)* June 26 - 29, 2006, IEEE, Kharkov, Ukraine.

[7] K. Tavzarashvili, D. Karkashadze, Ch. Hafner, and Cui Xudong. Efficient field solvers for the analysis of photonic crystal filter. In N.N. Voitovich, editor, *Direct and Inverse Problems of Electromagnetic and Acoustic Wave Theory, 2005. DIPED 2005.*, pages 164-167, NASU, 3b Naukova St., Lviv, 79601, Ukraine, September 2005. *IEEE MTT/ED/AP/CPMT/SSC West Ukraine Chapter and MTT/ED Republic of Georgia Chapter.*

[8] K. Tavzarashvili, Ch. Hafner, C. Xudong, and R. Vahldieck. Model-based parameter estimation (mbpe) for metallic photonic crystal filters. In *Asia Pacific Microwave Conference, 2005. APMC 2005*, December 2005.

[9] N. Guerin, C. Hafner, X.Cui and R. Vahldieck. Compact directive antennas using frequency-selective surfaces (fss). In *Asia Pacific Microwave Conference*, Suzhou, China, December 2005. IEEE.

[10] Christian Hafner, Cui Xudong, Andre Bertolace, Ruediger Vahldieck, "On the design of optical antenna, " In the 23rd International Review of Progress in Applied Computational Electromagnetics (ACES 2007), March 19-23, 2007, Verona, Italy, invited paper.

[11] Christian Hafner, Jasmin Smajic, Cui Xudong, Ruediger Vahldieck, "Simulation and optimization of photonic crystal structures, " In the 23rd International Review of Progress in Applied Computational Electromagnetics (ACES 2007), March 19-23, 2007, Verona, Italy, invited paper.

[12] Franck Robin, Ping Ma, Patric Strasser, Robert Wuest, Heinz Jaeckel, Cui Xudong, Christian Hafner, "Fabrication and characterization of compact photonic wire 90 degree bends in InP, " In the 1st European Topical Meeting on

Nanophotonics and Metamaterials, 8-11 January, 2007, Seefeld ski resort, Tirol, Austria.

[13] Kakhaber Tavaznashivli, Christian Hafner, Cui Xudong, Ruediger Vahldieck, "Band structure calculation by using the model based parameter estimation technique, " In the 1st European Topical Meeting on Nanophotonics and Metamaterials, 8-11 January, 2007, Seefeld ski resort, Tirol, Austria.

Invited talk in workshop

[1]Cui Xudong, Christian Hafner, Ruediger Vahldieck, "Photonic crystals with metallic inclusions," *In Micro and Nano Science Platform, Industry Day,* Zurich, Switzerland, 4th, September, 2006 .

[2]Jasmin Smajic, Cui Xudong, Christian Hafner, Rüdiger Vahldieck, "Numerical optimization of photonic crystal structures ", In *Workshop on Numerical Methods for Optical Nano Structures*, July 10, Zurich, Switzerland, 2006.

[3] Cui Xudong, Christian Hafner, Ruediger Vahldieck, "Photonic crystals at Optical Frequencies," In *First Material Research Center Graduate Symposium*, June 29, Zurich, Switzerland, 2006.

[4] Cui Xudong, Christian Hafner, Ruediger Vahldieck, "Photonic crystal bend: design with conventional waveguide, " In Joint meeting of optETH and the Optics Division of the Swiss Society of Optics and Microscopy (SSOM) ,Zurich, Switzerland, September, 2006.

[5] Cui Xudong, Christian Hafner, Ruediger Vahldieck, "High index of refraction metamaterial with metallic photonic crystals, " In *Sino-Swiss Science and Technology Workshop 2006- Material Science*, Oct. 30-31, 2006, ETH Zurich, Switzerland.

Acknowledgements

First, many thanks are given to my supervisors: Prof. Ruediger Vahldieck, Chair and Head of Department D-ITET, Head of Laboratory for Electromagnetic Fields and Microwave Electronics (IFH), let me stay in the institute and pursue the work; and Prof. Christian Hafner, Head of Computational Optics Group (COG) at the IFH, who offered me the opportunity to work with him and guided me without any keeping of his knowledge. It was them who show me the way to unveil the mysterious world of electromagnetic fields. Special thanks are given to Prof. Hans-Peter Herzig, Head of Applied Optics Lab (AOL), Institute of Microtechnology (IMT), University of Neuchâtel, for his reviewing of my thesis as coexaminer.
Furthermore, I would like to thank Dr.Daniel Erni, Dr.Jasmin Smajic, Dr.Kakhaber Tavzarashvili, Dr.Nicolas Guerin for their help, Krish, George, Johannes for their accompanies during my PhD study.
Finally, I want to thank my family for their support during my studies, especially my wife, for her encouragement all the time.

Zurich, May 2006 Cui Xudong

Resume

I was Born on 6th March 1973 in Yunnan, a mysterious and beautiful place located at southwest of China. After I got my bachelor degree in Beijing Institute of Technology, I found a job in the Institute of Fluid Physics, worked with image processing. Several years later, I got my master degree and became an assistant professor there. Another few years' stay in Singapore, I came to ETH and continue my study in the Laboratory for Electromagnetic Fields and Microwave Electronics, the time already passed thirty years since I was born!